UNIVERSITY OF SALERNO
DEPARTMENT OF CHEMISTRY AND BIOLOGY "A. ZAMBELLI"

and

UNIVERSITY OF BASILICATA
DEPARTMENT OF SCIENCE

Ph.D. in Chemistry
Cycle XXX
CHIM/02 – Physical Chemistry

Thesis on

THIN COATINGS OF BIOMATERIALS FOR HARD TISSUE APPLICATIONS

TUTOR:
Prof. Angela De Bonis

CO-TUTOR:
Prof. Roberto Teghil

Ph.D. Student:
Mariangela Curcio
Matr. 8800100008

EXTERNAL TUTOR:
Dr Julietta V. Rau

COORDINATOR:
Prof. Gaetano Guerra

Academic Year 2016/2017

Acknowledgements

Foremost, I would like to express my very great appreciation to Prof. Angela De Bonis, my research tutor, for her patient guidance, enthusiastic encouragement and constructive suggestions.

My grateful thanks are also extended to Prof. Roberto Teghil, my co-tutor, for the precious scientific support, and Julietta V. Rau, my external tutor, for the collaboration and for always having her door open to any discussion and help.

I owe sincere and earnest thankfulness to Prof. Dr.-Ing. habil. Aldo R. Boccaccini, who welcomed me for six months in the Institute of Biomaterials at the University of Erlangen-Nuremberg. I am grateful to all the people who helped me in that period, in particular Dr.-Ing. Rainer Detsch, Alina Grünewald and Laura Ramos Rivera.

I would like to offer my special thanks to all the institutions with which a work in collaboration has been conducted.

In particular, I would like to thank the members of the ISM-CNR (Tor Vergata), especially Dr. Marco Fosca and Valerio Graziani, the ISM-CNR (Montelibretti), specifically Dr, Adriana De Stefanis, who synthesized some of the employed materials, and Dr. Sara Lureti for the magnetic measurements, and the ISM-CNR (UOS Tito Scalo), especially Dr. Antonio Santagata for the scientific support and the possibility to use the fs pulsed Ti-sapphire laser. I am also thankful to the members of the IFT-CNR of Rome, for the biological tests, and the researchers of University Politehnica of Bucharest for the experiment with Mg-Ca substrates.

My special thanks are extended to all the technicians who helped me during this period: Agostino Galasso, Sandro Laurita, Antonio Romano, Neluta Ibris; I am particularly grateful for their precious assistance and their willingness to give me their time.

I thank my labmates for the stimulating discussions and for making life fun while working: Maria, Jessica, Antonella, Serena, Antonio, Nicola, Arcangelo and all the other students, I will miss the time spent together.

I want to thank my parents for the patience, my brother Ivano and my sister Gaia for their support and encouragement throughout my study. I wish to thanks all the "old" and new friends who trust me. All of them helped me to do not forget to enjoy the many other beautiful things life has to offer.

Finally I want definitely thank my fiancé Gabriele for making everything possible, you only can know how important your presence is for me.

Contents

List of figures

List of tables

Introduction

With the increasing of life expectancy, thus the aging of the population, the interest has been turned to a whole healthy life. At the biological level, the ageing is in fact associated with an accumulation of damage to cells that, over time, causes the weakening of the immune system and the self-repair and the increasing of the chance of developing various diseases [1]. As regards the problems connected to hard tissue, both bone and dental diseases make difficult, if not impossible, the normal life of old people. Fractures, as consequence of bone disease, and tooth loss, dental caries, periodontitis can compromise older people's quality of life [2].

Extraordinary progress has been made in hard tissue health in the last decades [3]. Continuous advances in term of materials and technologies are being made.

The goal of the present study is the production of new-generation coatings suitable for hard tissue implants, intended to decrease the healing time, limit infections and rejections and improve patients' life quality.

Materials designed for implant coatings are mainly bioactive ceramics. Belonging to this class of biomaterials, hydroxyapatite (HAp), bioglass (BG) and glass-ceramic (BGC) are indicated for application in hard tissue replacement and regeneration in form of filler, scaffold, implant or prosthesis coatings. However the use of each one has strengths and weaknesses; therefore the attention has been focused on their peculiarity in the coating of metallic materials, suitable for hard tissue replacement. In particular, in order to overcome their drawback and enhance their strengths, possible solutions, like the adding of helpful component in the basic material or the choice of composites, have been investigated.

In this thesis the experimental evidences of the ability of pulsed laser deposition (PLD) to make films of all these classes of bioactive ceramics will be demonstrated. In addition, the efficiency to produce composite polymer/bioceramic coating of another deposition technique, i.e. the electrophoretic deposition (EPD), will be provided.

Almost all the experiments have been carried out with non-conventional materials:

- Hydroxyapatite has been deposited together with iron oxide nanoparticles (IONPs), with the aim to impart magnetic properties to the deposited composite films.

- A Cu containing bioglass, obtained with the adding of a certain amount of copper oxide in the 45S5 composition, has been deposited by PLD and EPD. Electrophoretic deposition has been used to obtain composite polymer/BG film. In fact, conventional PLD is not indicated for organic component, since their interaction with the laser beam causes the degradation of the molecules, on the contrary EPD is a really promising technique for the co-deposition of polymers and bioactive glasses.

- RKKP has been the bioactive glass ceramic deposited with PLD on Ti and Mg-Ca substrate. It has been also co-deposited with carbon-based material, in order to improve the mechanical properties of the coating. Furthermore another element, manganese, with proved influence on bone formation has been added in the glass-ceramic composition.

The thesis is organised in six chapters followed by general conclusions. In Chapter 1, the history and evolution of biomaterials are briefly illustrated. Afterwards, biomaterials for hard tissue applications are individually described in detail. In Chapter 2, the available techniques for coatings deposition are reported, whereas an accurate description of the employed techniques, i.e. pulsed laser deposition and electrophoretic deposition, is provided. The materials and methods of all the works are reported in Chapter 3. This chapter is followed by three different chapters in which the experiments conducted on the three class of bioceramics, reported above, are presented separately. In particular, in Chapter 4 hydroxyapatite-based films, in Chapter 5 bioglasses deposited by the means of PLD and EPD and in Chapter 6 films of the glass-ceramic named RKKP are described.

This thesis results from a collaboration between the Laser laboratory, Department of Science, University of Basilicata, and ISM-CNR, Tor Vergata, Rome.

CHAPTER 1

Biomaterials

One of the early definition of biomaterials was given in 1983 during the Consensus Development Conference on "Clinical Applications of Biomaterials". A biomaterial was defined as *"any substance (other than a drug) or combination of substances, synthetic or natural in origin, which can be used for any period of time, as a whole or as a part of a system which treats, augments, or replaces any tissue, organ, or function of the body"* [4]. This definition was not clear enough: it was not possible to distinguish between traditional materials, also used in the medical field, and materials interacting with a living organism. This inaccuracy was overcome with the definition agreed during the 1st Biomaterials Consensus Conference (1986, Chester, UK) [5], when biomaterial was defined as *"A nonviable material used in a medical device, intended to interact with biological systems"*.

Finally, a more complete definition was agreed in the 2nd Biomaterials Consensus Conference (1992, Chester, UK) [6]: *"A material intended to interface with biological systems to evaluate, treat, augment, or replace any tissue, organ, or function of the body, in order to maintain or improve the quality of life of the individual"*.

The first characteristic of a biomaterial is the biocompatibility, i.e. the ability to induce an appropriate response within the human body after implantation.

Biomaterials may be metals, ceramics, polymers and composites and, according to their composition, they exhibit peculiar properties. In the last 50 years an accurate selection of materials, for recovering and replacing of physiologic disabilities with innovative device, have significantly extended the life time and life quality in society.

1.1 History of biomaterials

Biomaterials science consists in the production of materials, with a specific function in a bio-environment, and their study from the chemical-physical point of view to the biological perspective. It therefore requires strong crossover between different scientific disciplines: the collaboration between materials science, chemistry, engineering, biology (cellular, molecular and genetics) and medicine (embryology, anatomy, physiology) is a fundamental prerequisite for the developing of this kind of materials.

Although the first attempts to restore biological functions, by the introduction of non-biological materials dated at ancient history, that of biomaterials is a relatively young science. Only 60-70 years ago there were no biomaterials in the sense we understand, not even the word "biomaterial" existed and the medical device manufacturers had no formalised regulatory [7].

It is difficult to define when people recognised the concept of deformity; probably, since the origin of human beings, the need to prevent a deficiency or repair wounded tissues encouraged humans to use a large variety of materials. However most of the ancient civilizations did not leave any written records, they passed down their historical events only by the means of orally recorded songs, poetry and sagas. Several mythological stories, from Greek, Egyptian and South-America civilizations, recount people with missing arm, hand, leg, foot, or other parts of the body which have been replaced by "implants" or "prostheses". Because the most frequent surgical intervention concerned bone repair or teeth replace, the most used materials were: wood, nacre, ivory, allogenic and xenogenic bone and, later, leather and metals. In fact, loss of limbs was common for different causes: accident, war, punishment, religious or magical ceremonial amputation. For that reason, as ancient cultures attributed to deities human traits and behaviour, gods could often appear with some "medical devices" for the replacing of the lacking organ. One of the most popular legendary implant bearers was the Greek god Pelops. [8]. This legend has it that Pelops' father, Tantalus, was an Asian prince and a son of Zeus. Once, to test the Zeus' ability to know everything, Tantalus cut up his son, boiled the pieces, and served them to the gods at a banquet. At the banquet the gods refused to eat, except for Demeter, who, distracted by grief for the loss of her daughter, ate the left Pelops’ shoulder. Zeus killed Tantalus and the gods restored him to life, replacing with ivory the part eaten by Demeter [9].[1]

Many other legendary stories tell of organs or limbs replaced with different materials; among these we can find the gold phallus of the Egyptian god Osiris, the right foot of the

---

[1] Tantalus's punishment for his act, was to stand immerged in a lake and tied to a tree bearing fruit, however he could not drink or eat. Whenever he tried to drink, the water receded; the reached for the fruit, the branches moved away from his grasp. This fate was cursed him with eternal deprivation of nourishment.
His name was given to a chemical element by Ekeberg. He wrote "This metal I call tantalum ... partly in allusion to its incapacity, when immersed in acid, to absorb any and be saturated"[9]. The irony is this element has been used in orthopaedic prosthesis for knee, hip and...shoulder.

Aztec deity Tezcatlipōca replaced by an eagle foot (Figure 1.1), the silver four-fingered hand of the Irish god Nuada.

Figure 1.1: The Aztec deity Tezcatlipōca with his right foot replaced by an eagle foot.

The past delivers us not only legendary stories but also archaeological artefacts really employed as "medical device", such as the *Cairo Toe* (Figure 1.2 (a)) constructed of wood and leather. It was found attached to an Egyptian mummy, dated between 1550 and 700 BC. Other examples are the *Greville Chester Great Toe*, an ancient Egyptian phalange prosthesis made from cartonnage, the bronze *Capua Leg* (Figure 1.2 (b)) dated from about 300 BC.

Figure 1.2: *Cairo Toe* (a) and *Capua Leg* (b) archaeological artefacts.

On the other hand, the "first" dental prosthesis comes from Etruscan civilization of around 2,600 years ago. It was a hybrid material made of a cow tooth fixed to the neighbouring patient's teeth by a gold wire [4]. Roman and Greek also tried single iron dental implants;

microscopic analyses revealed strong corrosion and bone reconstruction around the implants, which proved they were implanted during the life-time. The most famous and beautiful art work of dental implantology is now stored in Museo del Oro, in Lima, it is a skull from the Peruvian Mochica culture, with a complete replacement of all teeth with carved rose quartz. Probably the artificial teeth were implanted during the life-time of the person, since some zones around the teeth look like reconstructed bone; however it is not yet confirmed [8].

Those, above described, are only few examples of attempts done with the intent to address the loss of physiologic/anatomic function with an implant. Many other efforts were carried out with more or less success throughout history, but certainly, between the First and the Second World War, the interest for the study and the use of new materials grew up drastically. After the war, surgeons needed inert and durable materials to replace diseased and damaged body; for that reason they started to apply to medical requirements materials originally developed for airplanes, automobiles, clocks, and radios. Thanks to the collaboration between surgeons, scientists and engineers, many materials were tried on the spur of the moment and some of them fortuitously succeeded. Surgeons could take the life of people and these high risk trials, usually, took place where other options were not available. Silicones, polyurethanes, Teflon®, nylon, methacrylates, titanium and stainless steel were the innovative biomaterials [7]. Many materials and procedures, common used today, were born at that time, thanks to the courage, intelligence, guts and creativity of individuals, which started to share their knowledge. We can say they were the parents of the biomaterials science. As an example, few years after the Second World War, an important and fortuitous discovery was made by a Sweden orthopaedic surgeon. He was studying the healing reaction of a rabbit after the implantation of a titanium cage screwed in the bone. Some months later he found the device strongly integrated into the bone and called this phenomenon "osseointegration" [11]. Most of the dental and orthopaedic implants are still made in titanium until today. Furthermore, it is necessary to underline that, at this point of the history, still the term "biomaterials" had not been coined. It is difficult to establish the precise origins of this term. Certainly, it was consolidated trough the early Clemson University biomaterials symposia in the late 1960s and the early 1970s. In fact, these symposia were so successfully in the scientific community that they led to the foundation of the Society For Biomaterials in 1975 [12].

1.2 The evolution of biomaterials

Biomaterials science is a research field in constant growth. In fact, it is still difficult to explain the biological response and the role of a specific material on the tissue regeneration, thus this non full knowledge pushes researcher to produce new materials. Today biomaterials have applications that concern the whole human body and they allow every year the improvement of the quality of life of millions of people.

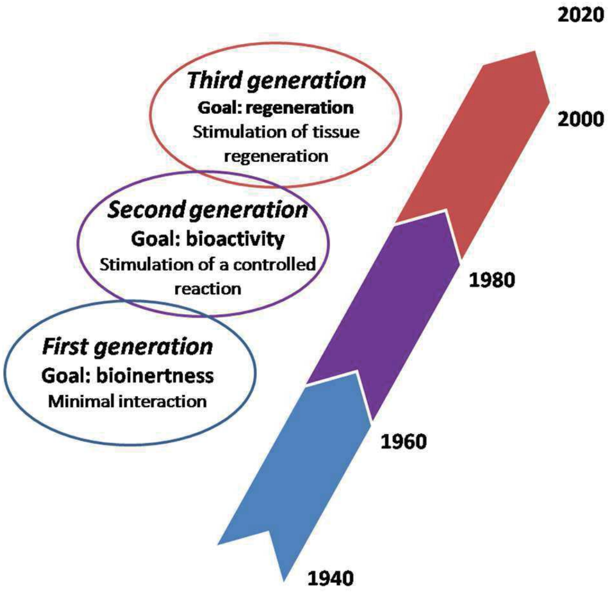

Figure 1.3: Generations of biomaterials.

The development of biomaterials has been divided into three generations in part temporally overlapped (Figure 1.3) [13].

First generation of biomaterials began in the 1950s, when new industrial materials, not developed for medical purpose, were available. It was common to think every artificial materials could provoke adverse reactions, thus they were selected for their physical properties and inertness in a biological environment (bioinertness). Therefore, in order to reduce the corrosion and the releasing ions and particles after implantation, to minimise the immune response and to avoid foreign body reaction, biologically inert or nearly inert materials were chosen. Examples for the first generation biomaterials are:

- Metals (stainless steel and Co-Cr-based alloys, Ti and Ti alloys).
- Ceramics (Alumina Al_2O_3 and Zirconia ZrO_2).
- Polymers (silicone rubber, acrylic resins).

The second generation of biomaterials was materials able to give a controlled interaction with the biological environment, so called bioactive. They were implanted with the aim to induce the desired therapeutic effect. Second generation biomaterials included also bioresorbable materials, with the ability to degrade during the new tissue regeneration and heals; in other words, materials with a degradation rate that could be adapted to the requirements of the specific application. Examples of second generation biomaterials are:

- Polymers (Biodegradable polymers of synthetic and natural origin, such as polyglycolide (PGA), polylactide (PLA)).
- Ceramics (Bioactive glass, glass–ceramics and calcium phosphates (CaPs)).

The third generation of biomaterials has the goal to support and regenerate tissues in the service of tissue engineering and regenerative medicine. The complete substitution of a damaged tissue with a new artificial living one is becoming possible. Thus, biomaterials engineered to control specific biological reactions constitute the modern era in the history of biomaterials.

Biological concepts such as cell-surface receptors, growth factors, control of proteins and cells attachment, stem cells and gene delivery were either controversial observations or not yet discovered in the 1960s, when the pioneers of biomaterials were laying the groundwork of this science. Similarly, they could not design materials with new ideas from materials science in mind such as phase separation, anodization, self-assembly, surface modification, and surface analysis.

Currently, a wide range of materials is routinely used in medical devices. For that reason specialization is common and appropriate: no one researcher can be comfortable synthesizing, characterizing, designing, and fabricating with all these materials. Moreover, all the biomaterials are grouped in two different classes of application: soft tissue and hard tissues replacement. Biomaterial for soft tissues are typically associated with cardiovascular implants and general plastic surgery materials. Biomaterials for hard tissues are whereas represented by those involved in orthopaedic and dental materials. Soft tissue biomaterials researchers are considered polymer experts, while hard tissue biomaterials researchers are thought to focus on metals and ceramics.

The progressive population ageing, with related musculoskeletal disorders, is driving the development of innovative materials for bone implants. Although the production of prosthetic implants is nowadays a mature and well-established practice, the scientific research is constantly evolving with the aim of improving the reliability and effectiveness of the available prostheses, thus increasing patience's' life expectancy.

1.3 Hard tissues biomaterials

This special group of materials consists of highly mineralized and load-bearing tissues of the human body: bone, cement, dentin and enamel. They are subjected to high level of stresses, wear and fatigue. Moreover, the progressive population ageing, with related musculoskeletal disorders, is driving the development of innovative materials for bone implants. Orthopaedic devices include prosthesis (for hip, knee, ankle, shoulder and elbow joints) and fracture fixation devices (as wires, pins, plates and screws). Dental implant is a cylindrical or tapered device, usually made of titanium, implanted in the jawbone to support a dental restoration such as a crown or denture.

Hard tissues biomaterials are classifiable in two main groups:

- Metals
- Ceramics.

1.3.1 Metals

Bioinert metals belong to the first generation of biomaterials, however they are still used for their unique mechanical properties: high tensile and yield strength and resistance to fatigue, creep and corrosion. Thus their common application is the production of load-bearing joints implants. Stainless steel and titanium are the most common metals for such types of devices.

Stainless steels are iron-based alloys, with a minimal percentage of Cr of 10.5%, necessary to avoid the rust. There are several types of stainless steels in use for medical applications, Stainless steel (18Cr–8Ni) was the first used in orthopedic surgery in 1926. For implant applications they must have the resistance to pitting and crevice corrosion from the body fluid. 316L (18Cr–14Ni–2.5Mo) single phase austenitic (FCC) stainless steel is the most popular one for implant applications. The ‘‘L’’ in the designation denotes its low carbon content and as a result it has high corrosion resistance in vivo conditions [14].

Extracted for the first time in 1791 by William Gregor[2], titanium was largely available at the end of World War II, from military application to peacetime uses. A major step forward in the use of titanium for bone tissue implants was the Brånemark discovery of osseointegration [7], described above in the section 1.1. Pure titanium is usually used when corrosion resistance of the device is more important than mechanical properties, as in dental implants. Otherwise, in order to improve mechanical properties, titanium is used in alloys with aluminium and vanadium, Ti–6Al–4V is the most popular. In the recent past, however, it has been found the possibility of any toxic effect due to the dissolution of aluminium and vanadium ions into the body fluid.

Since stainless steel and Ti are bioinert materials, the material- tissue interface is not chemically or biologically bonded. This can cause a relative movement and the growth of a avascular connective fibrous capsule[3] around the implants, which can be rejected very quickly [15].

Magnesium is suitable for revolutionary bioresorbable implants. In general, the bioresorption is a degradation process that involve two different mechanisms: the dissolution, due to the solubility in physiological environment and the involving of cells, like osteoclasts, giant cells and macrophages [16]. In contrats to the other metals used as biomaterials, magnesium and its alloys are eligible for temporary implants, supposed to be completely degraded after the bone healing [17]. However, the degradation rate of magnesium and its alloys is too rapid to match the kinetics of bone healing; in addition, it is possible that corrosion mechanisms occur. To overcome these problems, the coating with a biodegrdable film, able to delay the degradation of the implant, should be an appropriate solution [18].

1.3.2 Bioceramics

Ceramics are inorganic, non-metallic, solid materials consisting of metal, non-metal or metalloid atoms, with interatomic bonding (ionic or covalent), which are generally formed at elevated temperatures. The crystallinity of ceramic materials ranges from highly oriented to semi-crystalline, vitrified, and often completely amorphous (e.g., glasses).

---

[2] William Gregor was a Cornish amateur chemist. He used a magnet to extract the mineral, now known as ilmenite, from a local river. He used hydrochloric acid to extract iron, leaving impure titanium oxide as residue.

[3] This capsule consists of different cellular layer: an inner layer of macrophages, a concentric layer of fibrous tissue and fibroblasts (30–100 μm), and an outer layer of vascularised tissue.

The category of ceramics used for hard tissues repair is named bioceramic, which are subcategorized in:

- bioinert, as alumina (Al_2O_3) and zirconia (ZrO_2);
- bioresorbable, as calcium phosphate (CP);
- bioactive, as hydroxyapatite (HAp, $Ca_{10}(PO_4)_6(OH)_2$), bioactive glasses and glass-ceramics.

Their common clinical applications include their use in orthopedics as bone plates and screws, total and partial hip components, coatings on metal prosthesis, space fillings of diseased bone, and vertebra prostheses and spacers, iliac crest prostheses, etc [14].

Bioinert materials, as described in the previous section, belong to the first generation of biomaterials. The drawback of bioinert materials, as for metals, is given by their tissue-implant interface. In fact, they do not cause adverse reactions by the host tissues, however they inevitably get covered by a fibrous capsule when implanted in the human body. The capsule is not bonded with the implant, and therefore micro-movements may occur, which could deteriorate the functionality of the prosthesis or the original tissue properties at the interface, or both. In order to limit the relative movements between implant and host tissue the modification or coating of their surface is recommended.

Calcium phosphates are the largest group of bioresorbable material, mainly thanks to their composition, similar to that of bone. As described in the previous paragraph (1.3.1), the basic difficulty with this material is the matching of the resorption rate with the growth of the new bone tissue. In fact, the strength and the stability of the interface between the biomaterial and the bone in formation should be stable during the degradation process. In addition, for calcium phosphate implant, it is necessary to take into account that its mechanical properties are different from that of bone, because in the latter, the presence of collagen gives some elasticity to the tissues [19]. In order to adjust the dissolution rate and the mechanical properties, several methods can be used, such as the addition of doping elements to the biomaterial or the coating with bioactive materials. Their activity is intermediate between the bioinert and the bioresorbable materials. Bioactive materials, bioactive glasses, ceramics and glass-ceramics, are able to bond the surrounding tissue. Obviously, the bonding kinetic, strength and mechanism are different according to the composition; in fact, small changes in the composition can have remarkable effects on the activity of the material [15].

Among bioactive material, hydroxyapatite is one of the most widely studied for the bone healing, since it is the main inorganic component in calcified hard tissues, as bone and teeth. In particular, bone apatite consists in a poorly crystalline HAp and other calcium phosphate (CaP) phases that have trace elements in their structure. From one of the first publication on the use of HAp for biomedical application [20], up to now, a literature of countless papers has been issued. Originally, researchers believed the use of crystalline stoichiometric HAp ($Ca_{10}(PO_4)_6(OH)_2$) was the best choice, in order to avoid potential toxic impurities. Nowadays a poorly crystalline HAp, named biomimetic hydroxyapatite, is preferred [21]. Therefore, various ions, singly or multiply in many combinations, have been used for the doping with the aim to improve its biological activities [22].

Belonging to the category of bioactive ceramics, bioactive glass is the first completely synthetic biomaterial without any problems of bonding to bone. Bioactive glasses are a group of surface reactive glasses able to release ions in a biological local environment, which can then activate different biological responses, leading to the formation of new bone [23]. The first bioactive glass to be commercialized was Bioglass®, also known as 45S5 glass, it was developed by Professor Larry Hench in 1969 to comply the request of a US Army Colonel just returned from Vietnam, who asked for a material that would not be rejected by the body [24][4]. Its work was explained in the first paper published in 1971 [25], where *in vitro* and *in vivo* tests where summarised. *In vitro* test revealed the production of a hydroxyapatite thin layer on the surface of the material into the testing solution, equivalent to the layer developed at the interfacial bonding of the implant to bone, during the *in vivo* tests. Consequently, no fibrous encapsulation occurs on the bioactive material, as in the case of a bioinert one, on the contrary, their surface directly bonds to the new host tissues. This strong adhesion between the implanted material and the living tissues drastically reduces the chance of rejection. Furthermore, after few months, new bone tissue will be born, connected to the implant through a strong bonding interface by the means of a process named bioactive fixation [25,26].

---

[4] In 1967 Hench worked on glass material and their interaction with radiation, at University of Florida. In that year he met the US Army Colonel during the bus ride to Bolton (New York), where the Army Materials Conference was to take place. The Colonel was not interested on the interaction between glass and radiation; in fact, he was just returned from Vietnam, where every week hundreds of limb were amputated because of the rejection of metals and polymers implants used to repair the body. Thus, he asked to Hench: *"If you can make a material that will survive exposure to high energy radiation can you make a material that will survive exposure to the human body?... We can save lives but we cannot save limbs. We need new materials that will not be rejected by the body."* [24]. Once back in Florida, Hench began his studies on a special type of glass, he supposed and demonstrated that glasses containing critical amount of Ca and P ions would not be rejected. Two years later, when this material was tested *in vivo*, Bioglass® was born. The Doctor, who carried out the test, reported: *"These ceramic implants will not come out of the bone. They are bonded in place. I can push on them, I can shove them, I can hit them and they do not move. The controls easily slide out."*

Finally, glass-ceramics have properties intermediate between glass and ceramics, in fact, they are made by the controlled crystallization of a glass to obtain a polycrystalline ceramic. Glass-ceramics are ideal materials for create bioceramics with improved chemical durability and mechanical properties, thanks to the contribution of the crystalline phase. It is possible to control the properties of bioceramics by controlling the type and content of the mineral phases. Glass-ceramics based on the formation of an apatite crystalline phase, such as apatite glass ceramics, apatite–mullite glass ceramics, apatite–wollastonite glass ceramic, are preferred because they are close to natural bone in their chemical composition [23]. There may be a residual glassy matrix, which could undergo a process of phase separation. Whereby it is possible to obtain one or more crystalline phases suspended in a glassy matrix [15]. Therefore, crystalline phase and glass composition have a heavy impact on the biological behaeviour of the glass-ceramic.

a *Hydroxyapatite*

Hydroxyapatites are widely applied as biomedical materials. Thanks to its excellent biocompatibility, osteoconductive properties, and similarity to the inorganic component of human bones, HAp is used as bone fillers, bone tissue engineering scaffolds, bioactive coatings, soft tissue repairs, drug/protein/gene loading and delivery systems. HAp materials can be potentially used in cell targeting, fluorescence labelling, imaging and diagnosis. In addition, HAp has been studied as a model to mimic the biomineralization process [27].

Stoichiometric HAp, with composition $Ca_{10}(PO_4)_6(OH)_2$, is the most stable calcium phosphate with a Ca/P ratio of 1.67. The crystal structure of HAp most frequently encountered is hexagonal, having the P63/m space group symmetry with lattice parameters of $a = b = 9.432$ Å, $c = 6.881$ Å, and $\gamma = 120°$ [27,28] . The structure consists of an array of PO_4 tetrahedrons held together by Ca^{2+} ions. The latter can be positioned in two different sites: four Ca^{2+} cations (Ca(I)) and OH^- anions are positioned along columns parallel to the c axis; the remaining six Ca^{2+} (Ca(II)) are associated with the two hydroxyl groups (OHs) in the unit cell, where they form triangles centered on, and perpendicular to, the OH axis and lying on the mirror planes. HAp can also exist in monoclinic form with space group P21/b and lattice parameters $a = 9.4214$ Å, $b = 2a$, $c = 6.8814$ Å, $\gamma = 120°$. The major difference between the monoclinic and hexagonal HAp is the orientations of the OHs. In monoclinic HAp, all of OHs in a given column are oriented in the same direction, and in the opposite direction in the successive column, while in hexagonal HAp the adjacent OHs are oriented in opposite directions [27].

Stoichiometric HAp is difficult to be resorbed in physiological enviroment. In fact, the biological hydroxyapatite, which is mainly present in bones and teeth, contains many impurities, because its crystallography and chemistry allow different substitutions in both anionic and cationic positions. For example, Ca^{2+} ions can be easily replaced by for example Sr, Mg, K, Na, and Fe cations; while phosphate anions can be partially replaced by carbonate groups (CO_3^{2-}), silicate (SiO_4^{4-}), and so on; finally the OH^- groups may be replaced by F^-, CO_3^{2-} and O^{2-}. Therefore, it has been demonstrated an increasing of the degradation rate of HAp with co-substituted essential trace elements and the dissolution rate of HAp grew with the increasing of the ion substitution degree [21]. Furthermore, these substitutions have a significant effect in the biological performances, as resumed in the Table 1.1.

Table 1.1: Biological roles of some ions.

Ion	Biological role
Na	Bone metabolism and osteoporosis
Mg	Tissue calcification
K	Mineralization
F	Calcification of calcium phosphate in bone formation
Sr	Stimulation of osteoblast differentiation and inhibition of osteoclast activity
Fe	Increase bone health
CO_3^{2-}	Biocompatibility and resorbability
Si	Promotion of collagen type I synthesis, osteoblast differentiation, and bone repair

Other than the incorporation of essential elements, it is possible to promote the bone formation and mineralization by the morphological modification of the medical device. HAp bioceramics, with nanoscale crystal sizes and micro-/nanostructured surface topography, show better bioactivity, promote adhesion, proliferation, and osteogenic differentiation of bone marrow stem cells (BMSCs) and osteoblasts and, subsequently, to stimulate bone [29].

The main limitation of the use of HAp, that is common to almost all bioceramics, is their poor mechanical properties: they are usually brittle, rigid and low wear resistant. Therefore, their main applications are the filling of small bone defects and the coatings of metallic prostheses and periodontal implants [28]. HAp coated metal implants show a very good fixation to the host tissue, because HAp favours bone cell attachment, while the bulk properties of the metal (e. g. titanium) are retained. The biological interaction of calcium and phosphate ions released by the HAp promote the formation of a good interfacial strength between the implant surface and the bone, leading to the osseointegration. Furthermore, the deposition of nanometric particles reduces the healing time [30].

The biological reactivity of HA is closely related to its composition, crystallinity and microstructure. In fact, while a stoichiometric and highly crystalline HA is almost stable in a biological environment, a poorly crystalline and/or chemically substituted one can undergo a fast degradation. The dissolution process begins from structural defects such as dislocations and grain boundaries. During this process, dissolution and precipitation reactions occur, as summarised below [28]:

1. Partial ionic dissolution of the HA coating and subsequent increasing of Ca^{2+} and phosphate ions concentration in the surrounding fluids.
2. Precipitation from solution of nanocrystalline and/or amorphous calcium phosphate (ACP) onto the ceramic surface.
3. Ion exchange between HA crystals and surrounding tissue.
4. Structural rearrangement and formation of carbonated calcium phosphate crystalline layer incorporating a collageneous matrix.
5. Solution-mediated effects on cellular activity.
6. Deposition of either the mineral phase or the organic phase, first without integration into the ceramic and then with integration.
7. Cell attachment and proliferation.
8. Cell differentiation to osteoblastic phenotype.
9. Extracellular matrix formation.
10. Bone growth and remodelling.

b *Bioactive glasses*

Bioglass®, also known as 45S5 bioactive glass, is the name of the first synthetic material able to bond with bone. The composition is reported in Table 1.2. Developed in the late

1960s by Larry Hench, Bioglass® has been in clinical use since 1985. It is a soda–lime–phosphosilicate (Na_2-CaO-P_2O_5-SiO_2) glass and the formula 45S5 has a specific meaning: 45 wt.% S, wich stands for SiO_2 (network former), and 5:1 is the ratio CaO:P_2O_5 [15]. What traditional glass and bioactive glasses have in common is their amorphous structure and the thermal behaviour. In fact, both of them have a glass transition range (T_g), wich is the temperature range where the system varies from a supercooled liquid to a no long-range order solid [31]. However, three important features distinguish bioactive glasses from traditional soda-lime-silica glasses:

1) less than 60 mol% SiO_2;
2) high Na_2O and CaO percentage;
3) high CaO/P_2O_5 ratio.

Table 1.2: Composition of 45S5 Bioglass®.

Composition	**SiO_2**	**Na_2O**	**CaO**	**P_2O_5**
Mol %	46.13	24.35	26.91	2.60
Wt %	45.00	24.50	24.50	6.00

Like for hydroxyapatite, the composition of bioactive glasses is changing; in fact, in order to improve biological performances, numerous ions have been introduced.

As regards the bioactive glass structure, there are three peculiar components to be taken into account; network formers, network modifiers and intermediate oxides.

Network formers, typically three or fourfold coordinated, include silica (SiO_2), phosphorus pentoxide (P_2O_5). The basic building block of silicate glasses is the SiO_4^{4-} tetrahedron, each one can be connected to neighbouring SiO_4^{4-} tetrahedrons through Si-O-Si bonds, named bridging oxygen atoms (BO). However, the presence of network modifiers varies the glass structure by the conversion of bridging oxygen atoms, with predominant covalent character of the bond, into non-bridging oxygen atoms (NBO), with predominant ionic character of $Si\text{-}O^-M^+$ (where M^+ is a modifier cation) [32]. Network modifiers are, generally, the oxides of alkali or alkaline-earth metals. Modifiers cations present coordination numbers higher than the former cations, such as: sodium, calcium or strontium, with coordination number of 6 or 7 [33,34].

The glass structure can be estimated on the basis of the composition, by the means of the network connectivity model (NC), which predicts the number of BO for each SiO_4^{4-} tetrahedron. NC can be calculated by the following equation 1.1 [35]:

$$NC = 2\frac{BO - NBO}{G} \tag{1.1}$$

where BO is the total number of bridging oxygens per network-forming ion, NBO is the total number of non-bridging oxygens per network modifier ion and G is the total number of glass-forming units.

Considering a bioactive glass, with composition SiO_2-P_2O_5-M_2O-M'O (where M_2O and M'O are network modifiers), assuming a maximum of four bridging oxygen atoms per silicon atom, of which the nonbridging oxygen atoms formed by modifiers are subtracted, knowing that P_2O_5 is present as orthophosphate PO_4^{3-}, charge-balanced by modifiers cations, it is possible to solve the following equation 1.2 [31,35]:

$$NC_{Si} = \frac{4 \times SiO_2 + 6 \times P_2O_5 - 2 \times (M_2O + M'O)}{SiO_2} \tag{1.2}$$

Usually, bioactive glasses have a 2 <NC <3, while for vitreous silica the connectivity is 4. Finally, intermediate ions, such as Mg, Zn, Co and Ni ions, have a crystal field strength intermediate between that of network formers and that of the modifiers. Generally, intermediate oxides may reduce the tendency of the glass to crystallize, thus the bioactivity of the glass improves. However, it is difficult to predict their behaviour because they can act like network modifiers or, if they enter the backbone of the glass structure, they act more like network formers. In general, the behaviour of an intermediate oxide depends not only on the network connectivity, but also on the field strength of the others modifiers present in the surrounding: higher is the field strength of the other cations, higher will be the coordination number of the intermediate, thus its character will be more similar to a modifier [36]. Therefore, it is necessary to analyse each case individually.

The interaction between a bioactive glass and the biological environment is a multi-stage process, stimulated by the dissolution products of the bioactive glass. As proposed by Hench [37], it is possible to differentiate the mechanism in two sets of steps. The first five steps involves only inorganic reactions occurring at the glass surface and leads to the formation of a biological HAp layer. The following seven steps regards the cellular effects at the bioactive glass interface.

1. Rapid ion exchange of alkali-metal cations (e.g. Na^+, Ca^{2+}) with H^+ (or H_3O^+) from the body fluid, with the creation of silanol bonds on the glass surface:

   $$Si\cdots O\cdots Na^+ + H^+ + OH^- \rightarrow Si\cdots OH + Na^+ + OH^-$$

   The pH increases and a silica-rich region is formed near the glass surface. In this step also phosphate ions are released.

2. The increasing of the pH allows the breaking of the Si–O–Si bonds, soluble SiO_2 are lost in the fluid in form of $Si(OH)_4$, and of Si–OH (silanols) are formed at the glass-solution interface:

   $$Si\cdots O\cdots Si + H_2O \rightarrow Si\cdots OH + OH\cdots Si$$

3. Condensation and repolymerisation of the Si–OH bonds to create a silica-rich layer:

   $$HO\cdots Si\cdots OH + HO\cdots Si\cdots OH \rightarrow HO\cdots Si\cdots O\cdots Si\cdots OH + H_2O$$

4. Ca^{2+} and PO_4^{3-}, present inside the glass and the body fluid, migrate to the surface through the SiO_2-rich layer, forming an amorphous $CaO–P_2O_5$ film on the surface of the SiO_2-rich layer.

5. Crystallisation of the amorphous layer by incorporation of OH^- and CO_3^{2-} from fluid to form biological HAp.

6. Adsorption-desorption of proteins.

7. Macrophages action.

8. Attachment of osteoblast stem cells.

9. Differentiation and proliferation of stem cells.

10. Generation of matrix.
11. Crystallisation of matrix.
12. Proliferation and growth of the bone tissue.

The second set of reactions is not so clear. Biochemical process responsible for the gene activation depends definitively on the silicon and calcium ions concentration, thus on the glass composition. The absorption-desorption of proteins is actually a high and dynamic process that occurs during all dissolution process, step 6 is only the point at which the adsorption-desorption process reaches a degree of equilibrium. This process involves also other biological moieties (e.g. sugars, phospholipids, amino acids). Only certain proteins bind selectively and irreversibly and it happens during both the formation of the silica and HAp layers. Furthermore, it is influenced by the ions released by the glass, surface morphology, particle size, roughness as well as protein composition and concentration.

Hench used a "Phase Diagrams for Ceramics" to design the early bioactive glass composition: 45% SiO_2 – 24.5% Na_2O – 24.5% CaO – 6% P_2O_5 was selected to supply a large quantity of CaO with some P_2O_5 in a Na_2O – SiO_2 matrix [23]. The composition is very close to a ternary eutectic temperature and thus is easy to melt. A compositional diagram of the SiO_2–Na_2O–CaO system is shown in Figure 1.4 [35]. All compositions have a fixed 6 wt% of phosphate. Glasses, the composition of which falls into the region A, are able to bond the bone. For this reason, region A is named bioactive bone-bonding boundary. "Normal" silicate glasses (such as window or bottle glass) belong to region B and are effectively bio-inert and their implantation would result in fibrous tissue encapsulation at the implant-tissue surface. Glasses within region C are resorbable, they degrade too rapidly and disappear in 10 to 30 days. Region D contains compositions with a silica content too low to form a glass network, so they are not technically feasible [15]. Glasses within the dashed line (region S) strongly adhere to collagenous (soft) tissue as well as the inorganic part of bone. Region E corresponds to 45S5 Bioglass composition.

High content of silica means high network connectivity, because there are many BO (silica tetrahedrons covalently bonded to other silica tetrahedrons via –O–Si–O bonds); thus the glass is durable in body fluid. For this reason melt-derived glasses with more than 60 mol% silica are not bioactive. The adding of network modifiers, as described in the previous section, reduces the NC, allowing an easier degradation of the material inside the body fluid [15,35].

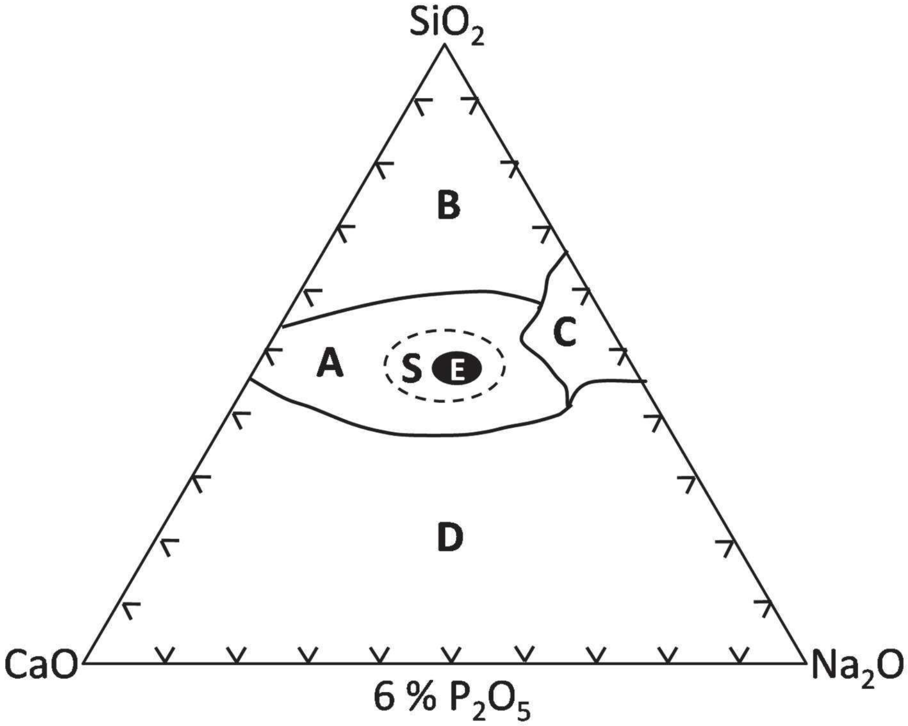

Figure 1.4: Bioactivity map of compositions in the SiO_2–Na_2O–CaO system (6 wt% of P2O5) showing regions of bioactive response.

c *Glass-ceramics*

A glass-ceramic is a glass containing micro- and nanocrystalline phases. Does not exist any normative that determine which type of composition is definable glass-ceramic. It is suppose to be a glass-ceramic a glass wich contains from 1 % to 80 % (v/v) of crystalline phases [38]. During the development of bioactive glasses it was demonstrated that a bioactive glass, with a composition suitable to obtain a glass-ceramic, when heat treated to create crystalline phases, it can retain its bioactivity [23]. It was an important discovery for the improving of the mechanical properties of the bioactive glasses. Various compositions based on silicate glass-ceramics have been developed from then. Among them apatite glass-ceramics and apatite-wollastonite glass-ceramics were developed. In 1977 Professor Gross and his colleagues implanted in animal models a bioactive apatite glass-ceramics, based on 45S5 Bioglass composition with small amount of K_2O and MgO. With these experiments, they demonstrated that the glass-ceramic was able to bond the bone with a mechanical strong interface and with improved bioactivity [39]; in fact, a biological HAp layer was formed within one hour of implantation. This bioactive glass-ceramic, marketed as Cerevital®, however, was not so successful, because the instability of the crystal phase boundaries and the resorption of the material limited the clinical usage.

A multiphase bioactive phosphosilicate was developed by Yammamuro and Kokubo in the 1980's; it was an apatite/wollastonite (A/W) glass-ceramics with a residual glassy matrix. Mechanical strength, toughness, and stability of AW glass-ceramics in physiological environments were excellent and it was able to bond the bone with a high interfacial bond strength [40].

The reaction mechanism that characterizes the bioactivity of these glass ceramics has some differences with respect to that of apatite or bioactive glasses. First of all, a dissolution process of Ca^{2+} ions takes place in the surrounding body fluid, which is attributed to the high CaO content in the glass ceramic. Si–OH groups on the surface of the glass-ceramic immediately combine with Ca^{2+} and phosphate ions in the fluid to form an amorphous calcium-silicate-phosphate layer, with a low Ca:P ratio. Which then crystallize in bone-like apatite, incorporating minor ions such as Na^{+} , Mg^{2+} , and Cl^{-} . After the formation of the HAp, the mass transport from the surrounding body fluid supplies the additional requirements of Ca^{2+} and PO_4^{3-} ions. The apatite present in the glass ceramic does not dissolve any ions, because the body fluid is already supersaturated for the apatite, for this reason the PO_4^{3-} ions required are only supplied from the surrounding body fluid [40]. Furthermore, in these glass ceramics, the formation of a SiO_2 gel layer, as is the case of the bioactive glasses from the SiO_2–Na_2O–CaO–P_2O_5 system, was not observed [23]. Moreover, by comparing the dissolution rate of Ca^{2+} and silicate ions from glass ceramic A/W with those from the Bioglass and apatite glass ceramic, it was revealed that the calcium and silicate ions were dissolved from both of the wollastonite and the glassy matrix.

CHAPTER 2

Bioceramics coatings

A wide range of material is available for bone-related devices. Each one exhibits specific properties that make their use particularly advantageous for certain applications. However, a single type of material is usually not enough to satisfy all the requirements for a successful bone-related implant. Despite their excellent biological performances, bioceramics have indeed poor mechanical properties; consequently, they cannot be used in load-bearing applications. On the other hand, metals like stainless steel or titanium and its alloys, which present advantageous mechanical properties, such as high tensile strength, resistance to fatigue and deformation, are largely used for biomedical devices for hard tissue replacements. However, metallic materials are not osseoconductive, thus they can be subjected to a fibrous encapsulation process and can have problem with corrosion resistance in biological fluid [41]. All these problems are related to the surface of the implant, were biological reaction occur on. In order to overcome these limits, while maintaining the favourable bulk properties, it is possible to modify the surface of the implant by the deposition of a bioactive coating [30]. Bioactive ceramic coatings onto metallic implants have these scopes:

- To promote a rapid bone fixation of the devices by enhancing bone growth and creating a strong interface.
- To act as a protective barrier, minimizing or preventing metallic ion release and reducing the risk of corrosion.

The features and properties of the achievable film depend on both the chosen bioceramics and deposition technique. A wide range of bioceramics, from calcium phosphates to bioactive glass and glass-ceramics, are eligible, as reported in Chapter 1.

The manufacture of high quality coating on a metal substrate is a complex issue. The choice of the material and the deposition technique should be a careful balance of the most critical characteristics, collected below:

- **Crystallinity**. The presence of amorphous phases, which exhibit higher solubility in aqueous medium, is desirable to accelerate bone formation. However, too high dissolution rate compromises the stability and increases the risk of failure. Consequently, crystalline phases are necessary to ensure a term stability of the implant in clinical use [42]. Therefore, to prepare implants with predictable properties it is necessary to design and control the crystallinity and purity of the coatings.

- **Surface topography**. Denser is the microstructure of the coating, less are the problems of cracking or degradation. However, rough, textured, and porous surfaces could stimulate cell attachment and formation of an extra-cellular matrix. In particular, the combination of sub-microscale surface roughness, with microscale and nanoscale features, can stimulate both the adhesion of proteins, involved the regulation of osteoblast proliferation, and the adhesion and differentiation of cells [43,44]. An optimum coating porosity and roughness are important for in-growth of bone cells, conversely the accumulation of macropores at the substrate/coating interface leads to a weakening of the coating adhesion.

- **Mechanical properties.** Good adhesion, high hardness and high toughness are necessary to decrease residues generated during the functional loadings, which can be dangerous for the organism, and to prevent mechanical failures under load conditions [41].

A huge number of micro and nanocoatings methods are suitable for the surface modification of implants for hard tissues replacement. The deposition technique shall be selected on the base of the following criteria:

- ✓ minimum influence on the physical and structural properties of material chosen for the coating;
- ✓ no change of the properties of the substrate;
- ✓ no spallation of the produced film.

Methods available for the deposition of bioceramic coatings have been classified as physical and chemical technique. The most used for these types of coatings are listed below [41].

- ✓ Physical methods:
    - ➢ Plasma spray

    - Physical vapour deposition (PVD):
      - Sputtering:
      - Ion beam assisted
      - Pulsed Laser

- ✓ Chemical methods
    - Chemical vapour deposition (CVD)
    - Sol-gel
    - Electrophoretic

Plasma spray, is based on the production of a plasma in which the material to deposit is injected, usually in powder form. Inside the plasma the particles are melted and accelerated towards the substrate, were they stick and condense. The film is formed by the overlaying of layers of liquid droplets, softened material domains, and hard particles. The density, temperature, and velocity of the plasma are important factors in the formation of a coating. Its composition and structure depend on process parameters, such as plasma gas, particle size of the powder and cooling rate. The advantages of this technique include high deposition rates, ability to coat large areas, thick deposits, low capital cost, and low operating cost. However, it is not possible to coat homogeneously porous surfaces or complicated substrates.

Physical vapour deposition contains a series of technique for the deposition of thin films, based on the vaporization of a solid material and its condensation on a substrate. The main difference between them is the process which leads to the vaporization. In sputtering deposition, atoms and molecules are ejected from the target by bombardment with high-energetic ions. The applying of a specific magnetic field to a diode sputtering target allows to increase the ionization efficiency and the ion current density; consequently, this source provides relatively high deposition rate. The obtained films are thick, dense and with high purity.

In ion beam assisted deposition (IBAD) technique the material to be deposited is vaporised by heating or sputtering or carrying out another PVD technique. The as obtained vapour deposits as a film on a substrate. An ion source is focused on the substrate to modify the properties of the growing film by the bombardment (and the reacting if the ions are not inert). The ion bombardment allows to control morphology and crystallinity of the film.

Pulsed laser deposition (PLD) is based on the interaction of a laser source and the material to be deposited, that causes the ablation of the material and the formation of a plasma, which expands and deposits on a substrate. Further details of this technique will be provided in the next paragraph.

Among chemical technique, CVD involves different types of heterogeneous chemical reactions between a gaseous reactant and the surface of a heated substrate, depositing a film on the same substrate. Chemical reactions can be pyrolysis, oxidation, reduction, hydrolysis and so on. The deposition temperature is a key parameter for the controlling of dynamics and kinetics of coating process.

Sol-gel coating involves multiple subsequent procedures. First of all, the preparation of sol by the generation of ultrafine particles in a liquid medium takes place by the hydrolysis and condensation of a metal alkoxide in a solvent (water or alcohol), in presence of acid or basic catalyst. Then the sol is subject to the ageing, in order to obtain the opportune viscosity. At this stage, the sol is ready for the coating process, during which the sol-gel transition occurs. Some possible coating process are casting, spinning, dipping, spraying and so on. After the drying, the specimen is usually heated to obtain the desired product. The main advantages of this technique are the possibility to coat big substrate, also with complex geometries, and the chance to entrap different compounds and biologically important molecules.

The electrophoretic deposition (EPD) is based on the movement of charged particles under an electric field into a colloidal suspension. Particles are deposited on the electrode with opposite charge. This technique will be more accurately described in section 2.2.

2.1 Pulsed Laser Deposition

Pulsed laser deposition is based on the interaction between a pulsed laser beam and a solid target material. The interaction causes the vaporization of the superficial layers of the target through a complex process named ablation. The vapour, termed plasma, is highly ionized, electrically neuter and composed of atoms, molecules, ions, electrons and clusters. Laser ablation experiments can be carried out in different ambient background, i.e. vacuum, background inert or reactive gas and liquid. The laser can have different pulsed duration, i.e. nano, pico or femtosecond. The principles of laser ablation are the same, however it affects the plasma expansion and the characteristics of the obtained material. When the ablation takes place in liquid environment, a colloidal solution of nanoparticles or nanostructures is obtained. This method is called pulsed laser ablation in liquids (PLAL) and more complex phenomena occur. In fact, during the PLAL the plasma, generated at the target-liquid interface, is confined and rapidly cooled by the surrounding liquid and its expansion causes the formation of a supersonic shockwave (SW). The SW propagation induces an additional pressure on the plasma, which reaches a high temperature, high pressure and high density (HTHPHD) state [45]. The pressure gradient induces the formation of a cavitation bubble (CB), which contains the ablated material. In the CB the material can reacts also with the liquid species at the bubble boundary and, after the CB collapse, it is released in the liquid in form of nanoparticles.

Whereas, during a pulsed laser deposition (PLD) experiment, the plasma expands in vacuum or in gaseous environment towards a substrate, on which it deposits and grows as a nanostructured thin film[5].

In Figure 2.1, a typical schematic representation of a PLD set up is shown. PLD is carried out in a vacuum chamber, where a nanosecond pulsed laser is focused on the target, which is continuously rotated in order to avoid piercing and to improve the morphology of the deposited film and the substrate is positioned in front of the target. Additional optical elements are used in order to direct and focus the laser beam on the target surface.

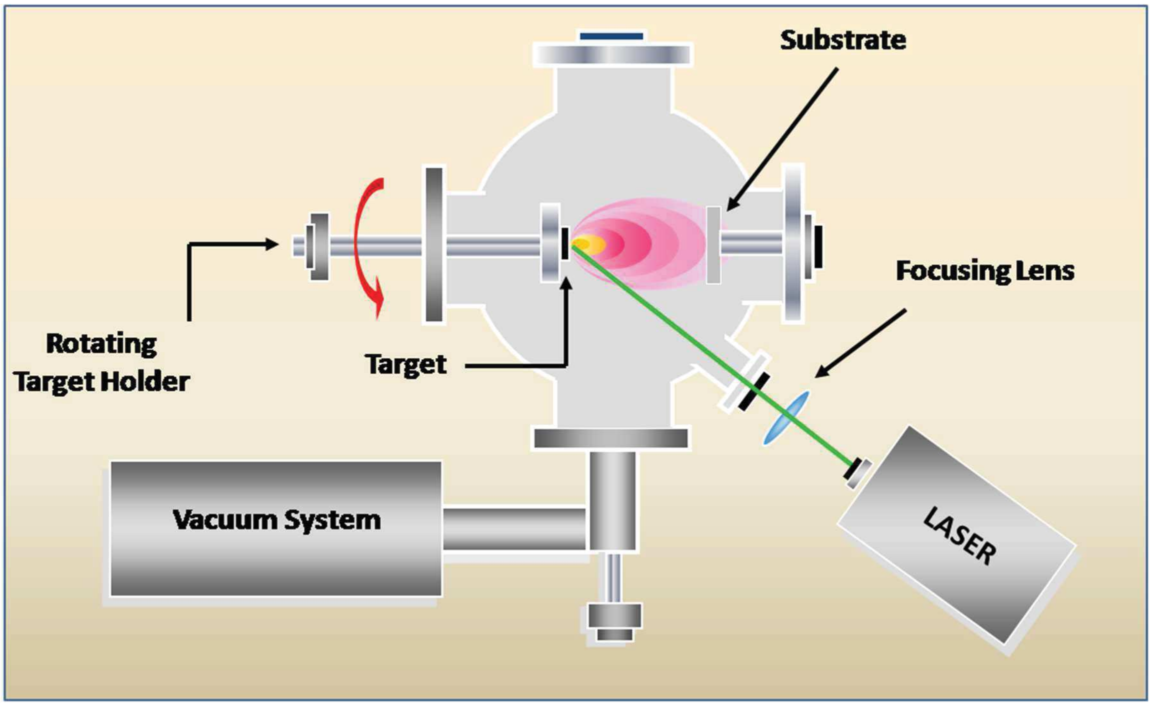

Figure 2.1: PLD set-up.

---

[5]. Since in this work PLD was performed in vacuum with a nanosecond pulsed laser, the deposition mechanism will be explained only related to this condition.

The use of this technique has a number of advantages; some of them are listed below [46].

- ✓ It is possible to ablate almost any material and combination of different material
- ✓ A considerable freedom in the geometry is possible since the laser is not part of the vacuum system.
- ✓ The congruent transfer of the composition from the target to the film is allowed.
- ✓ The control the deposition rate, hence the film thickness, is possible.
- ✓ The control of roughness and crystallinity.
- ✓ PLD is an environment-friendly technique since no by-products are originated, no solvent and toxic reagents are used.

2.1.1 Laser-matter interaction: plasma generation and expansion

The interaction between a laser photon and a material causes the absorption of the former. In few ps the energy is transferred to the electronic system directly, if the material is metallic, or to the lattice in non-metallic systems. The absorption process is followed by thermal diffusion process, which leads to vaporization and plasma formation during the pulse time [46]. The heating begins within the penetration depth of the material ($\delta_p = 1/\alpha$, where α is the optical absorption coefficient) and is fast and strong [47]. This suggests that all target components evaporate in the same time, irrespective to their binding energy. Matter of fact, the congruent evaporation of multielemental target occurs only if the following condition is verified:

$$l_T < \delta_p$$

where l_T is the thermal diffusion length, which is $l_T = 2\sqrt{D\tau}$. D is the thermal diffusion constant and τ is the laser pulse duration.

Since the laser-matter interaction is a very complex process, strongly dependent on pulse duration, laser wavelength and energy and target material, different theories have been proposed regarding the matter removed after the laser irradiation. Most of the available models are based on the ablation of metals or semiconductor materials. This is because theory on the nanosecond ablation of metals are complicated enough that to make an accurate model on the ablation of complex system is utopia. Nevertheless models valid for metals may be adapted to bioceramics materials.

One of the first important attempt to explain the interaction laser-matter and the following plasma formation and expansion was made in the late '90s by Miotello and Kelly. They, by the means of a semiempirical approach, suggested that the interaction of a nanosecond pulsed laser beam with a material causes the so called phase explosion (or explosive boiling). This process consists in homogeneous nucleation of vapour bubbles upon rapid heating of a metastable, superheated liquid that undergoes a transition to a mixture of vapour and equilibrium liquid droplets, well separated in time [48,49]. However, in the course of time this theory has been controverted. Perez at al. [50], for example, declared phase explosion, as intended by Miotello and Kelly, impeded during a nanosecond laser ablation. Perez, in fact, supported a process called trivial fragmentation: a near-equilibrium dissociation of a homogeneous, supercritical fluid. They used a two-dimensional molecular- dynamics model to demonstrate that the nanosecond ablation process of solid characterized by a large optical penetration depth (as ceramics) is determined by a local level of inertial confinement. They found three different regions in the ablating material associated to three different mechanism of ablation, as a function of increasing penetration depth. The ablation mechanism can be individuated with the thermodynamic trajectory of the ablated material in a ρ–T–P (density – temperature – pressure) space. In Figure 2.2 the simulation of the time evolution of the system is reported in a ρ–T plane for different y_0 depth below the target surface.

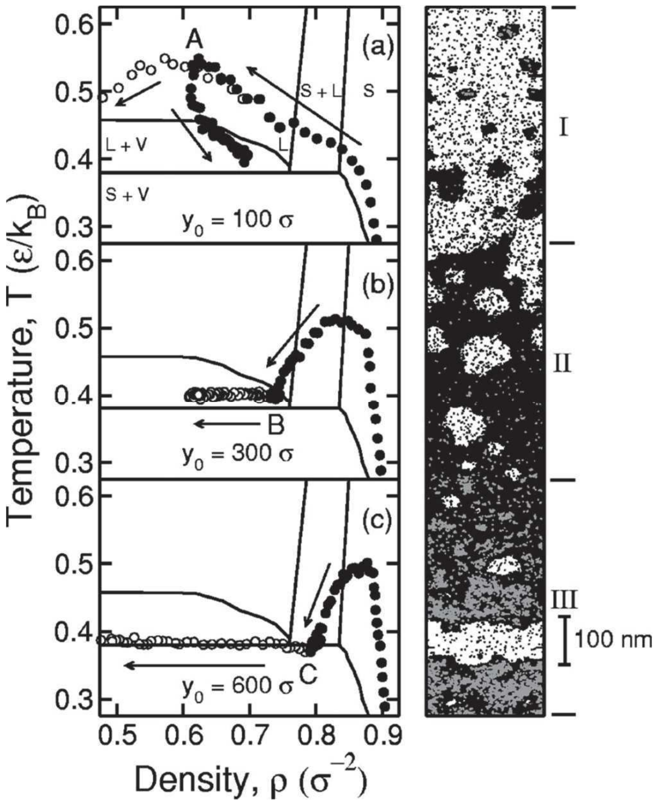

Figure 2.2: Simulation of the time evolution of the system [50].

First region is characterised by a rapidly expanding mixture of gas and liquid droplets, coming from a trivial fragmentation mechanism. Therefore, because of the limited inertial confinement near the surface, the solid expands almost freely in the vacuum, a solid-liquid region can be achieved then the molten material can heat until a supercritical state, and nucleate as clusters. In the second region, down into the plume, the inertial confinement starts to grow. The heating is approximately at constant volume and the expansion takes place during the cooling, the system melts and at the end enters the liquid-vapour boundary region where it is possible to observe an homogeneous nucleation of gas bubbles in a slowly expanding melt. This is an indication of a phase explosion mechanism (different from that proposed by Miotello and Kelly). Finally, in the region further down in the plume, due to the increased inertial confinement, mechanical expansion is slow enough that thermal diffusion becomes an additional cooling process. Consequently, the material expands within the solid-liquid boundary region where heterogeneous nucleation of gas bubble occurs. If the cavities coalesce, the ejection of large piece of material is observed. [50].

During the ablation in ns regime, also the plasma interacts with the laser beam, mainly by inverse Bremsstrahlung [46,47,51]. The inverse Bremsstrahlung process consists in the absorption of a photon (of the laser beam) by a free electron, inside the plasma, during a collision with a nucleus. During this collision, the oscillatory energy of the electron is converted to kinetic energy [52]. The expansion of the plasma in vacuum is approximately adiabatic [46] and considered an ellipsoid [53]. In fact, the plasma expands in the three spatial directions, but preferentially along the direction perpendicular to the target surface, because there is a strong difference in pressure gradients in axial and radial directions: the plasma expands in the direction of maximum pressure gradient. This is the reason why the plasma produced during PLD in vacuum, of elongated shape, is also called "plume". The plume expansion dynamic in vacuum was extensively investigated by Anisimov et al. [53]. He considered the plume expansion similar to the expansion of an elliptical, neutral gas cloud. At the beginning of the expansion, the plume energy has been considered purely thermal, and progressively transformed into kinetic energy during the expansion. When all the initial thermal energy has been transferred to kinetic energy of the ablated species, free-plume expansion stage is reached, therefore, the plume front dynamics becomes linear with respect to time, reaching a maximum, asymptotic expansion velocity, which is typically in order of 10^6 cm/s [53]. These models describes pretty well the angular distribution of the ablated material, which can be fitted to a $\cos^n(\theta)$ [51], where n takes into account the anisotropy of the plasma distribution and can be calculated by:

$$n = \frac{2ln2}{ln(1+\chi^2)} - 1 \qquad (2.1)$$

where χ is the ratio between the minor and the major axis of the elliptic plume.
Usually, as the ablation yield of a ns PLD is higher than 0.1 monolayer per ns.

2.1.2 Film growth

The first species of the plume, which arrive on the substrate surface after the first laser pulse, nucleate in subcritical clusters. These clusters dissociate in mobile species, which can nucleate in new clusters of different size. After the following pulse, the same process recurs and the only difference is that some of the incoming mobile species can join the clusters nucleated in the previous clusters. This process will repeat for each laser pulse.

During the film growth, several parameters affects his structure and morphology. Usually, a film deposited by PLD is characterized by particulates embedded in the film; however by the tuning of substrate-target distance, substrate temperature, laser fluence and ambient pressure in the ablation chamber, it is possible to control the particles size, or even avoid their presence on the film surface if a flat surface is required. Since film coating hard tissue implants require rough surface, nano- and micron-size particles benefits the performances of the implant.

There are three main mechanism of particulate production, strongly dependent on the target material and its near-surface morphology: condensation from vapour phase, target fragmentation and droplet ejection. Particles originated by different mechanisms can coexist in the same film [54].

Ultrafine particles are originated by vapour phase (or gas-phase) condensation. Their dimension can be controlled by the gas ambient pressure. In a typical PLD experiment the target-substrate distance is of few cm, therefore, in presence of an ambient gas, the vapour species in the plasma can collide several times with the gas molecules. Before their arriving on the substrate the collisions can cause the nucleation and growth of the vapour plasma components in different size particles. Therefore particles dimension grows with the ambient gas pressure. On the contrary, depositing in high vacuum condition, smaller particles are obtained and their distribution size is narrower [54].

Target fragmentation is more probable during the ablation of rough target surface, in which the exposure of cracks and poorly attached particles to an intense laser beam causes the formation of crater edges, columnar structures and deep voids. Any mechanical weakness can be easily dislodged. If these fragments are melted in the plasma, mainly for the interaction with the laser pulse, they will deposit as circularly shaped particles, otherwise, they will arrive on the growing film as irregularly shaped fragments [54]. Clearly, the presence of the latters is usually detrimental, since their adhesion on the substrate is poor and their shape is not controllable.

The ejection of liquid droplets occurs when the molten layer of the target is superheated, the metastable superheated liquid cannot sustain the tensile forces, vapour bubbles are created and grow in order to extract heat, and the explosive boiling (or phase explosion) of molten material from the target takes place [54].

2.1.3 Parameters

The characteristics of the deposited films can be tuned, according to the needs, by the changing of the deposition parameters: energy per laser pulse, pulses frequency, target-substrate distance, substrate temperature.

The energy of the laser pulse, or rather the fluence, which is the amount of laser energy delivered in a single pulse per unit area, has to be high enough to induce the material ablation, but not so high to induce particle ejection.

Pulse frequency determine the deposition rate, however it should be taken into account that, in the lapse of time between two consecutive laser pulses, the species arriving on the substrate tend to dissociate into mobile atoms that help to stabilize some of them.

The kinetic energy of the arriving species is controlled by the target substrate distance: the higher the distance the more uniform the film, since segregation can occur within the plume.

Since the mobility of the species on the substrate is strongly dependent on the deposition temperature, this parameter has a big incidence on the film morphology and crystallinity.

Certainly the deposition time matters, since it is possible to modify film thickness and morphology.

2.2 Electrophoretic deposition

In EPD technique a colloidal suspension of particles is subject to an applied electrical field, under which the charged particles move onto the electrode with opposite charge. Consequently, if the particles are positively charged, they will deposit on the cathode, so a cathodic deposition will take place; on the contrary, if the particles are negatively charged an anodic deposition, as in Figure 2.3, will occur. When a particle is in the liquid medium, it can be charged by four mechanisms [55]:

- selective adsorption of ions from the liquid on the solid particle;
- dissociation of ions from the solid particle in the liquid;
- adsorption of dipolar molecules on the solid particle's surface;
- electron transfer between the solid particle and the surrounding liquid.

EPD is a versatile and attractive technique for the production of coating of a wide range of materials or combination of them. Its applications include the production of wear resistant coatings, ceramics coatings, functional films for microelectronics and solid fuel cells and coatings for biomedical implants [14]. This deposition method exhibits several advantages, such as:

- ✓ it can be carried out on any kind of substrate also with complex geometries;
- ✓ it is a fast coating process;
- ✓ it is possible to deposit complex compound and also their combinations.

The basic processes involved in EPD have been extensively studied. It is well known that EPD is carried out in a cell with two electrodes connected to a power supply, as shown in Figure 2.3. It is a two-step process. The first one is the electrophoresis, in which the charged particles in the suspension, driven by an external electrical field, move toward the oppositely charged electrode (working electrode)[6]. The second step is the deposition itself, when particles coagulate on the electrode, that acts as substrate, forming a film with thickness and morphology depending on the deposition conditions. Once deposited, the film is dried and then, usually, subject to other treatments, as sintering, in order to consolidate it [56]. This last step can be generally avoided for composite inorganic-organic films, were organic part is a polymer that acts also as a binder.

---

[6] The EPD experiment can be carried out at constant voltage or constant current. Since during the present work the deposition has been performed only applying a constant voltage, all the explanation given in this chapter will be referred on constant voltage case. Furthermore, the electrode can have different geometries, which modifies the kinetics equations. Only planar geometry will be considered in the following discussions.

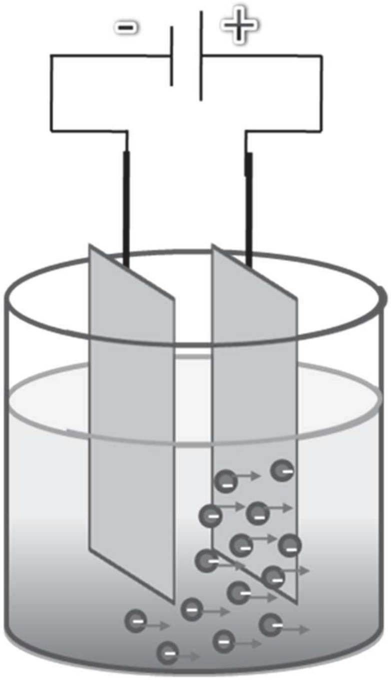

Figure 2.3: EPD set-up.

2.2.1 Kinetics

One of the first study on the kinetics of EPD was conducted by Hamaker, who observed that the deposition yield of EPD varies linearly with the charge passed, therefore, in 1940 he published his first kinetic model [57], in which the deposit yield (Y, kg) is proportional to the electrophoretic mobility (μ, $m^2/(V \cdot s)$), the electric field strength (E, V/m), the surface area (A, m^2) of the electrode and the particle concentration in suspension (C_S, kg/m^3), integrated over deposition time (t, s):

$$Y = \int_{t_1}^{t_2} \mu E A C_S dt \tag{2.2}$$

The equation is usually integrated implicitly, assuming μ, E, A and C_S constant during the deposition time. Furthermore, the efficiency factor ($f \leq 1$) is often included, in order to consider the possibility that not all the particles brought to the electrode are incorporated into the deposit; however $f \approx 1$ for colloidal stable suspension [58]. Thus the equation become:

$$Y = f \mu E A C_S t \tag{2.3}$$

However, the equation does not take into account the decreasing of the C_S during the EPD process. Later Biesheuvel and Verweij [59] conducted a more accurate study. They considered EPD as an undisturbed sedimentation process, describing only the transprt phenomena close to the interface suspension-deposit and neglecting all the possible movements in the suspension and at the counterelectrode.

The concentration of particles in the suspension (*s*), C_s, and the concentration in the deposit (*d*), C_d, are:

$$C_s = \phi_s \rho_p \qquad C_d = \phi_d \rho_p \tag{2.4}$$

where ϕ is the volumetric concentration and ρ the intrinsic particles density. Thus the deposition rate is related to the particles velocity and their volumetric concentration by the equation:

$$\frac{\mathrm{d}\delta}{\mathrm{d}t} = -v_c \frac{\phi_s}{\phi_d - \phi_s} \tag{2.5}$$

where δ is the deposit thickness and v_c is the particles velocity at the suspension-deposit boundary. Considering that the velocity of particles in an electrical field is the product of their mobility and the field strength, it is possible to solve equation 2.5 for $\delta = 0$ at initial condition:

$$\delta = \mu E \frac{\phi_s}{\phi_d - \phi_s} t \tag{2.6}$$

If the deposition yield is written as a function of the film thickness, it becomes:

$$Y = \delta A \phi_d \rho_p \tag{2.7}$$

By the substitution of equations 2.4 and 2.6 into 2.7 the result is:

$$Y = \mu E A C_d \frac{\phi_s}{\phi_d - \phi_s} t \tag{2.8}$$

If $\phi_s << \phi_d$, so if the suspension is sufficiently diluted, ϕ_s is neglected in the denominator in equation 2.8; thus, it is possible to obtain the Hamaker' law equation 2.3.

In all the other cases, generally observed, the correction factor for the concentration (X) is obtainable by the division of equation 2.8 by 2.3:

$$X = \frac{\phi_d}{\phi_d - \phi_s} \tag{2.9}$$

X is normally >1; as ϕ_s approaches zero X approaches 1.

Another important factor that can affect the deposition yield is the particles charge, because of its influence on particles mobility. In fact, charged particles in suspension repel ions with same charge (co-ions) and are surrounded by ions with opposite charge (counter-ions), forming a lyosphere [58]. When an electrical field is applied, ions with opposite charges should move in opposite direction, however the attractive force ions/counter-ions keeps them together in the so called Stern layer. Externally to the Stern layer a second diffuse layer of co-ions and counter-ions takes place, in which the concentration of ions decreases gradually with the distance until the reaching of the equilibrium condition. The resulting particle mobility is related to the dielectric constant, the viscosity of the suspending liquid and the electrical potential at the boundary between the moving particle and the liquid, called the slipping plane. As shown in Figure 2.4, the electrical potential at the slipping plane corresponds to the zeta potential (ζ) [55]. Therefore, particles mobility is related to ζ–potential by the following Henry law [59]:

$$\mu = \frac{2\varepsilon\zeta f_1(ka)}{3\eta} \tag{2.10}$$

where ε is the dielectric constant, η is the viscosity $f_1(ka)$ is the Henry's function, that is function of the double layer thickness (1/k) and the particles core radius (a).

ζ–potential is an indicator of the charge distribution in the suspension, hence the particles velocity does not depend directly on their charge, but on the net charge enclose the lyosphere [55]. Accordingly, the ζ–potential is an indicator of the suspension stability: the higher ζ–potential, the thicker the double layer, more stable is the suspension, because the colloids with high ζ–potential, in absolute value, are electrically stabilized while colloids with low ζ–potential tend to coagulate or flocculate.

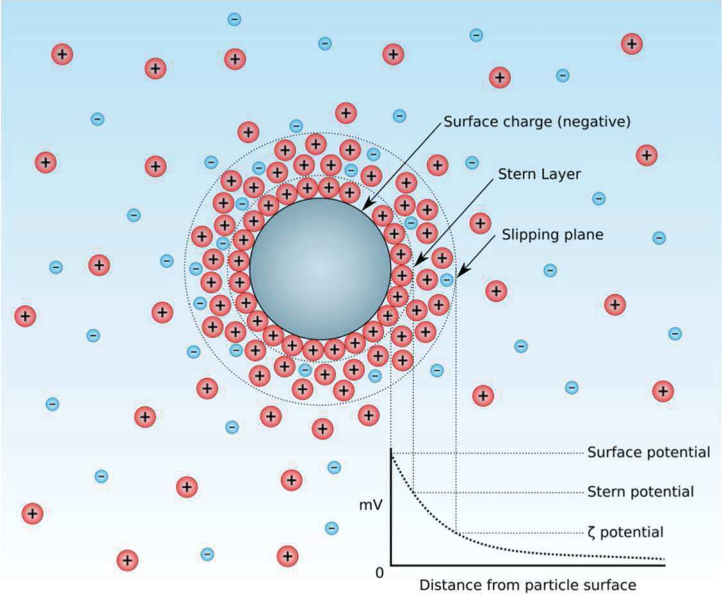

Figure 2.4: Zeta-potential representation.

2.2.2 Deposition mechanism

A number of theories have been put forward to try to clarify the electrophoretic deposition mechanism. However, up to now it is still not completely elucidate and under investigation. Again the first attempt was made by Hamaker and Verwey [60], who suggest deposition was based on the accumulation of particles on the electrode surface. They considered the EPD similar to natural sedimentation, therefore, particles accumulated on the electrode and deposit on its surface thanks to the pressure exerted by the incoming particles. This proposed mechanism works only for very stable suspension (high ζ value). Later Koelmans and Overbeek [61] proposed a deposition mechanism based on the DLVO theory.

DLVO theory (from Derjiaguin, Landau, Verwey, OverbeeK) is used to explain the stability of colloidal particles suspension by the combination of van der Waals attraction curve (Figure 2.5 (C)) and the electrostatic repulsion curve (Figure 2.5 (A)). The resulting curve (Figure 2.5 (B)) has a maximum corresponding to the energy barrier that particles have to overcome to agglomerate. Therefore, particle deposition occurs if the system is able to overcome this energy barrier. They considered that near the surface of the working electrode the electrolyte concentration increases, thus the ζ–potential decreases and the suspension is more instable inducing the flocculation of particles and their collapse in the deposit. Moreover, a finite time is required for the increasing of the electrolyte concentration near to the electrode surface and the subsequent beginning of the deposition.

This time is termed critical time and its magnitude decreases with the increasing of the applied voltage; which is the reason why sometimes the critical time is too short to be observed.

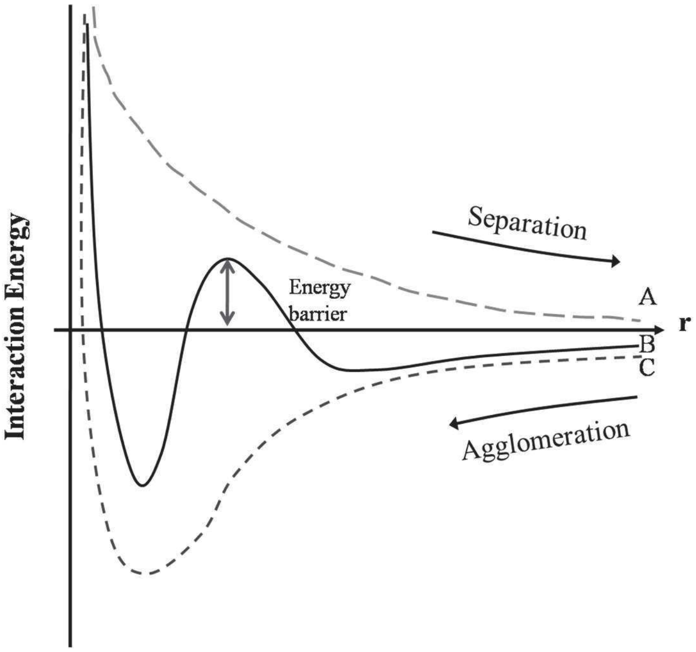

Figure 2.5: Energies involved during the electrophoretic deposition:(A) electrostatic repulsion, (C) van der Waals attraction curve, (B) resulting curve.

Another explanation of the deposition mechanism was given by Sarkar and Nicholson [58] based on the distortion of the diffuse double layer under the effect of the electric field (represented in Figure 2.6). When an electrical field is applied, the particle starts its motion inside the lyosphere towards the deposition electrode. The spherical lyosphere becomes oval and the particle moves from the centre of the lyosphere to the electrode. This causes the reduction of the double layer thickness and induce the reduction of the electrostatic forces between the arriving particle and the already deposited ones. Consequently, the increasing effect of the forces causes the coagulation of the particles and the formation of the deposit.

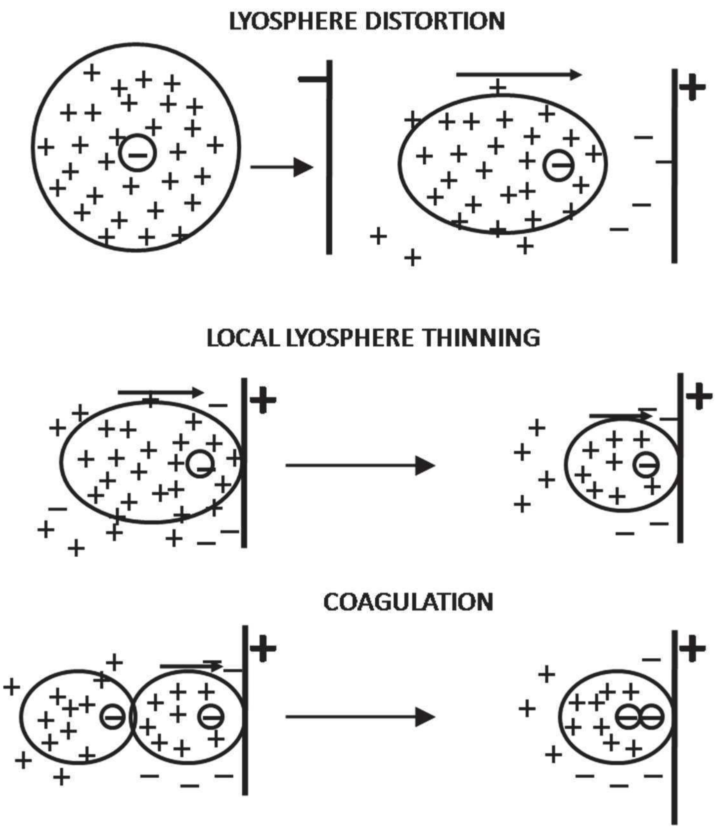

Figure 2.6: deposition mechanism was given by Sarkar and Nicholson [58].

2.2.3 Parameters

a *Suspension preparation*

The preparation of a stable suspension is the key to have a successful electrophoretic deposition. A proper suspension can be prepared by the control of some parameter, such as the particles dimension, the dielectric constant and the ionic conductivity.

The first important parameter is the particles size. In fact, large particle can easier settle than small one because of the gravity influence. These phenomenon causes a change in the concentration in function of the deepness, thus films deposited are, usually, thicker in the bottom and thinner in the top. Such type of coating is more susceptible to cracks during drying and sintering process due to stress accumulation.

As regards the dielectric constant, liquid with low ε are not able to deagglomerate particles, hence sedimentation and coagulation occur. On the other hand, if ε is too high, the ions concentration increases and the stability decreases [55]. The ions concentration controls the suspension conductivity: if it is too high, particles mobility is very low.

When the suspension is prepared in water, the particles charge, mainly for oxides, is determine by the absorption or desorption of protons. In this case ions concentration can be controlled by the adjusting of the pH. However, the use of water causes some problems. In fact, electrolysis of water occurs at low voltage (5 V), consequently, gas evolution at the electrode causes the inclusion of gas bubbles in the deposit. On the other hand, although organic solvent can be used at high field strength, they have typically lower ε.

In summary, in order to prepare a proper suspension it is important to keep a high zeta potential, high dielectric constant and low ionic conductivity.

b *Deposition parameters*

Once a stable suspension is obtained, deposition parameters to monitor are the time, the applied potential and the substrate (working electrode) conductivity. The linear correlation between the deposition time and the deposited mass is valid only for short deposition time. In fact, once film becomes thick, it acts as an insulator layer reducing the deposition rate. Ideally, applying high deposition potential the deposited mass increases. However at high potential the depositing particle have not enough time to rearrange in the film. Thus the obtained coating is not homogeneous and with more structural defects. Finally highly conductive substrate allows to obtain homogeneous coating.

CHAPTER 3

Materials and methods

In this chapter the experimental set-up, the materials and the methods used for the coatings deposition will be illustrated. First of all the experimental set-up of the two employed deposition technique (PLD and EPD) will be described. Then all the starting material preparation, deposition parameters and characterization technique for each deposition experiment will be illustrated.

3.1 Pulsed Laser Deposition set-up

3.1.1 Laser source

The ablation source has been a Nd:YAG laser. This is a solid state laser with a gain medium constituted by a neodymium-doped yttrium aluminium garnet crystal ($Nd:Y_3Al_5O_{12}$), optically pumped using flash lamps.

The fundamental wavelength is at 1064 nm and is due to the transition of the 3 electron of the level 4f of Nd^{3+} in the YAG crystal field. The energy-level diagram of the involved states is reported in Figure 3.1. The levels are labelled with their spectroscopic notations. Since the Nd atoms are situated within the YAG host crystal, the otherwise degenerated energy levels of the isolated Nd atom split into a number of states. The Nd:YAG absorbs mostly in the bands between 730–760 nm and 790–820, coupled to the level $^4F_{3/2}$ by a rapid non-radiative decay (~10^{-7} s). The main laser transition $^4F_{3/2} \rightarrow {}^4I_{11/2}$ involves specifically two sublevels ($R_2 \rightarrow Y_3$). From here the Nd atoms relax again into the ground state $^4I_{9/2}$ until the pumping process starts from the beginning again.

The Q-switching mode allows to obtain high energy short (ns) pulses, through modulation of intra-cavity losses, which requires a modulating device, triggered by an external source (outside the cavity). Furthermore, thanks to the presence of KDP (KH_2PO_4) crystals, the generation of a second harmonic is possible, thus a green (532) nm laser light can be used, as in the present work.

For all the PLD experiments a Handy YAG Quanta System Q-switched Nd:YAG laser source, with λ = 532 nm, τ = 10 ns and repetition rate = 10 Hz, has been used. The depositions have been conducted at 37 or 12 J cm^{-2} of fluence.

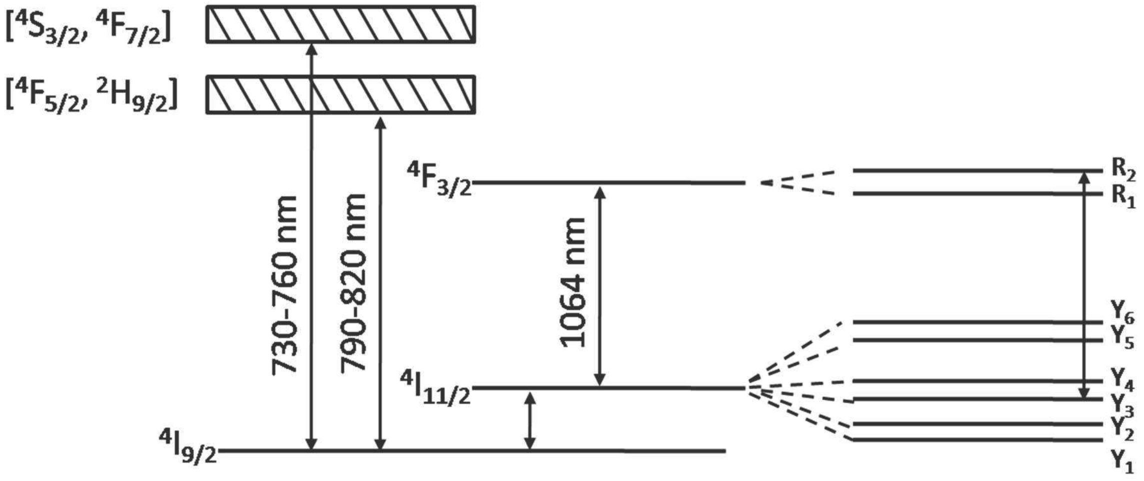

Figure 3.1: Energy-level diagram of Nd:YAG laser.

The Q-switching mode allows to obtain high energy short (ns) pulses, through modulation of intra-cavity losses, which requires a modulating device, triggered by an external source (outside the cavity). Furthermore, thanks to the presence of KDP (KH_2PO_4) crystals, the generation of a second harmonic is possible, thus a green (532) nm laser light can be used, as in the present work.

For all the PLD experiments a Handy YAG Quanta System Q-switched Nd:YAG laser source, with λ = 532 nm, τ = 10 ns and repetition rate = 10 Hz, has been used. The depositions have been conducted at 37 or 12 J cm^{-2} of fluence.

3.1.2 Deposition set-up

The film depositions have been carried out on the various target materials into a stainless steel vacuum chamber, evacuated by the means of a scroll and a turbo-molecular pumps until a pressure of 4×10^{-3} Pa. The chamber is equipped with quartz window for the inlet of the laser radiation. The target is supported onto a rotating holder in order to minimise the laser induced craterisation effect. The substrate is positioned in front of the target with a distance of 2 cm, and is eventually resistively heated. By the means of mirrors and lens, the laser beam is focused onto the target surface with an incident angle of 45°.

3.2 Electrophoretic Deposition set-up

EPD has a very simple setup (Figure 3.2), consisting of a power supply (TTI EX752M Miltu-Mode PSU 75V/150V 300W) with an amperometer (TTI 1906), both from Telemeter Electronic GmbH, Germany, connected to the electrodes by copper cables. The experiments have been carried out at constant voltage, adjusted with an accuracy of 0.1 V, and the deposition time has been recorded with a timer. The electrodes have been two commercial stainless steel AISI 316L (Thyssenkrupp, Germany) foils (0.2 mm in thickness, 15 mm in width and 30 mm in length). The electrodes, attached to a support throughout two clamps, connected to a distance regulator, has been dipped for 15 mm in the EPD suspension. This latter has been prepared in a glass beaker and positioned on a manual elevator platform.

The EPD parameters have been optimized by the variation of the deposition time and voltage until a homogeneous, compact and crack-free coating has been obtained.

Figure 3.2: EPD set-up.

3.3 PLD of hydroxyapatite-based materials

3.3.1 IONPs preparation: Laser Alation in Liquid

For the laser ablation in liquid process, a Spectra Physics SpitfirePro Ti:Sa ultra-short pulse laser source (λ: 800 nm, τ: 120 fs; repetition rate: 1 kHz, E: 3 mJ) has been used. A 50 mm focal plano-convex lens has allowed to focus the laser beam perpendicularly to the surface of the Fe target (Aldrich, purity 99.9%, 0.5 mm thickness). The target has been covered by a 2 cm bidistilled milli-Q water column, contained in a 1.5 cm × 5 cm quartz cuvette. The ablation process has been replicated several times, in order to obtain a proper amount of nanoparticles (NPs). Aliquots of the obtained colloidal solution have been transferred in centrifuge tubes; the NPs have been separated by centrifugation (6000 rpm, 90 min), collected and dried under ambient conditions.

3.3.2 Pulsed laser deposition of composite HAp/IONPs films

The target for the pulsed laser deposition has been prepared mixing in an agate mortar the NPs prepared by LAL (4wt%) with Hydroxyapatite powder (reagent grade, Sigma-Aldrich). The mixture has been pressed in a hydrostatic press in order to obtain a pellet. The experimental set-up described in section 3.1 has been used. Films have been deposited on a monocrystalline silicon (Si (100) Goodfellow) substrate for a deposition time of 4 h at three different substrate temperatures (room temperature (RT), 300 °C and 500 °C), with a substrate-target distance of 2 cm, at a fluence of 37 mJ.

3.3.3 Characterization techniques

a *High resolution transmission electron microscopy (HRTEM)*

HRTEM Fei-TECNAI G2 20 TWIN, operating at 200 kV, has been used to study both the particle-size distribution and the crystalline phases.

The sample of NPs produced by LAL has been obtained by drop casting NPs colloidal solution on a holey carbon coated copper grids. TEM analysis of the deposited films has been performed by using Formvar/Carbon copper grids. In this case the film has been deposited at room temperature with a reduced deposition time, i.e. 7 min.

b *Angular Dispersive X-ray diffraction ADXRD*

The crystalline phases have been investigated by ADXRD analysis throughout a X-Perth-Pro Philips X-ray diffractometer operating at 40 kV and 32 mA, using CuKα radiation (wavelength of 1.5406 Å) in a θ–2θ configuration.

The explored range has been from 15 $2\theta°$ to 80 $2\theta°$ at a speed of 0.08 $2\theta°$/min and a step of 0.04°.

c *Micro-Raman spectroscopy*

Micro-Raman measurements have been performed by using a Jobin-Yvon Horiba LabRam apparatus equipped with edge filter, which excludes Raman shift below 150 cm^{-1} from detection, a He–Ne laser (λ: 632.8 nm) and an Olympus microscope with 10×/50×/100× objectives. A spectral resolution of about 4 cm^{-1} has been obtained by a holographic grating with 600 lines/mm. Measurement times have been integrated in the range of 50–150 s and neutral density filters have used in order to avoid sample degradation.

d *Fourier trasformed infra-red spectroscopy (FT-IR)*

FT-IR analysis has been performed by using a Jasco FT-IR 460 Plus interferometer. The spectra have been acquired in absorbance mode by collecting 100 scans at 4 cm^{-1} resolution, in the range of 4000–400 cm^{-1}.

A dried KBr thin pellet has been used as blank. The target sample has been prepared by the mixing and the pressing of KBr and starting powders (only IONPs, only HAp and both together as in the target). A non-coated Si substrate has been used as blank for the films analysis.

e *Scanning electron microscopy (SEM) and energy dispersive X-Ray spectroscopy (EDX)*

The morphology of the deposited film have been studied by means of a SEM device (Philips-FEI ESEM XL30), coupled with a X-EDS EDAX system for microanalysis. The electron emitter is a LaB_6 crystal and the emission power value can reach 30 keV. The image has been acquired in the secondary electron modes, with a resolution of 4 nm. The samples were coated with a gold layer before the observation to avoid sample charging during the imaging.

f *Atomic force mycroscopy (AFM)*

The AFM apparatus (Park System XE 120), coupled with an optical microscope (Nikon TE 2000), has been used in non-contact mode to collect several 10 × 10 μm^2 and 5 × 5 μm^2 images in order to have quantitative information on surface roughness, in terms of root-mean-square (r.m.s.).

g *Magnetic measurements*

The magnetic characterization of samples has been performed by field dependent magnetization measurements in the 5 K-300 K temperature range using a Quantum Design SQUID magnetometer (Hmax= 50 kOe).

h *ICCD fast imaging*

Fast ICCD imagines of the plasma have been acquired by the means of a iStar camera (Andor technology, Oxford instruments), equipped with a photographical objective Nikkor, positioned normally to the plasma expansion direction (see Figure 3.3). Andor software has allowed the setting of the parameters for the images registration: delay and gate has been varied from 50 to 1000 ns.

Figure 3.3: Set-up for the ICCD fast images detection of the plasma.

i *Optical emission spectroscopy*

Optical emission spectroscopy (OES) has been carried out by focusing the plasma plume onto a fused silica optical fiber bundle. The optical fiber was linked to a 500 mm focal length spectrograph (ARC 500i) connected to a fast ICCD device (PI MaxII, 1024×1024 pixels). The width of the entrance spectrograph slit has been 80 μm and the grating employed was 1200 grooves/mm. The gated system had a time resolution of 2 ns and each acquisition was integrated on 50 laser shots in order to increase the signal to noise ratio. Varying the position of the optical elements by a micrometric translation stage, it has been possible to obtain space resolved emission spectra at different distances from the ablated target surface with a spatial resolution of 20 μm.

3.4 PLD BG_Cu

3.4.1 BG_Cu preparation by melt processing

45S5 bioactive glass (BG) doped with 5 wt.% CuO has been furnished by the Institute of Biomaterials, University of Erlangen-Nueremberg, headed by Prof. Dr.-Ing. habil Aldo R. Boccaccini. The bioglass has been produced by melt processing. SiO_2, Na_2CO_3, $CaCO_3$, (Merck,Germany), $Ca_3(PO_4)_2$ and $CuCO_3{\cdot}Cu(OH)_2$ (Sigma–Aldrich, Germany) powders have been homogenized and melted at 1450 °C for 45 min [62]. The glass was then fritted and milled. The so obtained powder has been pressed in order to obtain a pellet, and sintered in air under the following conditions: peak temperature 1100 °C, heating rate 5 °C/min and cooling rate 20 °C/min.

3.4.2 BG_ Cu laser induced plasma ICCD image detection

The experimental set-up for this characterization is reported in section 3.3.1 a. Also in this case the delay time and the gate width have been varied from 50 to 1000 ns. The experiments have been carried out in absence and in presence of the substrate in front of the target.

3.4.3 BG_ Cu films deposition and characterization

The BG_Cu pellet has been used as target for the deposition of the thin films applying a PLD technique. PLD experimental setup is described in section 3.1. Depositions conditions have been: 12 J/cm^2 of laser fluence; substrate positioned at 2 cm from the target; deposition time of 4 h, the substrate temperature has been varied: room temperature (RT), 300 °C and 500 °C. Ti substrates (Ti foil, 99.6%, GoodFellow) squares of 1 × 1 cm^2 geometry have been sandblasted with a 60-grid SiC abrasive powder in order to assure nanometric surface roughness and boiled in aqua regia for 30 min, in order to remove any contaminant from the surface.

a *Angular Dispersive X-ray diffraction ADXRD*

The crystalline phases have been studied by ADXRD, with the X-Perth-Pro Philips apparatus reported in section 3.3.3 b. The spectra have been acquired at 2θ 10°–70°, step size 0.040°, time per step 4 s.

b *Fourier trasformed infra-red spectroscopy (FT-IR)*

FT-IR techniques, described in sections 3.3.3 d, has been employed for the spectroscopic characterization. In this case, the substrate has been monocrystalline silicon (Si (100) Goodfellow) wafer.

c *Contact angle measurements*

The wettability of the BG_Cu coated surface has been evaluated by means of static water contact angles measurements (DSA30 Kruess GmbH, Germany). Deionized water droplets with the volume of 3 μL have been released on the surface of the sample with a dropping rate of 100 μl/min. An image of the status of water droplet on the sample surface was taken and the contact angle at the interface was calculated immediately. For each coating samples at least 3 droplets have been measured.

The contact angle is given by the angle between the calculated drop shape function and the sample surface, as shown in Figure 3.4.

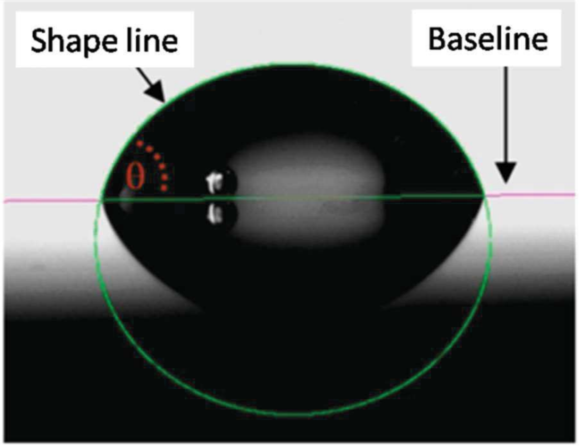

Figure 3.4: Static droplet with fitted contour.

d *In vitro evaluation of bioactivity: SBF assessment*

For the assessment of bioactivity in vitro, the standard protocol introduced by Kokubo et al has been followed [63], the amount of the reagents has been adjusted according to their purity. At this purpose coated and uncoated substrates have been placed in a plastic tube and submerged in simulated body fluid. The proper volume of SBF has been calculated with the formula $V_{SBF} \cdot 1/4S_a = 10$. The tube have been kept at 37 °C for different soaking time. SBF has been changed twice a week. Once the pre-specified time point has been reached, the sample has been removed from SBF, washed with bidistilled water and dried in ambient conditions. ADXRD , micro-Raman spectroscopy and SEM-EDX analysis (set-up in sections 3.3.3 b, c and e, respectively) have been carried out to evaluate the formation of hydroxyapatite on the coatings.

For the preparation of 1 liter SBF, bidistilled milli-Q water has been used to dissolve the chemicals (supplied by Carlo Erba) listed in Table 3.1.

Table 3.1: List of chemicals used for the SBF preparation.

Chemicals	Purity %	Amount (g) for 1L
1- Sodium chloride (NaCl)	100.0	7.9550
2- Sodium hydrogen carbonate ($NaHCO_3$)	100.0	0.3532
3- Potassium chloride (KCl)	100.0	0.2228
4- Dipotassium hydrogen phosphate trihydrate ($K_2HPO_4 \cdot 3H_2O$)	100.0	0.2287
5- Magnesium chloride hexahydrate ($MgCl_2 \cdot 6\ H_2O$)	99.0	0.2988
6- Hydrochloric acid (HCl) 1 M		39 ml
7- Calcium chloride dehydrate ($CaCl_2 \cdot 2\ H_2O$)	100.0	0.2760
8- Sodium sulfate (Na_2SO_4)	100.0	0.0713
9- Tris(hydroxymethyl)aminomethane (TRIS)	99.5	6.0873
10- Hydrochloric acid (HCl) 1 M		0-5 ml

A graduate plastic beaker has been filled with 700 ml of bidistilled water, kept at 36.5±1.5 °C in a thermal bath. The chemicals have been added, from 1 to 8 in the order reported in Table, one by one until the complete dissolution, under continuous stirring. Bidistilled water has been added up to 900 ml and the electrode of the pH-meter has been put in the solution (pH is 2.0±1.0). TRIS has been added controlling the pH value. When the pH has risen to 7.45±0.1, small amounts of HCl 1M has been added to lower the pH at 7.42±0.1. This operation has been conducted until the compete dissolution of TRIS. At the end pH has been adjusted to 7.40 exactly at 36.5 °C. Water has been added to obtain 1 liter.

The SBF has been restored in a plastic bottle at a temperature of 5-10 °C for a maximum of 30 days.

3.5 EPD of compostite zein/BG and /Cu-doped BG coatings

This work has been mostly carried out at the Institute of Biomaterials, Department of Materials Science and Engineering, University of Erlangen-Nuremberg, under the supervision of Prof. Dr.-Ing. habil. Aldo R. Boccaccini.

3.5.1 Zein, BG and Cu-doped BG materials and characterization

Zein from corn maize in powder form (Sigma-Aldrich Germany), BG (SCHOTT Vitryxx® Bioactive Glass, d= 2 μm), an Bg-2.5Cu (produced by melt processing synthesis as in the REF [62]) have been characterized, in order to control their phase purity by micro-Raman (see section 3.3.3 c) and FT-IR analysis.

a *Fourier trasformed infra-red spectroscopy (FT-IR)*

FT-IR analysis has been performed by using a IRAffinity-1S Shimadzu instrument, equipped with a Quest ATR FTIR accessory (Specac) (Figure 3.5), which allows to acquire spectra from powders without the necessity to prepare a pellet with KBr, as usual. The spectra have been acquired in absorbance mode by collecting 60 scans at 4 cm^{-1} resolution, in the range of 4000–400 cm^{-1}.

Figure 3.5: FT-IR instrument equipped with the ATR FTIR accessory.

3.5.2 Suspension preparation

For the suspension preparation, glycerol (Sigma-Aldrich Germany) has been added in a mixture of deionized water and absolute ethanol (Merck Millipore Germany) (H_2O:EtOH, 1:2) and stirred for 1 minute. Then BG or BG-2.5Cu powders have been added gradually under continuously stirring. The suspension has been magnetically stirred for 5min followed by 10 min ultrasonication (using an ultrasonic bath, Bandelin Sonorex, Germany). Zein powder has been then slowly added and the stirring and ultrasonication steps have been repeated. The ultimate concentrations of BG or BG-2.5 Cu have been 0 g/l, 20 g/l or 50 g/l. The pH has been adjusted to 8.5 by small adding of acetic acid.

3.5.3 Films deposition by EPD

The EPD setup has been described in the section 3.2. AISI 316L stainless steel (SS) foils have been used as substrates with a length of 30 mm and width of 15 mm. The substrates have been cut, cleaned in acetone, for 10 min each in an ultrasonic bath and dried. For the construction of the EPD cell, two parallel SS substrates have been positioned with a relative distance of 10 mm. The electrodes have been dipped for 15 mm into the suspension, yielding a deposition area of 3 mm^2. Two electrodes holder were connected to a voltage-constant power source. The optimization of the deposition has been carried out in different voltage values and different deposition time.

3.5.4 Films characterization

a *SEM-EDX*

The surface morphology as well as the composition of the deposited coatings have been studied by SEM (Auriga Zeiss) equipped with an EDX detector. The samples were coated with a gold layer of around 15 nm (model Q150T, QUORUM) before the observation to avoid sample charging during the images detection.

b *Bending test for qualitative adhesion evaluation*

In order to have an idea of the coating adhesion to the substrate, a cycled bending test has been performed. The coated substrate has been bent until the coated surface became parallel to the other half of the substrate, then it has been bent back to its original position, this two steps have been repeated for 5 times. before the next bending cycle. Optical images have been acquired in the region where the tensile strength is at a maximum level [64].

c *Contact angle measurements*

The wettability of the coated electrodes has been evaluated by the means of static contact angle measurements, performed in the same condition of that described in the section 3.4.3 c.

d *In vitro evaluation of bioactivity: SBF assessment*

For the assessment of bioactivity in vitro, the standard protocol introduced by Kokubo et al has been followed [63], as described in section 3.4.3 d. SEM-EDX, ADXRD , FT-IR and micro-Raman analysis and (set-up in sections 3.5.3 a, 3.3.3 b, 3.5.1 a and 3.3.3 c, respectively) have been carried out to evaluate the formation of hydroxyapatite on the coatings.

For the preparation of SBF, the chemicals have been supplied by Sigma-Aldrich.

3.6 RKKP coated Ti as support for Mesenchymal Stem Cells delivery

3.6.1 RKKP preparation by sol-gel synthesis

RKKP powder has been furnished by ISM-CNR, Montelibretti unit, Monterolo (RM). It has been prepared by sol-gel route. The synthesis has been performed as described in previous works [65,66]. RKKP glass–ceramic composition (SiO_2 – 43.68, P_2O_5 – 11.10, CaO – 31.30, Na_2O – 4.53, MgO – 2.78, CaF_2 – 4.92, K_2O – 0.19, La_2O_3 – 0.50, Ta_2O_5 – 1.00, all in wt%) has been synthesised by the hydrolysis and polycondensation of an aqueous solution of tetraethyl orthosilicate (TEOS, $Si(OC_4H_9)_4$, 99.99%, Sigma–Aldrich), triethyl phosphite ($P(C_2H_5O)_3$, 99.5%, Sigma–Aldrich), calcium nitrate tetrahydrate ($Ca(NO_3)_2{\cdot}4H_2O$, 99.60%, Sigma–Aldrich), sodium nitrate ($NaNO_3$, 100.40% Sigma–Aldrich), magnesium nitrate hexahydrate ($Mg(NO_3)_2{\cdot}6H2O$, 101.5%, Carlo Erba), ammonium fluoride (NH_4F, 99.99%, Sigma–Aldrich), potassium nitrate (KNO_3, 99.9%, Sigma–Aldrich), lanthanum nitrate hexahydrate ($La(NO_3)_3{\cdot}6H2O$, 99.9%, Sigma– Aldrich) and tantalum ethoxide ($Ta(OC_2H_5)_5$, 99.98%, Sigma– Aldrich), in stoichiometric amounts. HNO_3 (0.1 M) was used to catalyse the TEOS and the triethyl phosphite hydrolysis The synthesis has been carried out in a Teflon bottles. Each reactant was consecutively added every 30 min, under the continuous stirring, in the order in which they are listed above. The obtained sol has been kept at room temperature for 10 days, then aged at 70 °C for 72 hours. The obtained gel has been dried at 120 °C for 48 hours, in order to remove the gaseous by-products, and stabilised at 700 °C . After the pre-treatment at 700 °C (heating rate 5 °C/min, the powder has pressed at 400 MPa, in order to obtain a pellet, and sintered in air under the following conditions: peak temperature 1100 °C, heating rate 5 °C/min and cooling rate 20 °C/min. The obtained target has been analysed by X-Ray diffraction using a Philips PW1130 diffractometer with Ni-filtered CuKa radiation (λ= 1.5418 Å).

3.6.2 Films deposition and characterization

The RKKP tablet has been used as target for the deposition of the thin films applying a PLD technique. PLD experimental setup is described in section 3.1. Depositions conditions have been: 12 J/cm^2 of laser fluence; substrate positioned at 2 cm from the target; deposition time of 2 h, substrate temperature of 500 °C. Ti substrates (Ti foil, 99.6%, GoodFellow) squares of 1 × 1 cm^2 geometry have been sandblasted with a 60-grid SiC abrasive powder in order to assure nanometric surface roughness and boiled in aqua regia for 30 min, in order to remove any contaminant from the surface.

a *Energy Dispersive X-Ray Diffraction (EDXRD)*

For the film's crystallinity analysis Energy Dispersive X-Ray Diffractometer (EDXRD) has been carried out. A non-commercial ED apparatus has been used, with two arms pivoting around the optical centre. sample holder. White X-ray radiation is produced by a commercial W-anode X-ray tube (12–55 keV) and is collimated upstream and downhill the sample by four W- slits. X-ray diffraction pattern represents in this case the intensity of the X-ray radiation elastically scattered by a sample as a function of the momentum transfer. The momentum transfer amplitude is the scattering parameter: $q(E,\theta) = aE \sin\theta$, where E is the electromagnetic radiation energy, 2θ, the scattering angle, and a is a constant (1.014 Å/keV).

The transmission geometry has been chosen to perform the measurements upon the target to maximize the scattering volume and to obtain a truly averaged information. The coatings have been investigated in reflection mode in order to minimize the contribution of the substrate.

b *Atomic Force Microscope (AFM)*

Atomic Force Microscope, working in the noncontact modality, has been applied to investigate the surface topography. The used instrument is described in section 3.3.3 f.

c *Scanning electron microscopy (SEM) and energy dispersive X-Ray spectroscopy (EDX)*

Film's morphology has been investigated with a SEM apparatus (a LEO 1450 Variable Pressure), working in the secondary and backscattered electron modes, with the resolution of about 4 nm in vacuum conditions. This SEM apparatus is coupled with a EDX system for microanalysis (INCA Energy 300 detector), that allows to execute qualitative/quantitative analysis of the elements with the precision limit of about 0.2%.

3.6.3 Biological tests

All the following tests have been carried out by researchers of IFT-CNR (Rome, Italy).

a *hAMSC Isolation and Culture*

hAMSC has been isolated according to the approved protocol N°64/2012/C.B. from the Ethical Committee of the FBF S. Peter Hospital, for more details see in Ledda et al. [67] All the experiments have performed seeding the hAMSCs from passages P1 up to P4 (1 × 104 cells/cm^2) on the RKKP coated Ti, non coated Ti substrate and on a commercial plastic Petri dish (as a control sample, CTR) and grown up to 4 days. The samples has been sterilized for 1 hour using ethanol treatments and then washed three times with phosphate-buffered saline (PBS).

b *Cell Proliferation and Metabolic Activity Analysis*

The hAMSC proliferation has been evaluated by Bromodeoxyuridine incorporation assay (BrdU, Cell Proliferation Kit, Roche Diagnostics). The metabolic activity has been quantified by a colorimetric assay based on the oxidation of water-soluble tetrazolium salts (Cell Proliferation Reagent WST-1, Roche Diagnostics).

c *Cytoskeleton Analysis by Actin Fluorescence Staining*

After 4 days of incubation, the cells have been fixed in paraformaldehyde (4% in PBS) for 15 min, incubated with phalloidin tetramethylrhodamine isothiocyanate-conjugate (1:500), an antiactin toxin (Sigma), in a PBS buffer for 1 h. Afterwards the staining with Hoechst 33342 (trihydrochloride-trihydrate), for nuclei localization has been executed. Cell actin distribution has been measured using an inverted microscope (Olympus IX51, RT Slider SPOT, Diagnostic instruments, Sterling Heights, MI, USA), equipped with a 20X objective and with a cooled CCD camera (Spot RT Slider, Diagnostic Instruments)

d *Flow cytometry analysis*

Cell cycle and immunophenotypic analysis have been carried out, after 2 days of incubation, by flow cytometry, using a FACSCalibur (Becton Dickinson) cytometer and data were analysed by ModFIT LT 2.0 software for the cycle phase distribution and by Cell Quest Pro software (Becton Dickinson) for the immunophenotypic characterization. For the first analysis the DNA of the alive cells has been labelled with propidium iodide (20 ug/mL, Sigma) and RNase A (250 ug/mL, Sigma) solution for 30 min at room temperature in the dark, after fixation.

For the immunophenotypical characterization the cells were labelled with mouse monoclonal antibodies against the mesenchymal CD29-FITC (HI29a, Immunotools Friesoythe, Germany), CD73-PE (AD2, BioLegend), stem cell markers and the hematopoietic CD31-APC (MEM-05, Immunotools) cell marker. The adding of propidium iodide has allowed the dead cells exclusion.

e *Real-time quantitative reverse transcriptase polymerase chain reaction (RT-PCR) analysis*

Total RNA has been extracted from hAMSCs grown treated plastic Petri dish and RKKP film surface for 4 days. One microgram of total RNA has been used to synthesize first strand cDNA with random primers, using 100U of ImProm-II RT-PCR kit (Promega, Madison, WI, USA). The quantification of all gene transcripts (VESF, β–ACT, Ki67, IDO, HGF, TGF β1, RPL34, RUNX2, ALP OCL, GAPDH) has been carried out by real-time quantitative RT-PCR.

f *Osteogenic Commitment Study*

The osteogenic commitment has been evaluated, after 1 week of cultivation in osteogenic medium, by real-time RT-PCR to analyse the mRNA expression of differentiation markers: RUNX2, Osteocalcin (OCL), and Alkaline Phosphatase (ALP).

g *Statistics Analysis*

The statistical analysis of the data obtained was performed using Student's *t*-test, with $p < 0.05$ as the minimum level of significance.

More details of the biological tests and protocols used are better described in the paper [67] and in the relative Supplementary Materials section available at http://dx.doi.org/10.1155/2016/3657906.

3.7 RKKP films to improve corrosion resistance of Mg-Ca substrates

3.7.1 Mg-Ca alloy substrate preparation

The substrates have been prepared by researchers of the Polytechnic University of Bucharest

The Mg-Ca alloys were prepared by melting pure compact magnesium (99,96 wt.%) and pure calcium granules (99,98 wt.%). For the melting process a rocker crucible furnace has been used, of a gas atmosphere of sulfur hexafluoride (SF_6) to protect against oxidation. The magnesium has been melted at 680 °C and mixed with calcium (1.4 wt%). The melt has been held and stirred, into a permanent mold using a mild steel crucible. The melt has been casted in order to obtain an ingot, and after the solidification and cooling, it has been cut into square shaped pieces (1×1 cm^2, 3 mm thick) for the subsequent use as substrates. The surface of the substrates has been polished and cleaned using metallographic techniques for magnesium alloys, described by Antoniac et al. [68].

3.7.2 RKKP preparation by melt-processing synthesis

The RKKP material, developed at ISTEC-CNR (Faenza, Italy). In this melting synthesis procedure the powders of the component oxides (SiO_2 — 43.68, $Ca_3(PO_4)_2$ — 24.00, CaO — 18.40, CaF_2 — 4.92, Na_2O — 4.53, MgO — 2.78, K_2O — 0.19, Ta_2O_5 — 1.00, La_2O_3 — 0.50, all in wt%) have been fired up to complete melting in a Pt crucible in a laboratory kiln at 1450 °C for 60 min and poured into a graphite die. The melt has been cooled down to room temperature [69,70].

3.7.3 Films deposition and characterization

The experimental set-up of PLD has been illustrated in the section 3.1. In this case the laser fluence has been kept at 12 J/cm^2, the deposition has been carried out for 4 h at 400 °C by the means of a resistively heated support.

Micro-Raman measurements have been performed using a Horiba LabRam apparatus described in the section 3.3.3 c. Energy dispersive X-ray is described in the section 3.6.2 a. While the SEM instrument is illustrated in the section 3.6.2 c

a Atomic Force Microscope (AFM)

The AFM instrument, used for the analysis of the surface texture these samples consists of a stainless steel unit made of two separable cylindrical supports, equipped with a vibration isolation system. The lower unit contains the sample holder, mounted at the top of a piezoelectric scanner that allows 40 μm×40 μm×6μm maximum range, and a x-y-z motor controlled translator, to select the areas of the sample. The upper unit contains the cantilever holder, the mirror deflection system and a four-sector-position sensitive photodiode used as deflection detector. An electronic feedback loop is used to integrate the optical signal, maintaining a constant cantilever deflection during the acquisition. Typical instrumental lateral resolution is approximately 10 nm and around 0.1 nm in Z direction. The AFM measurements were performed in non-contact (tapping mode), with a scan rate of 2.0–4.0 s/row (400–800 points/row). Data have been treated by only a background subtraction and then analysed using the Gwiddion software.

b *Linear polarization technique for the electrochemical corrosion evaluation*

The evaluation test of corrosion resistance has been performed by the means of a Potentiostat/Galvanostat (model PARSTAT 4000, Princeton Applied Re- search, USA), and the potentiodynamic polarization curves were acquired using the VersaStudio v.2.4 software.

The corrosion resistance has been determined with the Tafel plot electrochemical technique, wich consists of linear polarization plotting curves involving the following steps: open circuit potential measurements for 1 h; potentiodynamic polarization plotting curves at ±250 mV vs. OCP (open circuit potential), with a scan rate of 1mV/s.

The cell for the determination of the corrosion resistance comprises a glass with double wall (heating jacket), a saturated calomel electrode (reference electrode, SCE), a platinum electrode (recording electrode, CE) and the Mg-Ca alloy coated or uncoated samples as working electrode (WE). The samples have been assembled in a Teflon holder, and the surface exposed to corrosion has been of 1 cm ^{2}. The tests were carried out in Simulated Body Fluid (SBF) media at the human body temperature (37±0.5 °C) using a heated reticulating bath connected to the glass with double wall.

3.8 PLD of composite carbon-RKKP material for the improving of mechanical properties of the coatings

3.8.1 Target material preparation

The material preparation procedure is reported in the section 3.7.2. The obtained RKKP has been reduced to small granules whose dimension ranged from 40 to 125 μm and mixed in an agate mortar with the C_{60} (99.98%, Therm-USA) powder (5 wt%). The mixture has been pressed in a die in order to obtain a compact pellet.

3.8.2 Films Pulsed laser deposition and characterization

For the PLD experiments, the laser source and the apparatus for the PLD is described in section 3.1. The depositions have been conducted at 12 J/cm^2 fluence, for 4 h. The Ti substrate has been kept at 2 cm distance from the target on a resistively heated support, in order to vary the substrate temperature: room temperature (RT), 300 °C and 500 °C.

a *Angular Dispersive X-ray diffraction ADXRD*

The crystalline phases have been studied by ADXRD, with the X-Perth-Pro Philips apparatus reported in section 3.3.3 b. The spectra have been acquired at 2θ 10°–70°, step size 0.040°, time per step 4 s.

b *Vibrational spectroscopy techniques*

The spectroscopic characterization has been carried out by Micro-Raman and FT-IR techniques, described in sections 3.3.3 c and d, respectively.

For the FT-IR analysis the substrate was monocrystalline silicon (Si (100) Goodfellow) wafer.

c *Microscopy techniques*

Transmission electron microscopy (TEM, Fei-TECNAI G2 20 TWIN) has been used to characterize the growth mechanism of the films. In this case, Formvar carbon film-coated copper grids has been used as substrates and the deposition time has been 7 min.

Morphological studies of the deposited films have been carried out by the scanning electron microscope (Philips-FEI ESEM XL30). To investigate the film's surface texture, an AFM (Park System XE 120), coupled with an optical microscope (Nikon TE 2000), has been used. Several 10 × 10 μm^2 images have been collected in order to have quantitative information on surface roughness, in terms of root- mean-square (rms). The two apparatus are illustrated in section 3.3.3 e and f, respectively.

d *Vickers microhardness*

The microhardness measurements were carried out by the means of a Leica VMHT apparatus (Leica GmbH, Germany), equipped with a standard Vickers pyramidal indenter (square-based diamond pyramid of 1368 face angle). The loading and unloading speed has been 5×10^{-6} ms^{-1}, and the time under the peak load has been 15 s. The indentations have been performed in 2 to 12 points with loads ranging from 0.098 to19.611 N. For film samples, the measured hardness was that of the film/substrate composite system. To separate the composite hardness of the film/substrate system (Hc) into its components, film (H_f) and substrate (H_s), a Jonsson and Hogmark ''law-of-mixtures'' model has been applied [71]. In this case, the composite hardness Hc of the film–substrate system is expressed as:

$$H_c = \frac{A_f}{A} H_f + \frac{A_s}{A} H_s \tag{3.1}$$

where H is hardness; $A = A_f + A_s$ is the total contact area, as shown in Figure 3.6.

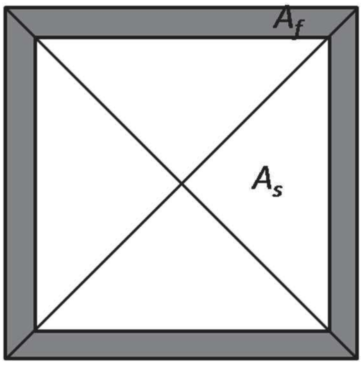

Figure 3.6: Load-supporting areas A_f and A_s, of the film and the substrate, respectively.

From the geometric considerations Eq. (1) can be specified as follows:

$$H_f = H_s + \frac{H_c - H_s}{2c(t/d) - c^2(t/d)^2} \tag{3.2}$$

where $c = 2(\sin 11°)2 \approx 0.07$ for hard brittle film on softer substrate; t is film thickness; $d \approx (1/7)D$ is the indentation depth, D is the imprint diagonal [71]. This equation is valid for surface displacement higher than the film thickness.

Furthermore, in order to take into account the Indentation Size Effect (ISE), consisting in the variation of the apparent microhardness with applied load (usually it increases with decreasing) [72,73], the correct expression for the Hc, based on the ‘‘law-of-mixtures’’ approach and taking into account for ISE, is:

$$H_c = H_{s0} + \frac{B_s + 2c_1 t(H_{f0} - H_{s0})}{2c(t/d) - c^2(t/d)^2} \tag{3.3}$$

where $c_1 = c(D/d) \approx 0.5$; H_{f0} and H_{s0} are intrinsic hardness of film and substrate, respectively; B_s is a coefficient, which can be determined from a separate experiment on substrate hardness [73]. To evaluate H_{s0} and B_s values, hardness of the Ti substrate has been measured. The relation between the measured substrate hardness, Hs, and the reciprocal length of the indentation imprints is expressed by the following equation:

$$H_s = H_{s0} + \frac{B_s}{D} \tag{3.4}$$

The H_s value obtained for the titanium substrate has been 1.6±0.1 GPa. The glass-ceramic films are hard and brittle film on a soft substrate and its plastic deformation allows to use the equation 3.2 for the H_f calculation.

3.9 Bone-like apatite formation on RKKP_Mn coatings obtained by PLD

3.9.1 RKKP_Mn preparation and characterization

RKKP_Mn glass-ceramic has been developed by A De Stefanis and J.V. Rau at ISM-CNR (Montelibretti and Tor Vergata Unit, respectively). The material has been synthesized by the sol-gel procedure (described in section 3.6.1) with an only variation: $Mn(NO_3)_2$ (2%) has been added as Mn^{2+} source.

Phase crystallinity and composition have been studied by ADXRD, Raman and FT-IR techniques (described in sections 3.3.3 b, c, and d, respectively).

3.9.2 Biological tests

These tests have been carried out at the Institute of Biomaterials, Department of Materials Science and Engineering, University of Erlangen-Nuremberg, heated Prof. Dr.-Ing. habil. Aldo R. Boccaccini.

a *WST-8 viability tests*

Viability test has been carried out by the using of ostoblast-like MG-63 cells. MG-63 cells have been incubated with different amounts of RKKP_Mn powder (0.1, 1.0 and 10.0 mg/ml), suspended in DMEM (Dulbecco's Modified Eagle Medium | Thermo Fisher Scientific). DMEM was supplemented with 10 vol.% FBS, 1 vol.% PenStrep and 200 mM L-Glutamine. The cell viability has been measured after 2 days of coculturing by the means of a cell counting kit was used (CCK - 8, Sigma-Aldrich). A mastermix of 1 vol.% WST-8 in DMEM without phenol red has been added to the culture and incubated for 2 h. During incubation, WST-8 (a water-soluble tetrazolium salt) is reduced to an orange-colored formazan through 1-methoxy PMS by NADH and NADPH, generated by cellular activities. Since The amount of WST-8 formazen is dependent on the activity of cellular dehydrogenase, therefore viable cells convert the WST in formazan dye with specific absorbance at 450 nm [74]. The spectrophotometric measurements have been performed by UV-Vis microplate reader (PHOmo, Autobio Labtec Instruments).

b *Calcein AM and DAPI staining*

To analyze the adherent alive cells, Calcein AM (acetoxymethyl) (Molecular Probes, The Netherlands) cell-labelling solution has been used for staining the cytoplasm of the cells. The modification of carboxylic acids with AM ester groups results in an uncharged molecule that can permeate cell membranes. The hydrolysis of the esterified groups allows the transformation from colorless nonfluorescent AM ester to the fluorescent form.

After removing the cell culture medium, 0.25 mL staining solution (0.5 vol% of dye labelling solution and 99.5 vol% of PBS) have been fixed by 3.7 vol% paraformaldehyde, washed again and stained with DAPI (40,6-diamidino-2-phenylindole dihydro- chloride, Roche, Basel, Switzerland) to label the nucleus. After 5 minutes of incubation, the solution has been removed and the samples left in PBS.

c *Fluorescence mycroscopy*

A fluorescence microscope (Axio Scope, ZEISS, Germany) has been employed for the detection of green calcein fluorescence and blue DAPI colour. By the using of two proper filter two separate images have been acquired and overlapped after the registration, in order to individuate the nuclei in the green coloured cytoplasma.

d *In vitro evaluation of bioactivity: SBF assessment*

For the assessment of bioactivity in vitro, the standard protocol introduced by Kokubo et al has been followed [63], as described in section 3.4.3 d. SEM-EDX, ADXRD , FT-IR and micro-Raman analysis and (set-up in sections 3.5.3 a, 3.3.3 b, 3.5.1 a and 3.3.3 c, respectively) have been carried out to evaluate the formation of hydroxyapatite on the coatings.

3.9.3 Films deposition and characterization

The RKKP_ Mn pellet has been used as target for the deposition of the thin films applying a PLD technique. PLD experimental setup is described in section 3.1. The films deposition has been performed at 12 J/cm^2 of laser fluence for a deposition time of 4 h; substrate has been positioned at 2 cm from the target and its temperature has been kept at room temperature (RT) and 500 °C. Ti substrates (Ti foil, 99.6%, GoodFellow) squares of 1 × 1 cm^2 geometry have been previously sandblasted with a 60-grid SiC abrasive powder in order to assure nanometric surface roughness and boiled in aqua regia for 30 min, in order to remove any contaminant from the surface.

ADXRD and SEM-EDX analysis (described in section 3.3.3 b and e) have been carried out on the film in order to study crystalline phases, morphology and composition.

a *In vitro bioactivity test: soaking in SBF*

The in vitro SBF assessment has been carried out exactly in the same way described in section 3.4.3 d. And the growth of hydroxyapatite on the coating surface has been evaluated by micro-Raman, ADXRD and SEM-EDX (described in section 3.3.3 c,b and e).

CHAPTER 4

Coatings based on apatite

Among the prominent calcium phosphate salts found in bone, such as. brushite ($CaHPO_4 \cdot 2H_2O$), octacalcium phosphate ($Ca_8H_2(PO_4)_6 \cdot 5H_2O$), calcium hydroxyapatite ($Ca_{10}(PO_4)_6(OH)_2$), the latter is the dominant lattice structure of hard tissue. This is the reason why hydroxyapatite (HAp) has been widely used in orthopaedics and dentistry in form of granules as bone filler, in tooth pastes and bone cements, as scaffold in non load-bearing sites and in form of thin coating on metal substrates for dental or bone implants [14]. However, it is characterized by a low osteogenic activity, in fact, longer time period is reported for substantial bone bonding to the implant surface and this disadvantageously increases patient rehabilitation time. The incorporation into HAp structure of various metal ions or inorganic salt anions may significantly influence structural, physico-chemical, mechanical and biological properties of HAp-based ceramics [75]. In particular, the possibility to substitute Ca^{2+} ions with other metal ions is an important property of HAp. Therefore, it has continuously been used as host material for the doping of various ions, singly or multiply in many combinations, with the aim of enhancing its biological activities [22]. Sodium, magnesium, potassium, manganese, strontium, zinc, barium, copper, aluminium, iron, fluorine, chlorine, and silicon can be considered as appropriate candidate for ion substitution because they are already present in bone apatite at trace levels due to safety purposes.

Among the coating technique, plasma spraying is the most commonly used technique for the production of hydroxyapatite coatings, however there are several drawbacks to overcome. During plasma spraying deposition, hydroxyapatite powder is heated above its melting point in order to forma plasma-gas stream, which is accelerated towards the substrate. The result is a coating containing a mixture of phase with a non controllable distribution, poor adhesion, poor integrity, irregular resorption in body fluid and mechanical failure at the coating/substrate interface [76,77]. Nevertheless, in the last decade the replacement of plasma-spraying technique with processes that allow to produce thin and well adherent films is a attractive issue for the researchers community. In this context, pulsed laser deposition technique (described in section 2.1) is a highly performant method and, although high quality hydroxyapatite thin films deposited by PLD have been obtained for the first time in 1992 by Cotell [78], this technique is not released for commercial use yet, however several research studies are constantly improving and testing it, and proving its potentialities [79].

4.1 Composite HAp/IONPs films deposited by pulsed laser deposition

This work has been carried out in collaboration with the CNR-ISM, UOS Tito Scalo (Potenza), where the laser ablation in liquid has been performed, and the CNR-ISM, Monterolo Scalo (Roma), where the magnetic measurements have been carried out.

4.1.1 Introduction

Magnetic nanoparticles (NPs) are attracting an increasing interest in the scientific community for their many potential technological applications from the magnetic storage to biomedical applications.

In biological field, the most suitable magnetic NPs are iron based magnetic oxides, which represent the best compromise between good magnetic properties on one hand and limited toxicity and stability under oxidizing conditions on the other hand. A number of potential application have already been investigated, such as targeting drug delivery [80], controlled drug release [81], hyperthermia treatment of cancers [82], labelling of biological entities, magnetic separation [83,84] and enhancing of the contrast in magnetic resonance imaging [85,86].

The possibility to use magnetic NPs in the hard tissue repair is attracting the interest of a number of researchers. Recent studies have indeed demonstrated that the presence of Fe^{3+} ions affects the crystallinity and solubility of hydroxyapatite (HAp) [87,88], while small amount of iron were found to have a positive impact on HAp biomedical properties [89]. Moreover, it has been showed that the presence of magnetite NPs improve the HAp layer growth encouraging HAp nuclei formation due to electrostatic interaction with SBF solution [90].

In addition, magnetized HAp scaffolds or coatings can be used as support matrix for cells delivery, in particular stem cells, for a remote magnetic controlled bone regeneration [91].

Several synthetic approaches exist for the production of iron/iron oxide nanoparticles (IONPs), however, in order to employ IONPs for biomedical applications, a "green chemistry" procedures is advised, in order to limit the presence of residues which may be toxic for the organism [92]. For this purpose, pulsed laser ablation in liquid (PLAL) can be proposed as a valid approach because the use of undesired chemical precursor or additives is not required and does not produce toxic by-products [93].

PLAL is a flexible and efficient one-step method to produce metallic and alloy NPs and nanostructures by a one-step synthesis [94,95]. This technique, similarly to PLD, is based on the interaction between an intense laser beam and the target material. In this case the target is submerged in a liquid. Therefore the plasma resulting from the interaction laser-matter is confined by the surrounding liquid and a state of high pressure and temperature takes place [96], causing the formation of a cavitation bubble. Inside the bubble, the rapid quenching of the high temperature laser induced plasma provides the formation of polycrystalline NPs [97]. Since a reaction between the liquid molecules and the ablated material can occur, by the variation of the target composition as well as the surrounding liquid it is possible to change the properties and the composition of the obtained nanoproducts, whereas laser parameters such as laser fluence, repetition rate and ablation can determine both the observed particle size distribution and colloidal solution concentration. IONPs have been already obtained by laser ablation of a metallic target in water by using different laser sources [98–100].

In the present work, the IONPs obtained by PLAL in water have been used in a mixed target with HAp for the pulsed laser deposition of a composite films. The physical-chemical properties of the particles before and of the obtained coating then have been evaluated from a structural, compositional and morphological point of view. The study of the plasma evolved during the PLD process has been useful to understand the obtained compositional and magnetic features of the films.

4.1.2 Results and discussion

a *IONPs characterization*

First of all IONPs characterization has been carried out. TEM images (Figure 4.1 (a)) show the presence of spherical and not aggregated particles, whose diameter has been evaluated of 42±20 nm, considering more than 560 particles (Figure 4.1 (b)). HR-TEM images (Figure 4.2) allows to observe the presence of different crystalline domains, confirming that particles obtained by laser ablation in liquid are polycrystalline. Interplanar distances of crystalline domains, retrieved by Fast Fourier Transform (FFT) image reported in Figure 4.2, have been related to the presence of iron oxides and metallic iron, as summarized in Table 4.1. In particular, interplanar distance of 0.50 nm can be referred to (113) plane of γ-Fe_2O_3, 0.31 nm to (110) FeO [101], 0.21 to (110) α-Fe [102] and 0.48 nm to (111) Fe_3O_4 [103]. IONPs phase composition has been confirmed by XRD analysis (Figure 4.3 (a)), the measured signals at 35.3°, 57.1° and 62.7° has been assigned to magnetite (ICDD PDF 01-076-1849), signals at 36.3°, 42.1° and 61.3 has been assigned to wuestite (ICDD PDF 00-002-1186) and signal at 44.6° to α-iron (ICDD PDF 01-087-0721). The presence of maghemite phase cannot be ruled out. In fact, it has been reported that it is difficult to distinguish between maghemite and magnetite signals since contributions of these two phases are extremely close to each other due to their similar crystalline lattice parameter [104].

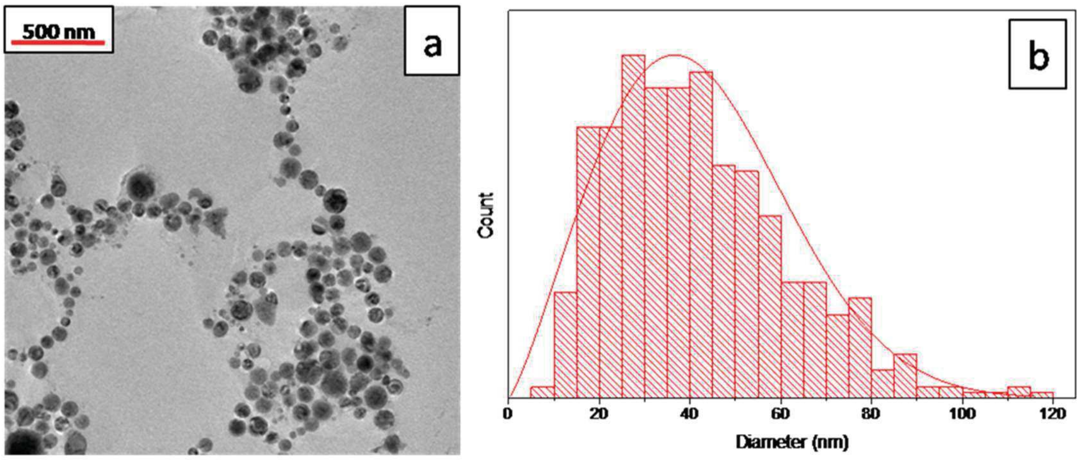

Figure 4.1: TEM image (a) and particles size distribution (b) of IONPs obtained by LAL.

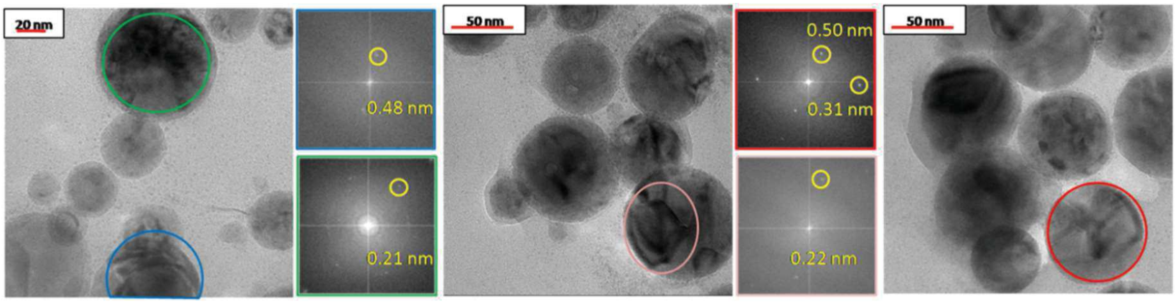

Figure 4.2: HR-TEM image of IONPs obtained by LAL and 2D fast FFT performed on the region indicated by the coloured line.

Table 4.1: Lattice planes retrieved from the FFT in Figure 4.2.

Interplanar distance (nm)	Lattice planes
0.21	(110) α-Fe (400) Fe_3O_4
0.22	(200) FeO
0.31	(110) FeO
0.48	(111) Fe_3O_4
0.50	(113) γ-Fe_2O_3

Further evidence of this hypothesis has been provided by Raman analysis (Figure 4.3 (b)). A pronounced magnetite feature at 665 cm^{-1}, attributed to the A_{1g} mode is evident in the Raman spectrum. In addition magnetite weaker signals , at 330 and 520 cm^{-1} of T_{1g} vibrational mode, are overlapped by the more intense signals of maghemite phonon modes: the T_{2g} at 360 cm^{-1} and the E_g at 495 cm^{-1} [105]. Moreover, the asymmetry of the most intense signal of magnetite could be due to the contribution of the A_{1g} mode of maghemite. By Raman technique, it is not possible to detect wuestite phase [99].

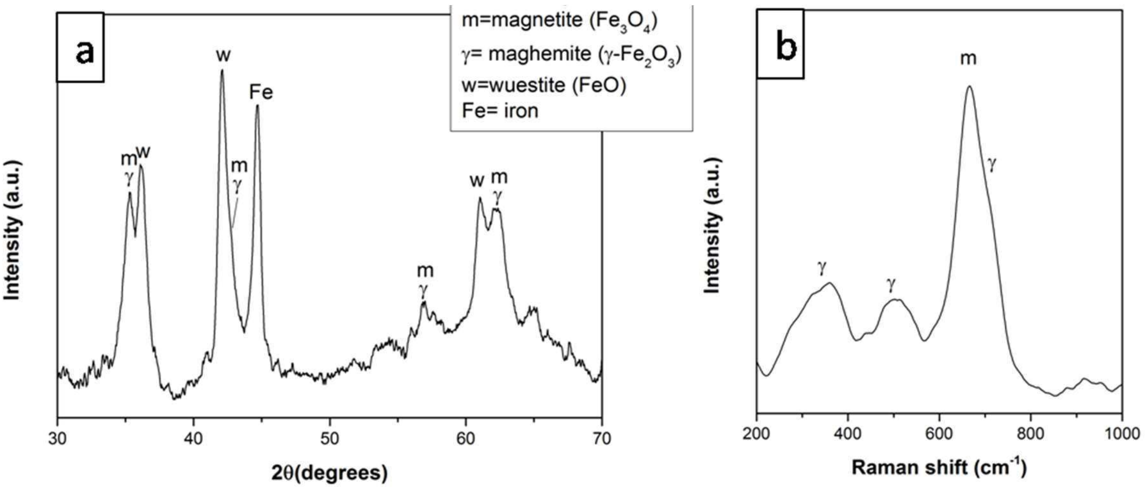

Figure 4.3: XRD pattern (a) and Raman spectrum (b) of IONPs obtained by LAL.

The magnetization field dependence at 5 K (Figure 4.4 (a)) confirms the presence of different magnetic phases in a sample which is characterized by NPs with a large distribution of size and magnetic anisotropies. In particular, a double step hysteresis loop can be observed in the low field regime (inset Figure 4.4 (a)), with a drop of magnetization that can be attributed to the soft metallic Fe phase. The temperature dependence of the coercivity Hc (Figure 4.4 (b)) manifests a significant drop around 200 K, where all the IONPs enter the superparamagnetic regime.

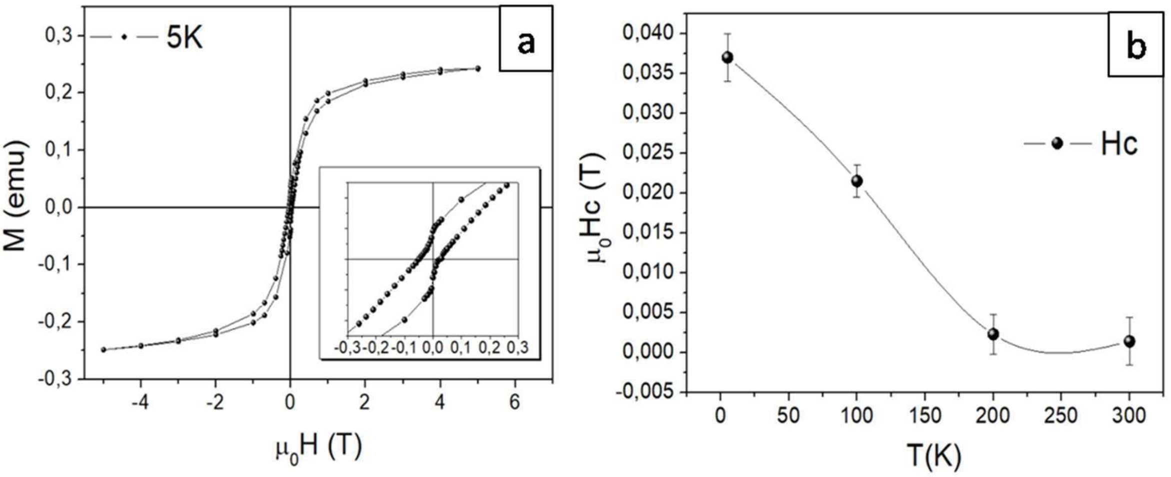

Figure 4.4: Magnetization field dependence at 5 K (a); variation of coercivity as a function of temperature (b) of IONPs obtained by LAL.

b *Composite HAp/IONPs films characterization*

Once the nanoparticles have been characterized, the target prepared by the mixing of HAp with IONPs (4 wt%) has been deposited by nanosecond PLD, varying the deposition temperature in order to obtain crystalline films.

To get information about the early step of film formation, thus to hypothesize the film's growth mechanism, TEM analysis has been performed. In TEM image (Figure 4.5 (a)), it is possible to observe a dense background of small nanoparticles, that can be due to a process of gas-phase condensation, overlapped by large fused spherical particles (hundreds of nanometers large) formed by coalescence of droplets.

The HR-TEM image (Figure 4.5 (b)), shows the presence of nano-domains. From the relative FFT (Figure 4.5 (c)), the interplanar distances measured have been 0.28 and 0.37 nm, which can be related to (211) and (012) planes of HAp [106], respectively, and 0.29 and 0.48 nm, related to (220) and (111) Fe_3O_4 [107], respectively, as summarized in Table 4.2. The presence of wuestite domains have also been observed. It is important to highlight that none of the measured interplanar distance can be referred to metallic iron.

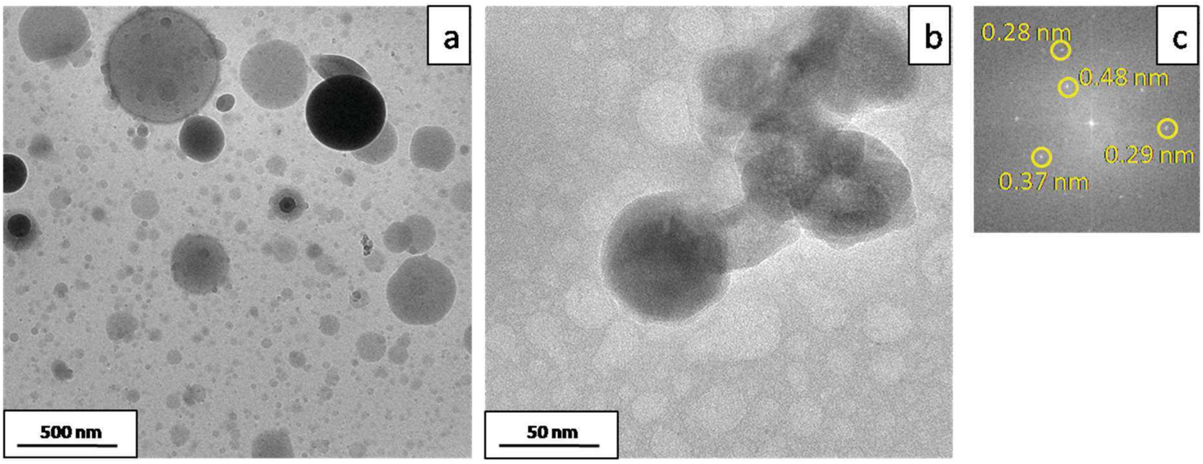

Figure 4.5: TEM image (a) and HR-TEM image of HAp/IONPs film deposited at room temperature (b) and 2D FFT (c).

Table 4.2: Lattice planes retrieved from the FFT in Figure 4.5.

Interplanar distance (nm)	Lattice planes
0.28	(221) HAp
0.29	(220) Fe_3O_4
0.31	(110) FeO
0.37	(012) HAp
0.48	(111) Fe_3O_4

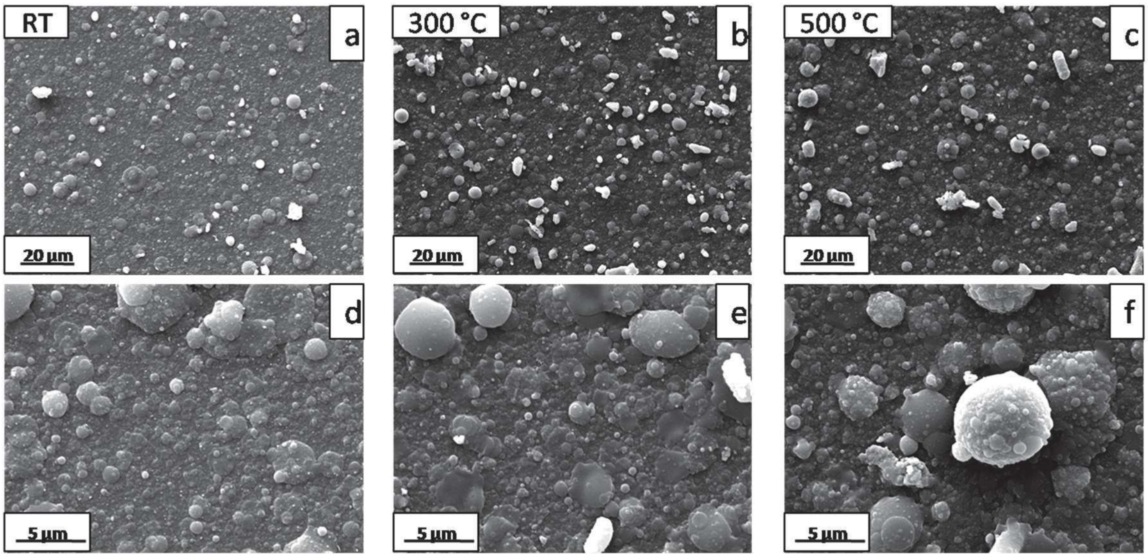

Figure 4.6: SEM images collected on the films deposited at RT (a, d), 300 °C (b, e), 500 °C (c, f), at two different magnification.

Irrespective from deposition temperature, all films are dense and uniform, consisting of quite spherical micrometric droplets coalesced over a dense layer, as shown in SEM micrographs (Figure 4.6). Due to the increased particles mobility at higher deposition temperature, in films deposited at 500 °C the coalescence of smaller particles can be observed together with the presence of bigger spherical particles [108,109]. Moreover, large particles are covered by nanometric grains, that is more evident in the image at higher magnification (Figure 4.6 (f)).

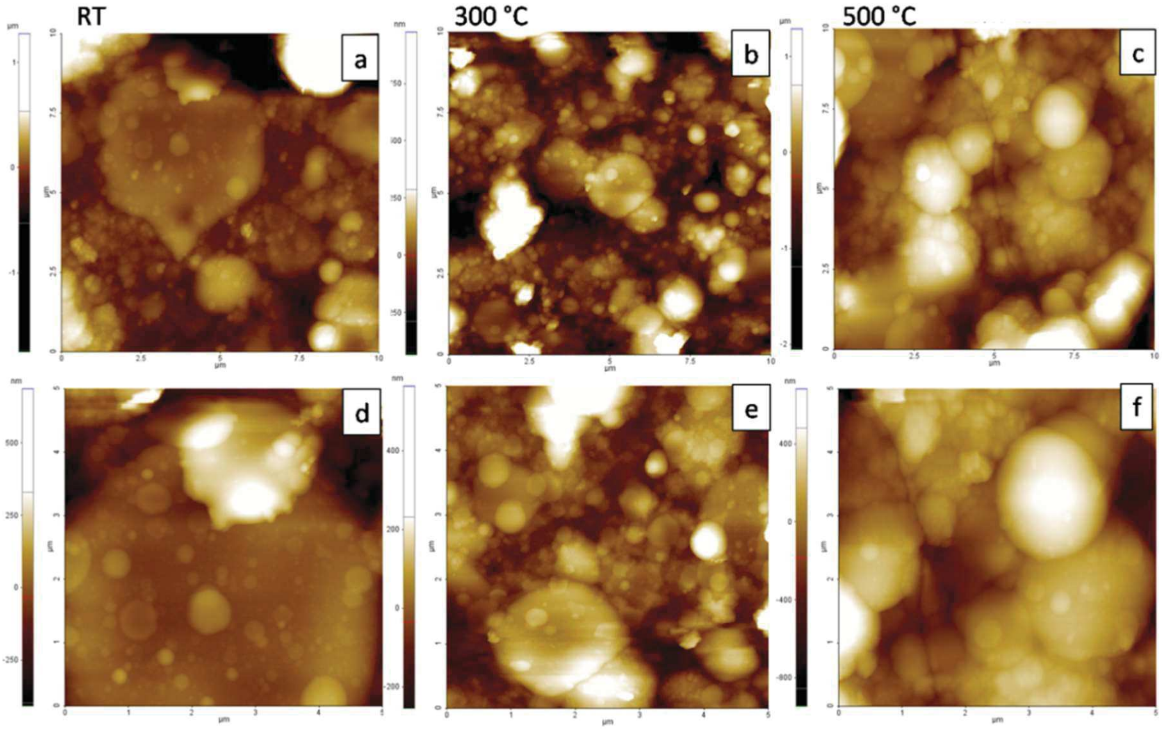

Figure 4.7: AFM images collected on the films deposited at RT (a, d), 300 °C (b, e), 500 °C (c, f), at two different magnification: 10×10 μm^2 (a, b, c) and 5×15 μm^2 (d, e, f).

AFM images (Figure 4.7) show a granular surface topography with micro and nano cavities on all films. Two different domains can be clearly distinguished: micrometric grain size structures uniformly distributed on a submicron size texture. The evolution of surface morphology with the deposition temperature has been observed. In fact, top-flat micrometric droplets are evident in films deposited at RT, whereas bigger spherical particles characterize the film deposited at 500 °C. Coatings average surface roughness (in term of root mean square, r.m.s.) has been calculated on several 10×10 μm^2 AFM images (Figure 4.7 (a-c)), by the integration of the whole area. The r.m.s. value increases with the increasing of the deposition temperature. Although no significant differences can be appreciated between the films deposited at RT and 300 °C, for which the r.m.s. is 131 (±27) nm, and in 155 (±36) nm, respectively, the film deposited at 500 °C, as expected, has a r.m.s. of 318 (±40) nm. Since these values are more effected by the micrometric structure, r.m.s. has been calculated in region free of the largest particles (mountains) in order to estimate the roughness of the nanometric texture. The obtained values are quite similar irrespective to the deposition temperature, and is of tens of nanometers.

Such morphological characteristics and roughness should have beneficial effects on the coating bioactivity. In fact, it has been demonstrated that multi-scale surface roughness can promote different biological responses at the implant surface [43,110,111]: micron sized particles, similar in size to cells, may stimulate adhesion and differentiation; on the other hand, smaller nanoparticles may induce the absorption of proteins involved in the regulation of osteoblast proliferation. Therefore, films like that produced by PLD, characterized by the combination of microscale and nanoscale features, may affect positively the osteintegration of the implant.

Film's composition, structure and magnetic properties have been investigated with a multi-technique approach by using FT-IR, EDX, XRD and SQUID magnetometry.

By EDX analysis (Table 4.3) an excess of calcium with respect to the expected HAp ratio has been measured, probably due to the carbonation effect, usually observed during PLD process in vacuum [77]. Moreover, the presence of iron is confirmed for all films, with an amount of about 4 wt%.

Table 4.3: EDX elemental analysis results for HAp/IONPs target and films.

Element	Target material	Dep RT	Dep 300°C	Dep 500°C
O	42,35	42,61	37,43	36,28
Fe	3,58	5,19	4,41	3,31
P	17,86	11,89	14,58	14,29
Ca	36,2	40,3	43,58	46,12

All the elements in wt %

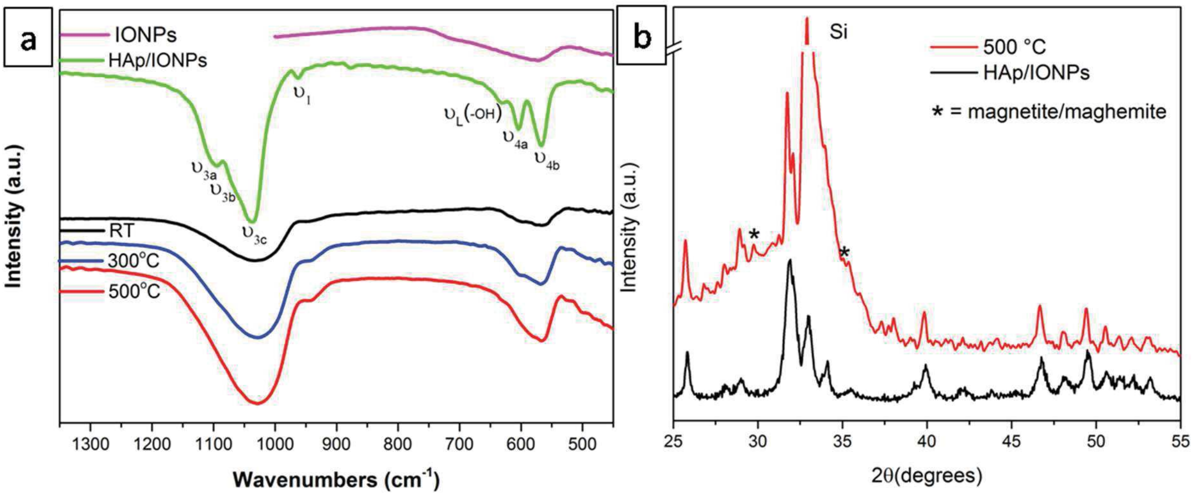

Figure 4.8: FTIR spectra of IONPs, HAp/IONPs target and the films deposited at RT, 300 °C and 500 °C (a); XRD pattern of the film deposited at 500 °C and the target material (b).

The FTIR spectra of the target and the films are reported in Figure 4.8 (a). In FTIR spectrum of the target it is possible to observe typical HAp signals. The splitting of the PO_4^{3-} bending and anti-symmetrical stretching modes is observed, which testifies the good crystallinty of the target material [112]. In particular, signals at 567 and 604 cm^{-1} have been assigned to ν_{4c} and ν_{4a} PO_4^{3-} bending mode, respectively, and signals at 1037, 1070 and 1094 cm^{-1} to ν_{3c}, ν_{3b} and ν_{3a} PO_4^{3-} anti-symmetrical stretching mode [112], respectively. In the spectrum are also visible the ν_1 PO_4^{3-} (stretching mode) at 960 cm^{-1} and the ν_L OH^- at 631 cm^{-1}. In the spectra of the deposited films, the two phosphate anti-symmetrical stretching and bending modes converge in a single band, suggesting the reduction of the crystallinity in the composite films. Therefore, the ν_4 PO_4^{3-} is around 570 cm^{-1},the ν_3 PO_4^{3-} is around 1039 cm^{-1}. Since the spectrum of IONPs shows a large band with a maximum around 570 cm^{-1}, related to the T_{1u} mode of magnetite or maghemite [105], iron oxide species are not detectable in the films' spectra. In fact, they are in low percentage in the film and their identifying signal is very close to the phosphate bending mode.

In XRD spectrum, in Figure 4.8 (b), of film deposited at higher temperature it is possible to appreciate diffraction peaks ascribable to hydroxyapatite phase (ICDD PDF 01-074-0566), accompanied to low intensity signals at 29.8 ° and 35.4 ° that can be assigned to magnetite phase (ICDD PDF 01-076-1849). The presence of maghemite phase cannot be definitively ruled out. However, no contribution of wuestite and metallic iron has been detected, confirming the results obtained by HR-TEM images (Figure 4.5).

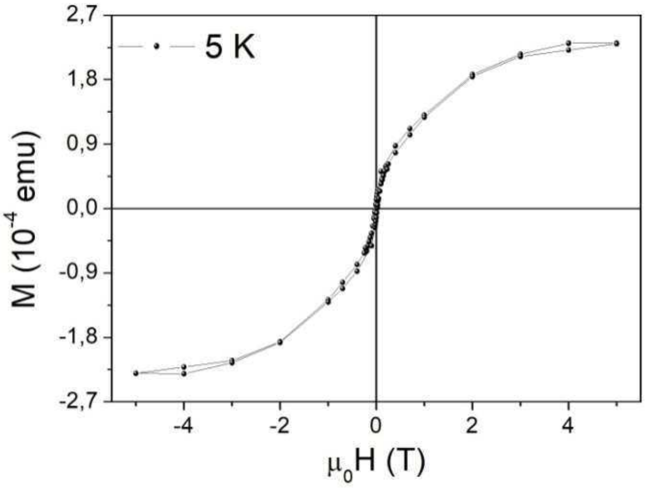

Figure 4.9: Magnetization field dependence at 5 K of the film deposited at 500 °C.

Magnetic properties of all film samples result almost independent on the deposition temperature. Although the lower magnetic signal with respect to the powder, it is evident from the hysteresis loop (Figure 4.9) the superparamagnetic character even at 5 K; the absence of the low field double step observed in the powder samples support the hypothesis of the disappearance of the metallic iron in the ablated material.

c *Spectroscopic characterization of HAp/IONPs laser induced plasma.*

In order to explain the film composition and properties, thus the lack of metallic iron, the ablation mechanism has to be considered. Therefore the plasma characterization has been carried out. In fact, during a PLD experiment, very complex physical and chemical phenomena are involved starting from laser–material interaction, to the formation and expansion of the plasma plume and ending with the film growth. All these processes have been well described in section 2.1. In brief, when the laser beam interacts with the target material all elements in the outer layers of the target are vaporized to form a plasma. The plasma is composed of atoms, molecules, ions and electrons, with a kinetic energy dependent on the laser parameters (i.e. intensity, wavelength, pulse duration) and to some degree the target sample. The plasma, expands in an approximately adiabatic way, with an angular distribution described by a $\cos^{n}(\theta)$ [51], where θ is the angle between target normal (plume direction) and laser beam and *n* is parameter that takes into account of the anisotropy of the plasma. Finally, when the plasma comes in contact with another surface, the substrate, it may recondense on it. Repeated laser pulses, thus repeated plumes, lead to build up material on the substrate surface to form the so termed thin film.

The HAp/IONPs plume expansion has been studied by the collection of ICCD images, reported in Figure 4.10. Whereas, by the acquiring of optical emission spectra, the plasma species have been detected (Figure 4.11) and their velocity has been determined (Figure 4.12). In addition, by the means of Boltzmann plot method, it has been possible to calculate the electron temperature (Figure 4.13).

With ICCD imaging only the primary plasma emission has been detected, as usual for nanosecond laser ablation, whereas direct expulsion of particles from the target material, which sometimes occurs with a ns-PLD, has not been detected. In the light of this results, the films morphology can be rationalised: as supposed, the film's growth is based on condensation of gas phase, which contribute to the compact and dense background, and coalescence of melting droplets, which lead to the formation of the overlapping large fused spherical particles.

The ICCD images, reported in Figure 4.10, have been acquired at different time delays with gate of 100 ns. The plasma plume has been characterized by a front velocity of about

3.5 10^6 cm/s, as usual for nanosecond ablation process in vacuum [53] and an emission lasting up to 1.5 μs. As regards the angular distribution of the plasma, the calculated *n* parameter has been of 1.6.

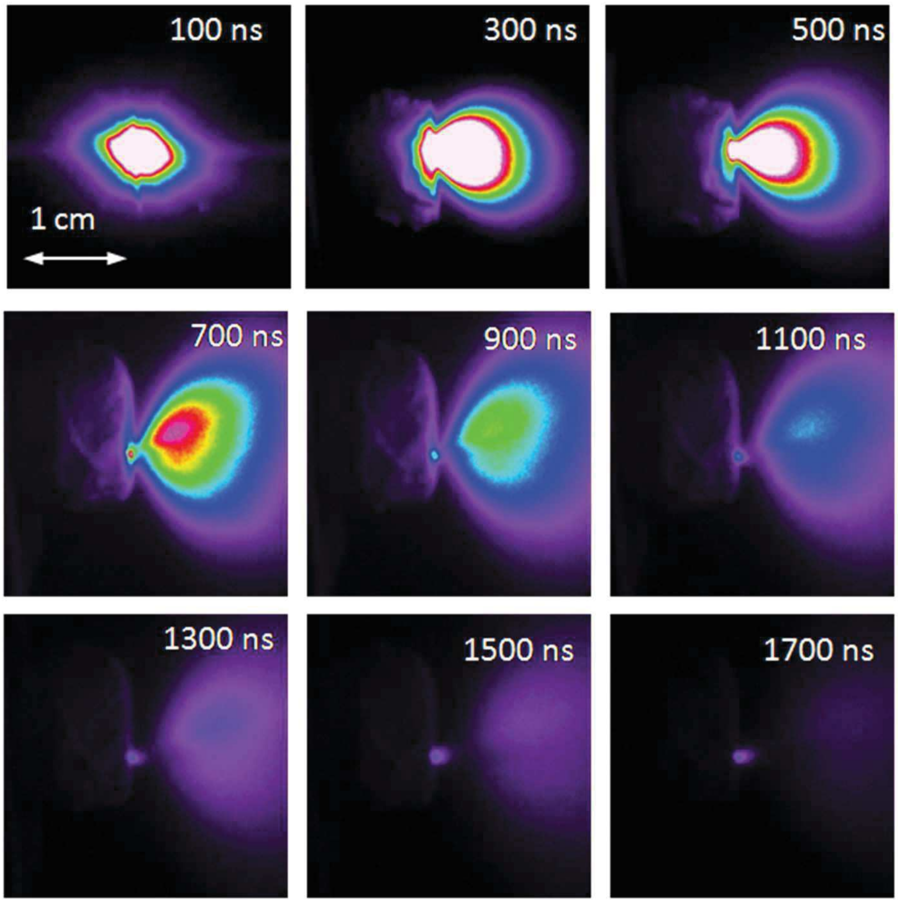

Figure 4.10: ICCD images of the plasma emission, acquired each 100 ns after the laser pulse with a gate width of 100 ns.

By the means of optical emission spectroscopy (OES), the different emission lines have been detected assigned to neutral (Ca I and O I) and ionic species (Ca II, Ca III, P II, Fe II and O II). In this reactive environment, iron species can suffer an oxidation process, thanks to the presence of an high amount oxygen ions. In this view, the absence of metallic iron in the deposited films, resulted from XRD and HR-TEM analysis, can be related to this second laser ablation process.

Several space and time resolved emission spectra have been registered in different wavelength range varying the position of the optical elements (distance 0, 1 and 2 mm from the target) and the delay time (from 10 to 400 ns, with gate width of 10 ns). In figure 4.11 a 3D graph related to the evolution of the emission spectra of the HAp plasma in the wavelength from 412 to 431 nm is reported at various delays.

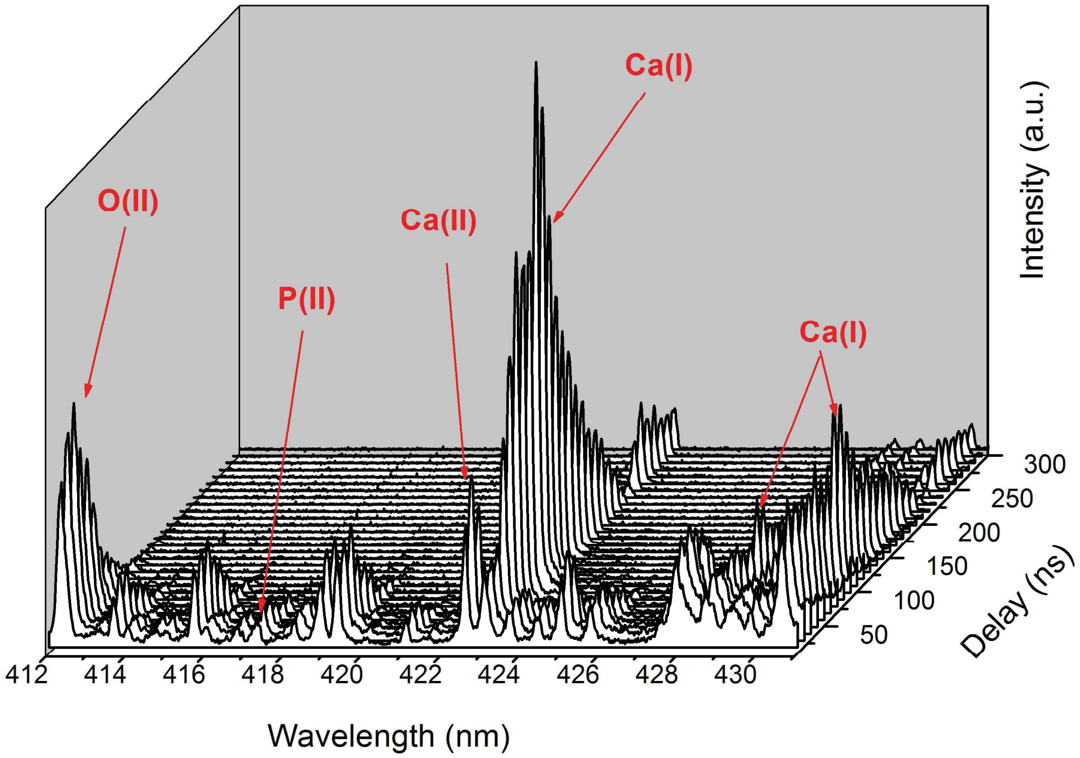

Figure 4.11: Evolution of the emission spectra of HAp plasma in vacuum for various delays.

From the optical emission spectra, time-resolved emission plots can obtained. In Figure 4.12 (a) the normalized time-resolved emission plots of the different species, related to the spectra acquired at distance 1 mm from the target, is shown.

From the values corresponding to the maximums of the time-resolved plots, recorded at different distances from the target, it is possible to calculate the velocity of the various species present in the plasma. In Figure 4.12 (b) normalized time-resolved emission plots of Ca I for different distance from the target. are reported as example. In fact, in order to calculate the velocity (v) of a specie, it is necessary to solve the following equation (4.1):

$$v = \frac{(d_2 - d_1)}{(t_{2\,max} - t_{1\,max})} \tag{4.1}$$

where $t_{1\,max}$ and $t_{2\,max}$ are the time where the maximum of the intensity has been observed at distance d_1 and d_2, respectively. Moreover, since there is a correlation between the kinetic energy (*KE*) of these species and the observed film properties [113], *KE* has been directly calculated from the velocity values .

In Table 4.4 the velocity and the kinetic energy values calculated for each founded species are reported. As regards the iron species, the detected signals have been not enough intense for a time range sufficiently large for the calculation. The obtained values of velocity are in agreement with the plasma front velocity observed by the acquisition of the ICCD images. As expected heavier species move slower than the lighter, while their velocity increases with the charge. This behaviour is described by the space-charge acceleration model. Electrons inside the plasma are obviously much lighter, therefore they have much greater mobility than ions or neutrals, but are prevented from escaping from the dense plasma by the strong Coulombic attraction to the ions. The electrons at the periphery of the expanding plume attract and accelerate proximate ions thanks to the Coulombic attraction, thereby inducing further acceleration of the charged components inside the plume [113,114]. Moreover the kinetic energy values calculated are typical of ns-PLD. These values are below the film damage threshold, therefore they cannot affect the film structure and morphology [113].

Table 4.4: Velocity and kinetic energy of the different species.

Species	**O I**	**Ca I**	**O II**	**Ca II**	**P II**	**Ca III**
$v\cdot 10^6$(cm/s)	3.0	2.2	3.3	3.0	3.3	3.3
***KE* (eV)**	74.6	100.4	90.2	186.8	174.1	225.9

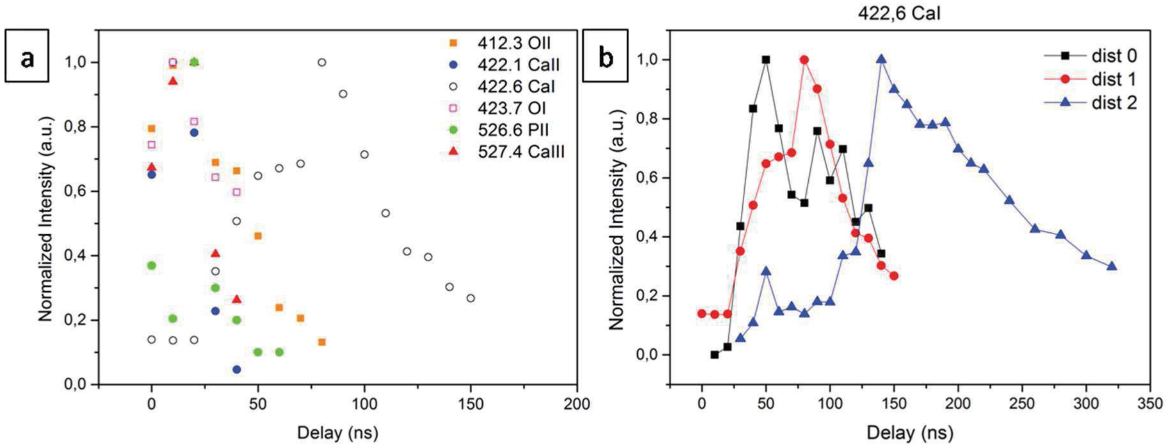

Figure 4.12: Normalized time-resolved emission plots of all the species, recorded at 0.5 mm from the target (a), normalized time-resolved emission plots for Ca I (422.6 nm), recorded at different distances from the target. The lines which connect the experimental data were added to facilitate the understanding of the graphics (b).

From OES it is possible to obtain another important parameter, the plasma excitation temperature (T_e), which is determined, assuming valid the local thermodynamic equilibrium (LTE) [115], through the Boltzmann plot method from the relative intensities of the observed line, which are normally proportional to the population of the pertinent upper levels. The following relation has been used to extract the plasma temperature (4.2) [116].

$$ln\left(\frac{I_{2,1}\lambda_{2,1}}{A_{2,1}g_2}\right) = ln\left(\frac{N(T)}{U(T)}\right) - \left(\frac{E_2}{k_b T_e}\right) \tag{4.2}$$

where $I_{2,1}$ is the integrated line intensity of the transition from an upper level (2) to a lower level (1), $\lambda_{2,1}$ is the transition wavelength, A_2 is the transition probability, g_2 is the statistical weight of level (2). N(t) is the total number density, U(T) is the partition function. E_2 is the energy of the upper level, k_b is the Boltzmann constant, and T_e is the electron temperature.

A linear plot of $ln(I_{2,1}\lambda_{2,1}/A_{2,1}g_2)$ versus the term energy E_2 gives a slope equal to ($-1/k_b T_e$). Thus, the electron temperature can be determined without the knowledge of the total number density or the partition function. The intensity $I_{2,1}$ of the line at $\lambda_{2,1}$ has been obtained by fitting the detected emission signal with a Voigt function. In Table 4.5 the spectroscopic parameters (taken from NIST atomic spectra database [117]) of the Ca I used for the T_e determination are listed.

Table 4.5: Spectroscopic parameters of the Ca I lines used for the determination of T_e.

$\lambda_{2,1}$ (nm)	Transition 2→1	$A_{2,1}$ (s^{-1})	g_2	E_2 (cm^{-1})
422.673	$3p^64s4p\ (^1P°) \rightarrow 3p^64s^2\ (^1S)$	2.18×10^8	3	23652.304
428.301	$3p^64p^2\ (^3P) \rightarrow 3p^64s4p(^3P°)$	4.34×10^7	5	38 551.558
430.774	$3p^64s5s\ (^3P) \rightarrow 3p^64s4p\ (^3P°)$	1.99×10^8	1	38 551.558
610.272	$3p^64s5s\ (^3S) \rightarrow 3p^64s4p\ (^3P°)$	9.6×10^6	3	31 539.495
612.222	$3p^64s5s\ (^3S) \rightarrow 3p^64s4p\ (^3P°)$	2.87×10^7	3	31 539.495
616.217	$3p^64s5s\ (^3S) \rightarrow 3p^64s4p(^3P°)$	4.77×10^7	3	31 539.495
643.907	$3p^63d4p\ (^3F°) \rightarrow 3p^63d4s\ (^3D)$	5.3×10^7	9	35 896.889
649.378	$3p^63d4p\ (^3F°) \rightarrow 3p^63d4s\ (^3D)$	4.4×10^7	5	35 730.454

In Figure 4.13 (a) the Boltzmann plot related to the signals detected with 60 ns of delay is reported as example. The T_e calculated in this case has been of 15000 K. The temporal evolution of the T_e is reported in Figure 4.13 (b). A typical exponential decreasing of the temperature is evident. The temperature drop is due to the LTE condition, according to

which the collision processes prevail over the radiative ones in the determination of the thermodynamic plasma parameters, therefore, during the plasma expansion, the thermal energy is rapidly converted into kinetic energy causing the exponential decrease of T_e.
The high founded temperature values, mainly at short delay time, are a confirmation of the high reactive environment that surround Fe atoms: high ionization degrees, together with the high amount of oxygen species allow a re-oxidation process if the IONPs inside the plasma, allowing the disappearance of metallic iron.

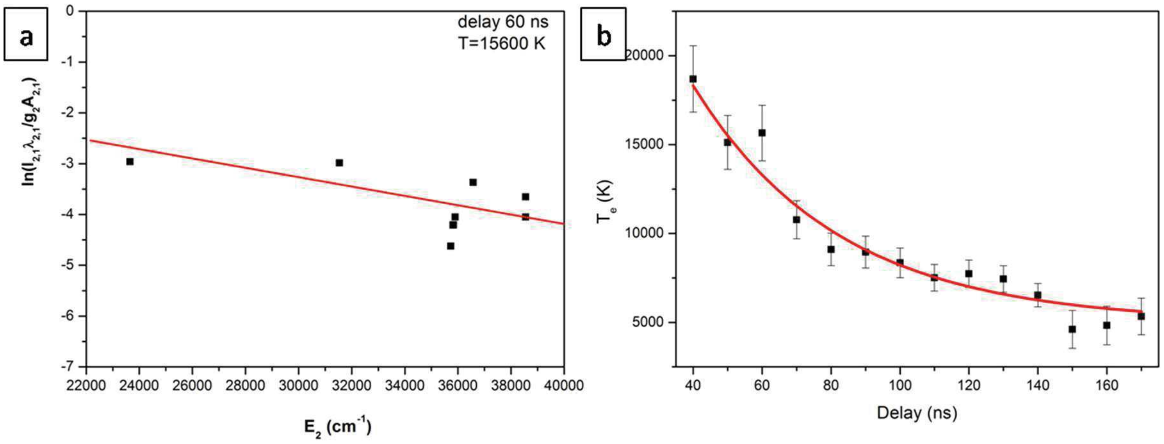

Figure 4.13: Boltzmann plot related to Ca I lines at 60 ns of delay (a); temporal evolution of the T_e (b).

The complete characterization of the deposited HAp/IONPs films has been carried out. The appropriate magnetic properties are due to the presence of magnetite-maghemite phases, while the presence of other iron species can be excluded. The films are characterized by compact microstructure and rough surface, especially the film obtained at 500 °C, which potentially promotes cells adhesion. Biocompatibility properties of HAp have been largely proved, and the "green" technique used for the IONPs production enables their usage in biomedical application. Furthermore, the presence of IONPs could improve the biological activity of the films. Such films should be incubated with proper cell line, in order to test their biological activity and to design them as magnetic support for cells delivery, in particular stem cells, for remote magnetic controlled bone regeneration.

CHAPTER 5

Coatings based on bioglasses

Since the invention of 45S5 Bioglass® (SiO_2–45, Na_2O–24.5, P_2O_5–6, CaO–24.5, all in wt%) by Professor Hench [26], the interest and even the clinical employing of silicate-based glasses as biomaterials for bone tissue replace and regeneration is growing up. Furthermore, numerous attempts have been made to improve its biological performances by the changing of the glass composition.

As described in section 1.3.2 b, the main structure of bioglass is a silicate network with a phosphate partner network, in which oxide of bivalent cations act as network modifiers [118]. The latter promote the silicate hydrolysing in contact with the biological fluids, resulting in the formation of a apatite layer at the boundary between the biomaterials and the fluid. The bioglass' capacity to release ions has inspired the researchers to introduce metal ions with specific activity in its composition [62]. Some metals ions, in fact, can influence the signalling pathways and the metabolic activity during the hard tissue formation since they act as enzyme co-factors [62,119]. Among the large variety of potential candidates, it has been proved that copper ions are involved during the extracellular matrix (ECM) degradation and remodelling [120]. In addition, Cu ions has been demonstrated to have an important role during tissue vascularisation stimulating the proliferation of human endothelial cells and the differentiation of mesenchymal stem cells (MSC) [121,122]. Accordingly, the incorporation of copper ions in bioglass materials leads to the increasing of (HIF)-1 (hypoxia inducible factor) and VEGF (vascular endothelial growth factor) expression [62,123].

The use of copper in biomedical field is desirable not only because it is an essential co-factor of several enzyme and for its proangiogenic properties, but also thanks to its antibacterial properties [124]. The risk to getting infections, especially during the implantation surgery is a serious complication for patients, which is currently difficult to treat with antibiotic therapy. In fact, some studies have shown that this type of infections are related to the formation of biofilms. Biofilms are the main form of life for the most microorganisms and germs in any hydrated biological system [125,126]. Over 80% of microbial infections in the body, including prostheses and other biomedical devices, are related to the formation of such biofilms, resulting in persistent and resistant to antimicrobial therapy infection [125,126]. The high number of bacteria inside a biofilm activates a cell-density-dependent mechanism, called quorum sensing (QS). QS systems regulate the expression of adhesion mechanisms and virulent factors. Microorganisms are embedded in a self-produced polysaccharide matrix adherent to a solid biological or non-biological surface. This extracellular matrix protects the bacteria impeding the eradication of the infection by the immune system and even the antibiotics. In this case the only solution is the implant removing [118,125]. Biofilms are not the only infections related to an implantation surgery and, although less dangerous, the risk of infection is higher for dental implantation therefore also the possibility of implants failure.

In this context it is advantageous to impart antibacterial properties directly to the employed biomaterials. Therefore, the introducing of copper ions into bioglass composition may be an effective strategy to limit infections and improve bone regeneration and tissue vascularisation [118]. Different research groups doped 45S5 Bioglass (BG) with different amount of copper and studied the effects of ion release. Goh at al. [118] proved the effectiveness of BG doped with copper as antibacterial materials. They compared the ion release of Cu-doped and Ag-doped BG, since silver is a known antibacterial agent. Cu-doped BG presented better long-term antibacterial properties. The introduction of Cu-doped BG in hydrogels, for the coating of medical tools, has been demonstrated by Wers et al [126] to improve its anti-adhesion character and to inhibit the formation of biofilms. Several works conducted by Boccaccini et al. [62,122,124,127,128] confirmed both angiogenic and antibacterial properties of Cu-doped BG . In one of the cited papers authors concluded with the following sentence:

"Since Cu shows angiogenic potential, osteogenic properties as well as antibacterial effects, the newly developed Cu-45S5 BG derived scaffolds are promising materials for applications in regenerative medicine including wound healing and bone tissue engineering."

In this work, two different deposition techniques have been employed for the coating of metallic substrates with Cu-doped BG.

The first employed technique has been the pulsed laser deposition (PLD), that allows to produce compact, homogeneous and rough thin films, in which the target stoichiometry is retained.

In order to increase the stability of bioceramics coatings in biological environment, polymer composite materials are increasingly used as materials with multiple functionalities, which provide structural and functional properties not achievable with a single components [129]. Since most of polymers, proteins and other complex materials are chemically and/or thermally modified or destroyed during the interaction with the high energy laser beam, the possibility to produce polymers-BG composite coating with pulsed laser technique is limited to matrix assisted pulsed laser ablation (MAPLE). MAPLE is an evolution of the PLD technique [130], which however requires a more complex experimental set-up than PLD.

As described in chapter 2, another powerful technique for the deposition of composite film coating for hard tissue implants is the electrophoretic deposition (EPD). Successful polymer-BG coated metal substrates have been produced [64,131–135]. In the second work of this chapter, EPD technique has been used for the deposition of composite zein/BG and Cu-doped BG.

5.1 Pulsed laser deposition and SBF assessment of Cu-doped BG

5.1.1 Introduction

In this work 45S5 Bioglass (BG) with 5 wt% of CuO content (BG_Cu) has been deposited by pulsed laser deposition technique. ICCD imagines have been acquired during the ablation process in order to study the plume expansion and estimate its velocity. The substrate temperature has been varied from room temperature (RT) to 500 °C in order to study its effect on the film's characteristics. The film deposited at RT has been chosen for the SBF soaking test. SBF, which stands for simulated body fluid, has an ion concentration very close to those of human blood plasma. The protocol for the preparation (described in section 3.4.3 d) has been refined by Kokubo et al. [63]. The soaking test in SBF has been accepted for the prediction of the in vivo bioactivity of a biomaterials suitable for hard tissue regeneration, according to the apatite formation on its surface [63,136].

At this purpose, various BG_Cu films have been deposited with PLD on Ti substrate. The as prepared samples have been soaked for different time, i.e. 3, 7,14 and 28 days. The apatite formation has been investigated with Raman spectroscopy, ADXRD and SEM-EDX techniques.

5.1.2 Results and discussion

a *Plasma characterization*

ICCD images acquired during the plasma ablation process, reported in Figure 5.1 (a), represent the time evolution of the ablated plume. The images have been registered each 100 ns, starting from the time when the laser pulse has struck the target surface, until 1.5 μs after that moment, when the plasma has become pretty cold. Since target-to-substrate distance affects the angular spread of the ablated materials [137]; the same set of images has been acquired with the substrate 2 cm distant from the target (Figure 5.1 (b)). By the observation of the plume expansion at different delays, it is possible to calculate the front velocity of the plume, which has been found to be 3.3 10^6 cm/s, as usual for nanosecond ablation process in vacuum [53]. The plume is completely detached from the target at 900 ns and at 1500 ns is almost completely cold. In addition, from the images it is possible to estimate the angular distribution of the plasma. Angular distribution of the ablated material can be fitted to a $\cos^n(\theta)$ [51], where n is parameter that takes into account the anisotropy of the plasma. In fact, in the case of a perfect spherical distribution n = 1, while as n increases the distribution increases along the direction normal to the target surface. n can be calculate by measuring the ratio between the major and the minor axes of the plasma plume (as described in section 2.1.1). In Figure 5.1 (a), related to the images acquired without substrate, it has been possible to measure a value of n= 1.65, at 300 ns after the laser pulse, that slightly diminished at higher delay. On the contrary, when the substrate has been positioned in front of the target (Figure 5.1 (b)), a faster progressive reduction of the ellipticity (decreasing of n) has been observed: during the first 300 ns, when the plasma is free to expand, n= 1.65; during its detachment from the target surface, n grows up to 1.26 (after 500 ns) and became 1.15 when the plasma is in contact with the substrate surface. At higher delay the effect of the plasma confinement exerted by the substrate presence is more evident.

No other emissions have been registered after the extinction of the first laser-induced plasma, similar to what has been observed for the HAp/IONPs plasma (section 4.1.2 c). Also the plume front velocity value of the two system are comparable. Therefore, similar morphology of the films can be predicted: a compact layer on the background, originated by the gas-phase condensation, overlapped by particles derived by the coalescence of molten droplets.

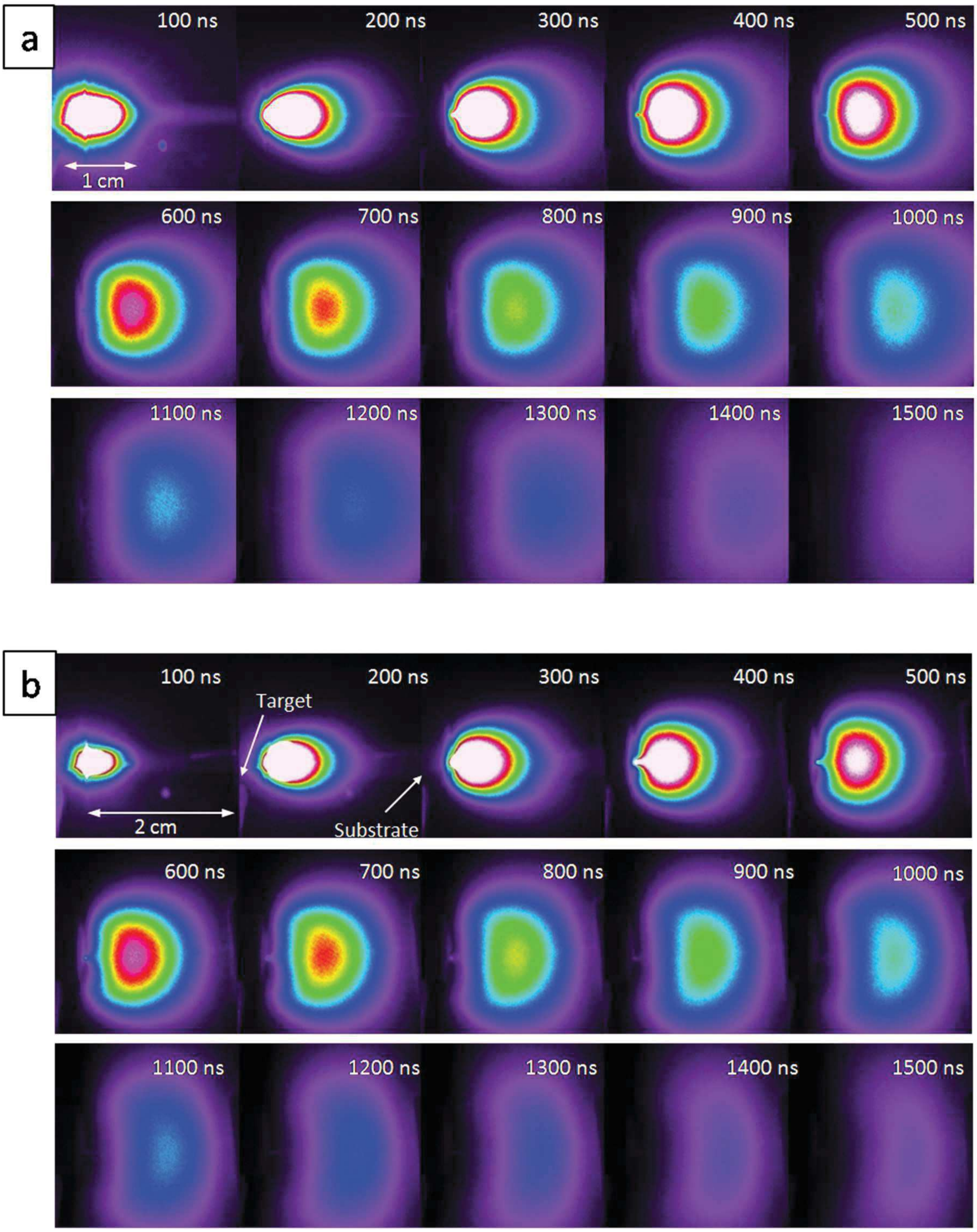

Figure 5.1: ICCD images of the plasma emission, acquired each 100 ns after the laser pulse, with a gate of 100 ns without (a) and with (b) substrate.

Due to the complexity of the material, OES has not been useful because the spectra interpretation has been difficult due to the presence of too many elements. In fact, for system with numerous species it is hard to distinguish and assign the detected peaks. As a matter of fact, OES is most widely used for monitoring the plasma of monatomic or diatomic simple system [114]. Nevertheless no marked differences are expected in the plasma behaviour between the bioceramic materials used in this thesis, thus plasma dynamic should by similar to the HAp/IONPs system, reported in section 4.1.2 c.

b *Physical-chemical characterization and bioactivity evaluation of the deposited films*

The wettability of the films has been evaluated by the measuring of the static contact angle of a water droplet. Wettability is an important condition for biomaterials in a biological system, because it influences protein attachment and cell adhesion and proliferation [126,138]. The ideal water contact angle for biomaterials surfaces should be in the range between 35° and 80°, accordingly the material should have moderately hydrophilic surface [64,139]. The results of contact angle measurements are reported in Figure 5.2. All the films have shown an improved wettability with respect to the substrate; the measured values fall within the desired range.

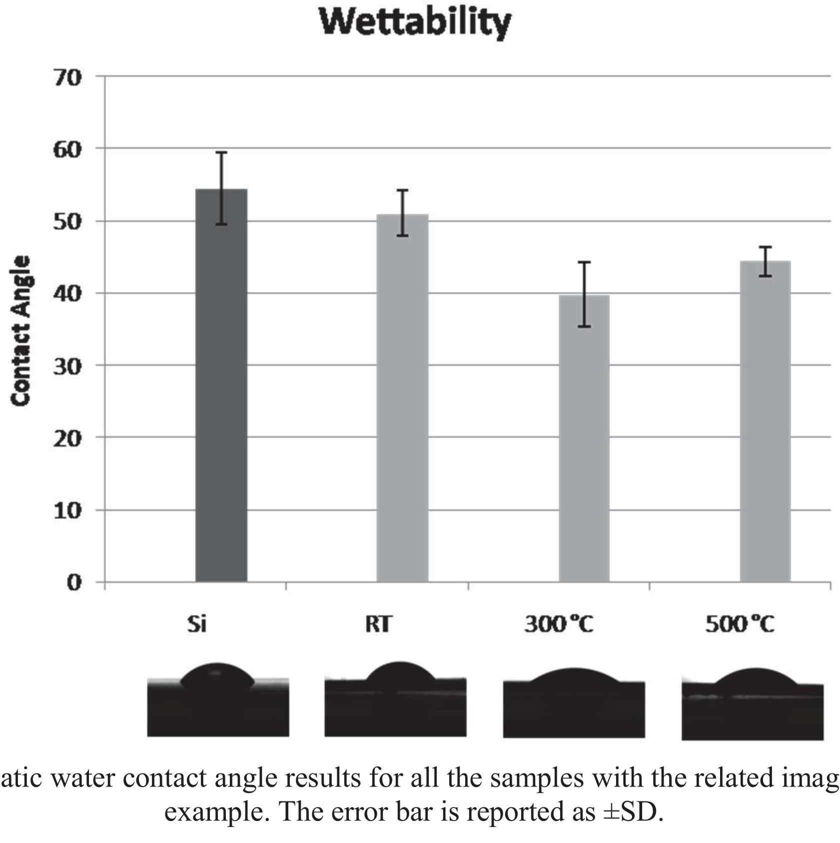

Figure 5.2: Static water contact angle results for all the samples with the related image, reported as example. The error bar is reported as ±SD.

In Figure 5.3(a) the ADXRD patterns of the target material and the film deposited at 500 °C are shown. The main crystalline phase in the target material is attributable to combeite, a calcium and sodium silicate, i.e. $Na_4Ca_4(Si_2O_3)_6$ (ICCD PDF 01-075-1687), typical of BG after a heat treatment [122,140]. The peak at 32.5° is associated to a silicorhenanite phase, which is isostructural to apatite, i.e. $Na_2Ca_4(PO_4)_2SiO_4$, whose crystallization is typically observed after heat treatments of BG [141–143]. In addition, the peak at 38.7 °, can be assigned to the most intense signal of CuO, associated to the plane (111) (ICCD PDF 01-080-1268). The film deposited at 500 °C have shown the four the most intense signals of combeite, while no peaks related to silicorhenanite or CuO have been detected. The films deposited at lower temperature have been found amorphous.

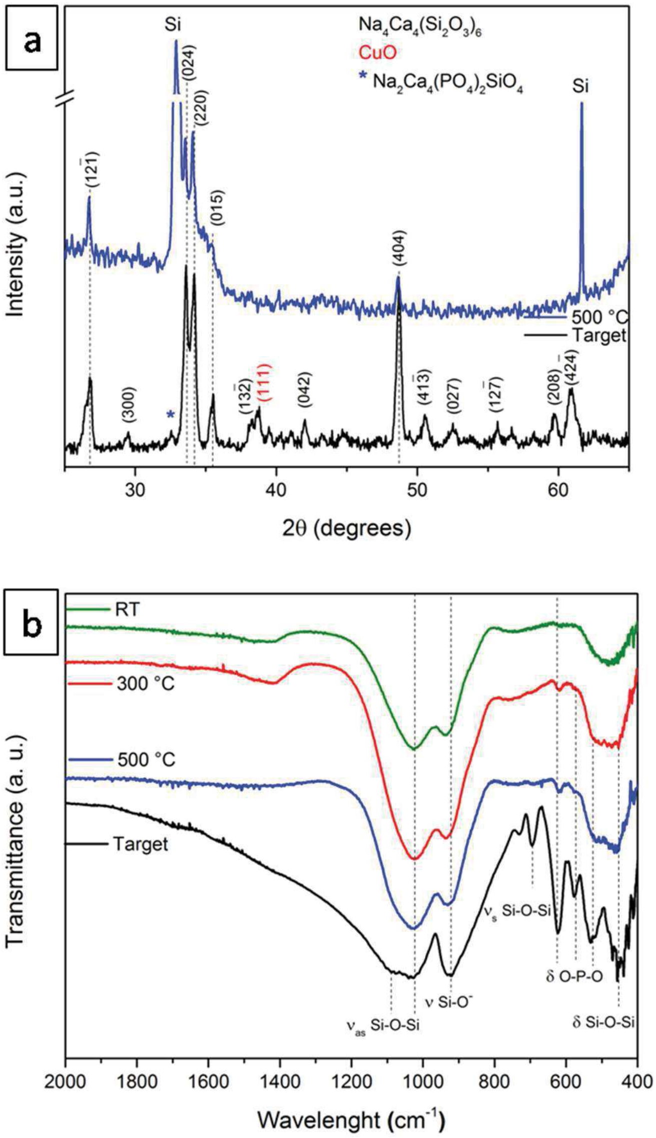

Figure 5.3: ADXRD patterns of the target material and the BG_Cu film deposited at 500 °C (a). FT-IR spectra of the target material and BG_Cu films deposited at RT, 300 °C and 500 °C.

The FT-IR target spectrum, in Figure 5.3 (b), has been shown the same signals of 45S5 BG without copper [122]. Signals at 622, 575 e 530 cm^{-1} of phosphate bending vibrations are attributable to the presence of a crystalline calcium phosphate (apatite-like), in agreement with the identification of the silicorhenanite phase in the XRD pattern; the appearance of these signals take places, in fact, during high temperature treatments 45S5 BG [141,143,144]. At 695 and 932 cm^{-1} the symmetrical stretching of silicate υ_sSi–O–Si and υ_sSi–O$^-$, respectively, have been detected. The presence of isolated tetrahedral Si, typical of crystalline silicates [122,141], have caused the splitting of the band around 1020 cm^{-1}, attributable to the asymmetrical stretching of silicate (υ_{as}Si–O–Si). No signals of CuO are detectable with this technique. The films' spectra, on the contrary, are characteristic of amorphous silicates, where it is possible to observe signals at 1022 cm^{-1}, 930 cm^{-1} and 480 cm^{-1}, attributed to Si–O–Si and Si–O$^-$ stretching modes and to the Si–O–Si bending mode, respectively [141]. In the spectra of the films deposited at higher temperature, especially the one obtained at 500 °C, the presence of silicorhenanite signals is starting to get visible. All the films deposited has shown pretty similar characteristics, for the easier preparation, the only observed difference has been the crystallinity of the films deposited at 500°C.

The tendency to crystallize is one of the major drawbacks of bioglasses. In fact, the presence of crystalline phases tends to retard the formation of the hydroxyapatite layer, hence glass becomes less bioactive in simulated body fluid [145,146]. It has been proved that the presence of phosphorus ions in bioglass affects the bioactivity: glasses containing a crystalline phosphate phase are less reactive than the ones containing phosphorus in solid solution, thus their dissolution behaviour and bioactivity decrease [142].

Therefore, RT deposited film has been chosen to test its in vitro bioactivity by the soaking in SBF. Its composition has been evaluated by EDX measurement. In Table 5.1 target and RT film compositions have been reported. The target composition has been almost retained in the film.

Table 5.1: SEM-EDX analysis results for BG_Cu target and RT film.

Oxides / Sample	Na_2O	SiO_2	P_2O_5	CaO	CuO
Target	20.7	40.0	9.9	22.4	7.0
RT film	21.5	39.3	5.6	27.6	6.0

All the oxides in wt %

The bioactivity of the film deposited on Ti at RT has been evaluated by the soaking of different samples for 3, 7,14 and 28 days. The apatite formation has been studied with a multi-techniques approach, by the employing of ADXRD, micro-Raman and SEM-EDX analysis.

The ADXRD spectra, reported in Figure 5.4 (a) reveal the amorphous character of the film before the soaking. A multicristalline apatite pattern has been detected only after 4 weeks of soaking. Moreover, since ADXRD is not a microscopic technique, it is difficult to detect the existence of small crystalline domains, which should be present on the coating surface even after 14 day of soaking, as Raman (Figure 5.4 (b)) and SEM (Figure 5.5 (g-h)) suggest.

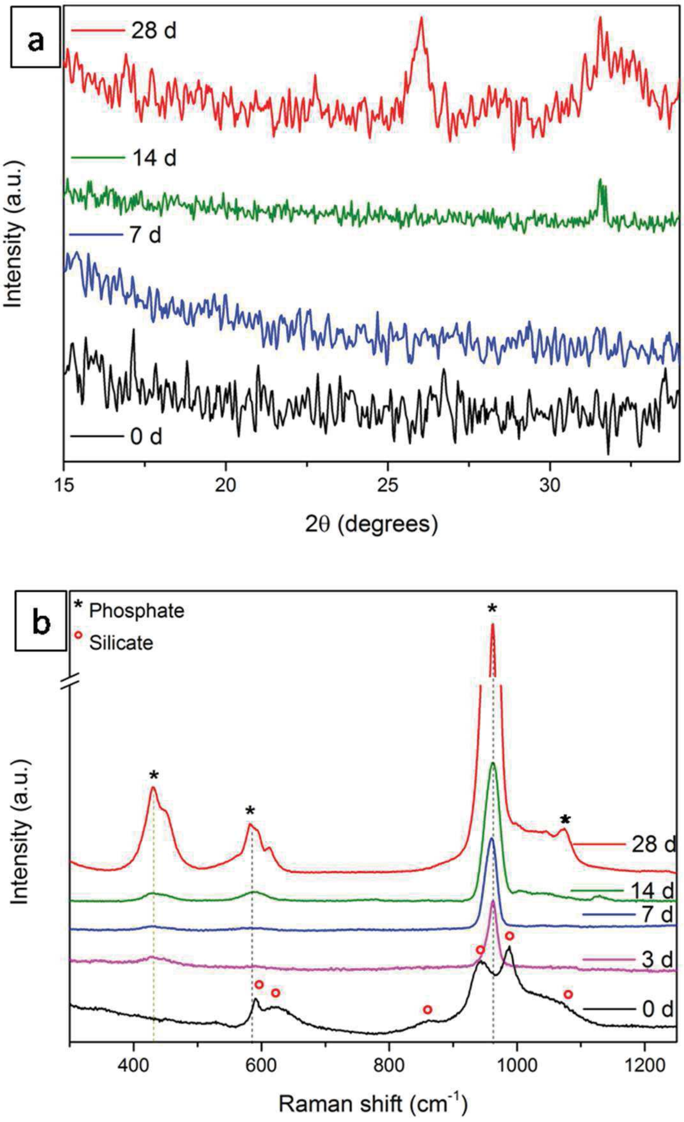

Figure 5.4: ADXRD patterns (a) and Raman spectra (b) of BG_Cu RT films after different immersion time points in SBF.

Table 5.2: Raman signals attributions.

Peaks Hydroxyapatite (cm^{-1})	**Assignment** [112]
429 (m), 451 (w)	ν_2 PO_4^{3-}
582 (w), 595 (w), 612 (vw)	ν_4 PO_4^{3-}
962 (s)	ν_1 PO_4^{3-}
1075 (vw)	ν_3 PO_4^{3-}
Peaks BG_Cu film (0 d) (cm^{-1})	**Assignment** [147,148]
592 (m)	ν_s SiOSi (crystal)
622(m)	SiOSi (r)
857 (w)	ν_s Si-O$^-$ (orthosilicates)
942 (s)	ν_s Si-O$^-$ (metasilicates)
988 (s)	ν_{as} SiOSi (crystal)
1070 (w)	ν_{as} SiO$^-$

where vw denotes: very weak, w: weak, m: medium and s: strong

Raman spectrum of the non-soaked samples shows the typical signals of mixed crystalline and amorphous silicate phases, the assignments are listed in Table 5.2 [147]. Whereas, apatite signals can be recognized still three days after the soaking in SBF.

In Figure 5.5 (a-b) the SEM images of the as prepared BG_Cu film is shown. It has been the typical morphology of bioceramics films deposited at room temperature by PLD in which elongated particles and droplets overlap a compact and uniform background, as predicted by the studying of the plasma expansion [67,108,109,149]. After only three days of soaking (Figure 5.5 (c-d)) the film's dissolution is evident. Cauliflower morphology characteristic of hydroxyapatite is visible after 14 days of soaking (Figure 5.5 (g-h)), while after 28 days (Figure 5.5 (i-l)) a second apatite crystallization has occurred.

The film's composition have been evaluated after the immersion tests by the means of EDX technique. It is possible to note the decreasing of the Si and Cu % with the increasing of the soaking time. While calcium and phosphorus, which are the principals components of the hydroxyapatite, have opposite trends. The synthetic hydroxyapatite is characterized by a specific Ca/P atomic ratio, which is 1.67. In the case of hydroxyapatite formed in physiological condition, the presence of bivalent cations, such as Na^{2+} or Mg^{2+}, induces defects in the crystalline structure by the substitution of Ca^{2+} in the hydroxyapatite apatite structure.

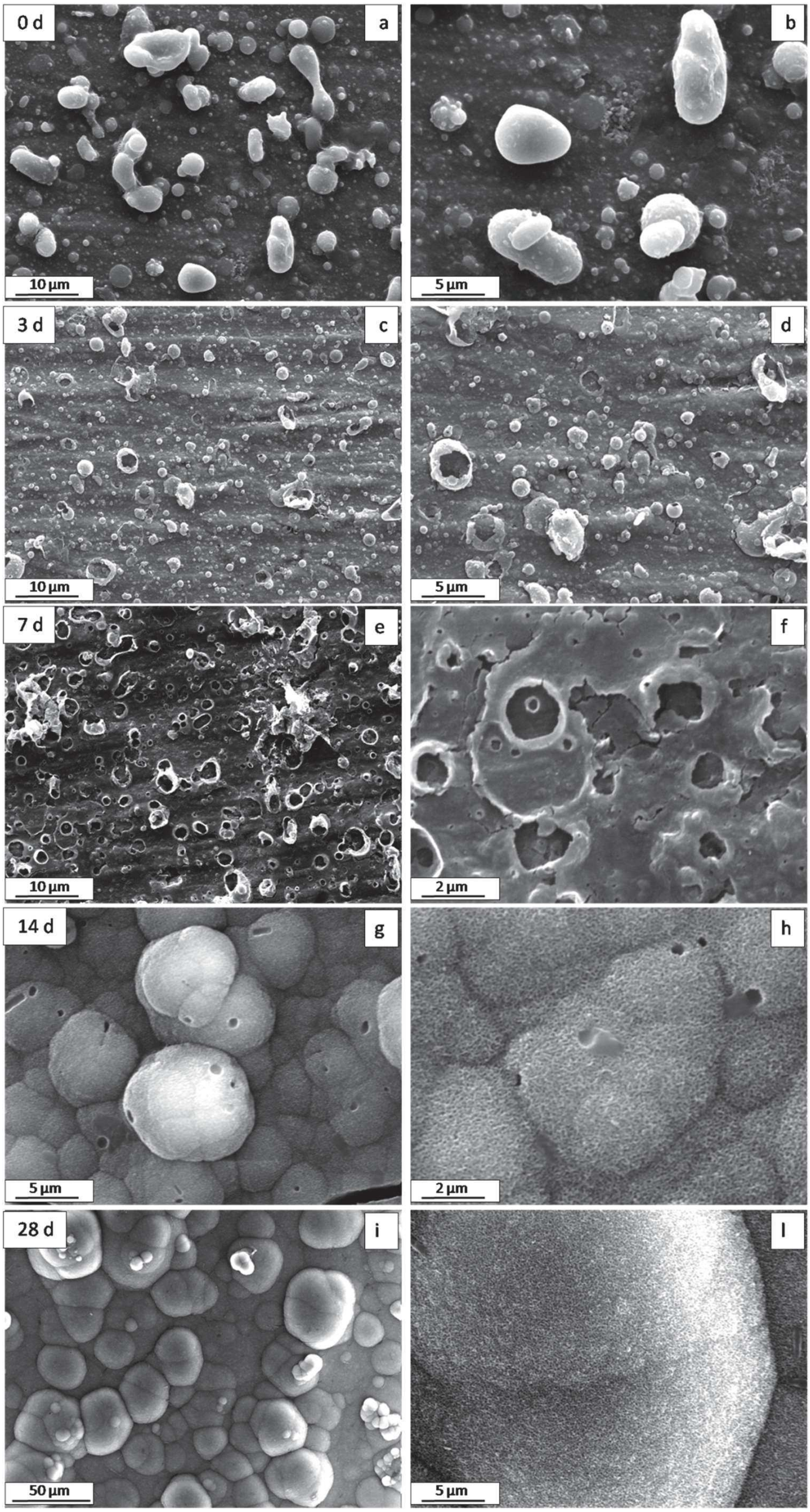

Figure 5.5: SEM images images collected upon BG_Cu coated Ti at two different magnifications, after different immersion time points in SBF: 0 d (a-b), 3 d (c-d), 7 d (e-f), 14 d (g-h) and 28 d (i-l).

Table 5.3: EDX measurements on the films deposited at RT, at different SBF soaking time points, all the data are reported in wt %, last column is an atomic ratio.

Element / Soak. d	Na	Mg	Si	P	Ca	Cu	(Na+Mg+Ca)/P
0 d	26.1	-	41.5	5.6	21.7	5.1	
3 d	3.7	-	12.5	38.7	40.0	5.1	
7 d	11.5	11.1	6.3	33.3	33.8	5.1	
14 d	3.3	1.8	1.8	37.4	55.5	<0.1	1.4
28 d	9.2	6.8	2.7	33.5	47.8	<0.1	1.7

The result is a multicrystalline apatite similar to the biological one [150,151]. Nevertheless, in this case the correct atomic ratio to be considered should be (Na+Mg+Ca)/P [152]. In the table it is possible to note a precipitous decreasing of the Si % together with a rapid increasing of Ca and P % after only 3 days of soaking in SBF. The (Na+Mg+Ca)/P atomic ratio, calculated for the samples where hydroxyapatite (more or less substituted) has been detected, gives a further confirmation of the bioactive behaviour of the BG_Cu film.

PLD technique has been revealed as a suitable method to prepare BG film coating for hard-tissue implant. For this purpose the physical-chemical properties and the in vitro bioactivity of the films have been found appropriate. Since the advantage of adding CuO in the BG composition lies in the improvement of antibacterial properties and angiogenic effect, such deposited films should be tested in contact with bacterial and osteoblast-like cell lines, respectively.

5.2 Electrophoretic deposition and SBF assessment of compostite zein/BG and /Cu-doped BG coatings

This work has been mostly carried out at the Institute of Biomaterials, Department of Materials Science and Engineering, University of Erlangen-Nuremberg, under the supervision of Prof. Dr.-Ing. habil. Aldo R. Boccaccini.

5.2.1 Introduction

There is a growing interest in the production of composite polymer/BG coatings for the improved hard-tissue related implant. Biological coatings containing bioceramics, biopolymers/biomolecules and their combinations have been investigated in order to improve the biocompatibility, the mechanical properties and the resistance to infections [64,132,153,154].

Usually, in order to improve the mechanical properties of the coating heat treatments are applied after the deposition process. This procedure, however, can causes the crystallization of the BG, with the diminution of its bioactivity. The use of polymers to prepare biomedical coatings can influence positively such properties, because it acts as a binder connecting the BG particles to the metallic substrate, with the advantage of low temperature processing and flexibility of coatings [135]. Among the room temperature method, Electrophoretic deposition (EPD) allows to obtain composite coating of various nature on substrate of different shape and dimension. In the field of hard tissue regeneration, great attention to bio-based polymer/BG films is devoting. Bio-based polymer are usually polysaccharides, proteins and/or lipids, generally biodegradable, non-toxic and edible materials [135]. Zein, the main storage protein of corn [155], belongs to this promising category of polymers. It has been largely used in the food industry as packaging material, thanks in part to its resistance to microbial attack [137,155]. In addition, zein biocompatibility, biodegradability and a various characteristics, which depend on its physical-chemical properties, make the material attractive for application in the biomedical field either as drug carrier or as material for tissue engineering [156]. Zein belongs to the class of prolamines, proteins peculiar of cereals. It is particularly rich in glutamic acid (21–26%), leucine (20%), proline (10%) and alanine (10%). The deficiency in essential amino acids such as tryptophane and lysine causes the low nutritional value of zein. Moreover the high amount of non-polar amino acid residues and deficiency in basic and acid amino acids is responsible for the solubility behaviour of zein. In fact it is insoluble in water but owns good solubility in aqueous-alcohol solution. Thanks to its numerous side-chain amino acid arrangements, zein can be processed in form of film. Zein films are generally tough, glossy, biodegradable, safe for internal human use, resistant to microbial attack and can entrap particles [156].

In this context, zein has been chosen for the electrophoretic deposition of composite film with BG and Cu-doped BG on stainless steel (SS) substrates. In this work the experimental parameters have been optimized in term of EPD suspension composition and deposition condition (i.e. deposition time and voltage). As regards the suspension composition, the percentage of water, ethanol and zein together with the BG contents have been varied. Glycerol has been added as plasticizer [157]. Although the optimum has been not yet reached, samples prepared in the best deposition condition have been characterized from a physical-chemical and bioactivity point of view.

5.2.2 Results and discussion

a *Zein, BG and BG-2.5 Cu powders characterization*

For a better characterization of the deposited films, a preliminary characterization of the starting powders (zein, BG and BG-2.5 Cu) has been carried out. In Figure 5.6 (a) the Raman spectra of zein powder is shown. The detected signals, which overlap a fluorescence band, intrinsically arising from foodstuffs, are attributable to the presence of cystine, tyrosine, tryptophan, phenylalanine as well as aliphatic residues and amides, as summarised in the Table 5.4 [137]. Whereas no difference can be detected between the spectra of BG and BG_Cu powders (Figure 5.6 (a)); both of them show typical signals of amorphous glass at 623, 945 and 1081 cm-1 the rocking vibrational mode and two stretching mode of silicate with non bonding oxygen, respectively, have been detected. Similar information has been obtained from the FT-IR (Figure 5.6 (b)), where the silicate bending has been found at 445 cm^{-1}, and the stretching modes at 731, 910 and 1003 cm^{-1}, such spectra is typical of 45S5 Bioglass, with or without copper [122]. Their amorphous character has been confirmed by the means of ADXRD analysis (not shown), where only a band in the range 25-40 2θ°, typical of a glassy material has been detected.

FT-IR spectrum of zein is characterized by four distinctive bands of proteins. The band corresponding to the stretching of the N-H and O-H bonds is between 3000 and 3500 cm^{-1}. The signal at 1630 cm^{-1} corresponds to the stretching of the carbonyl (C=O) of amide (amide I). The band at 1523 cm^{-1} is related to the angular deformation vibrations of the N-H bond (amide II). The last signal at 1231 cm^{-1} is due to the axial deformation vibrations of the C-N bond [158,159].

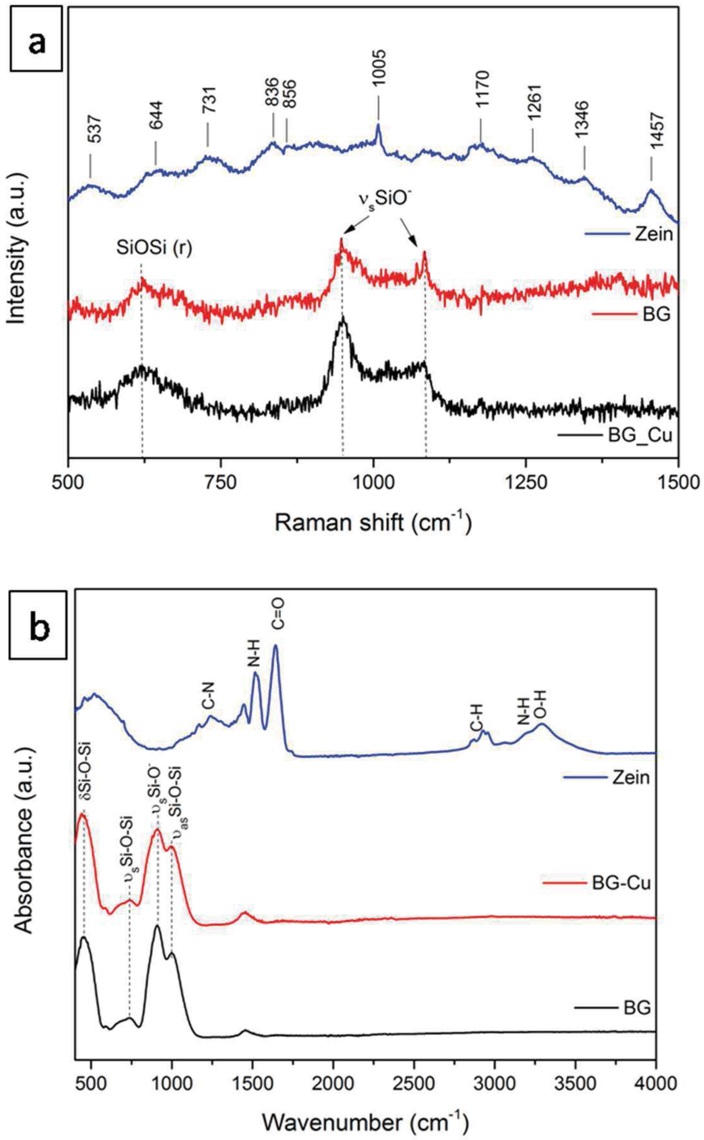

Figure 5.6: Raman (a) and FT-IR (b) of the starting powders.

Table 5.4: Raman signals attributions of zein [137].

Peaks position (cm^{-1})	**Assignment**
537	S-S stretching (cystine)
644 and **731**	C-S stretching (cystine)
836/856	Fermi resonance between ring (tyrosine)
1005	Ring breath (phenylalanine)
1261	N-H in plane bending and C-N stretching (amide III)
1346	indole ring (tryptophan)
1457	C-H bending (aliphatic residues)

b *Optimization of EPD parameters*

Several attempts have been made in order to obtain an homogeneous film with good adhesion and good wettability, since zein is basically hydrophobic. In addition, during the EPD of aqueous suspension, if water has the advantages of high dielectric constant (which allows to work at lower potential), its undesired electrolysis occurs [160]. The electrolysis of water results in the evolution of gas at the electrodes, the incorporation of gas bubbles into the deposit causes low deposit quality: coatings with holes, reduced adherence to the substrate and low homogeneity. In order to limit the electrolysis of water, the suspension has been sonicated before each EPD experiment, and deposition time and applied voltage have been kept low. In order to optimized the anodic deposition of zein/BG composite coatings, the deposition time has been changed from 30 sec to 15 min and the applied voltage has been varied in the range of 5-30 V. Since the isoelectric point falls at the pH of 6.2, the pH suspension has been kept at 8.5-9 in order to ensure the anodic deposition.

The evaluation of the films quality during the optimization steps has been carried out, after a visually inspection, by the observation of the film morphology with SEM technique and the evaluation of the wettability by static water contact angle measurements.

First of all, the films deposited for more than 1 min and 30 sec have been excluded because the morphology has been visually inhomogeneous, the same has been done for films deposited with a voltage higher then 15V. Once chosen to work in a range between 5-15 V, depositing for non more than 1 min and 30 sec, the relative percentage of zein, H_2O and EtOH have been slightly varied. For instance, in figure 5.7 SEM images of a film deposited for 1 min at 10 V (a-b) and 1 min at 5 V (c) are shown. The corresponding suspension compositions are listed in Table 5.5.

Table 5.5: EPD suspension compositions related to the samples reported in Figure 5.7.

Composition (wt %)	(a)	(b)-(c)
H_2O	25	25
EtOH	65	60
Zein	10	10
Glycerol	-	5

To all the suspension 20 g/l of BG has been added

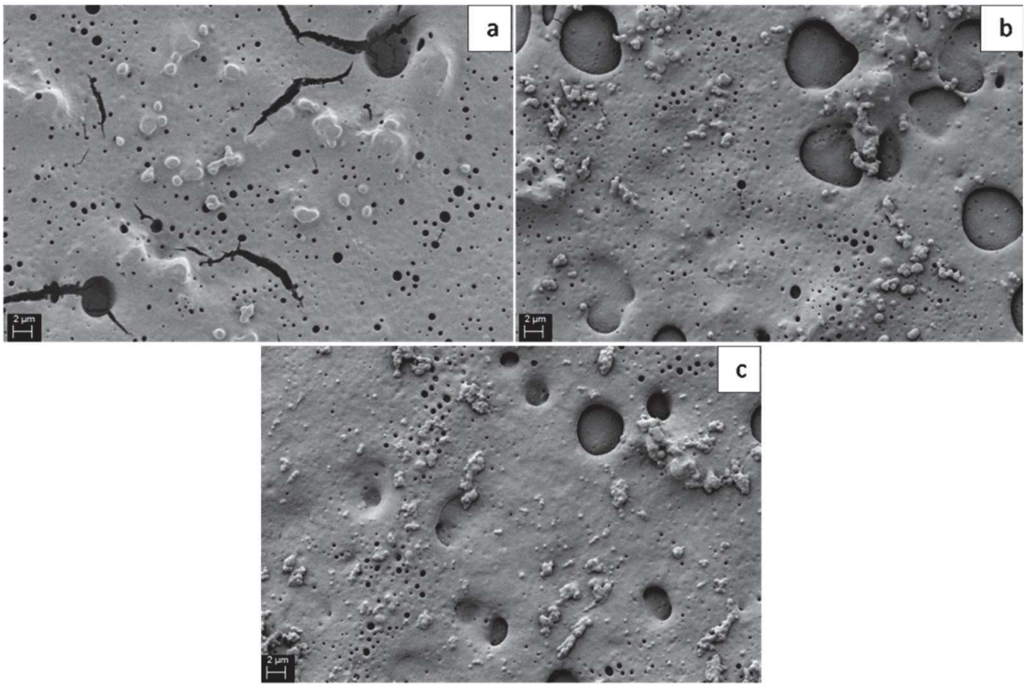

Figure 5.7: SEM images of a film deposited for 1 min at 10 V (a-b) and 1 min at 5 V (c).

The presence of cracks on the film surface in Figure 5.7 (a) has suggested to add a plasticizer agent, like glycerol. In fact, as is possible to observe in Figure 5.7 (b), the films deposited in the same condition has shown no cracks thanks to the adding of glycerol. However the presence of big holes due to the glass bubbles has been limited by the deposition at lower applied voltage, i.e 5 V, as visible in the last SEM image (Figure 5.7 (c)). Further improvements have been made and, although the optimal conditions have been not yet found, the chosen suspension composition has been: H_2O–25%, EtOH–66%, glycerol–3%, zein–6%, all in wt%. Films without BG have also been deposited in order to understand the role of zein on the coatings features. The as prepared samples have been characterized and their bioactivity in vitro assessment has been carried out by the soaking in SBF for different time points (i.e. 1, 3, 7 and 14 days). In Table 5.6 the samples chosen to be tested are reported in relation with the bioglass content and the deposition condition.

Table 5.6: Deposition condition of the chosen samples.

Sample name	BG amount (g/l)	Deposition time (min)	Applied voltage (V)
NOBG	-	1	5
20 BG	20 of BG	1	5
50 BG	50 of BG	1	5
20 BG_Cu	20 of Cu-doped BG	1	5
50 BG_Cu	50 of Cu-doped BG	1	5

c *Physical-chemical characterization and bioactivity evaluation of the deposited films*

A visually inspection of the films surface has suggested a film homogeneity, as is visible in the picuters reported in Figure 5.8. A qualitative evaluation of the adhesion between the coating and the substrate has been carried out by the means of cycled bending tests. This test consists in the bending of the coated substrate around the axis (180°) until the coated surface became parallel to the other half of the substrate, then the substrate is bending back in the original position; the operation is repeated for 5 times. The pictures of the film before and after the bending test are shown in Figure 5.8 and images recorded by the means of an optical microscope are shown in Figure 5.9. All the coatings have exhibited a compact and uniform surface with a few micro-cracks and pillings (shown by arrows in the figure) on the edge of the coating. This is an indication of good flexibility and adhesion of the coatings.

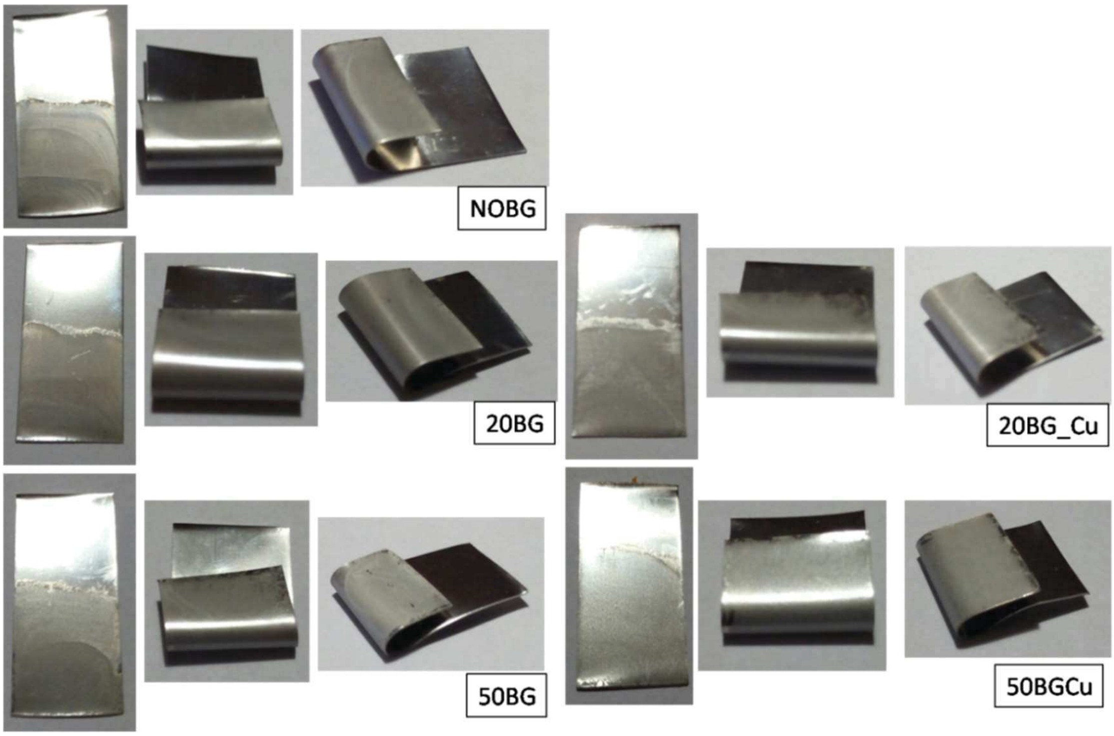

Figure 5.8: Pictures of the films before and after the bending test.

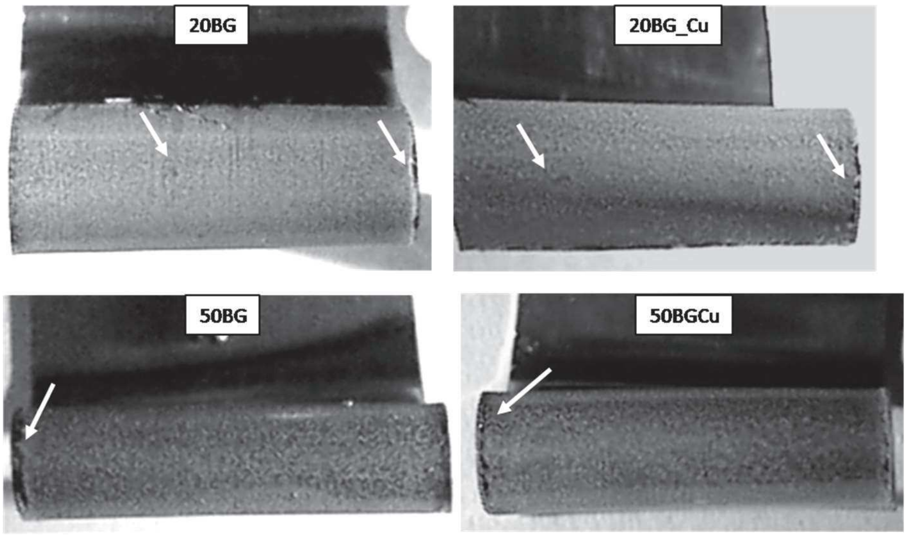

Figure 5.9: Optical images of the bent coated substrate.

The films' wettability has been evaluated by the measuring of the static water contact angle. As visible in Figure 5.10, all the films have shown an improved wettability with respect to the substrate. The measured values fall within the proper range, which is for biomaterials surfaces between 35° and 80°, accordingly the material should have moderately hydrophilic surface [64,139]. Only the sample 50 BG_Cu has shown a too high wettability. On the contrary, the NOBG sample has revealed that BG presence in the film is fundamental not only for the bioactivity, but also for the surface wettability.

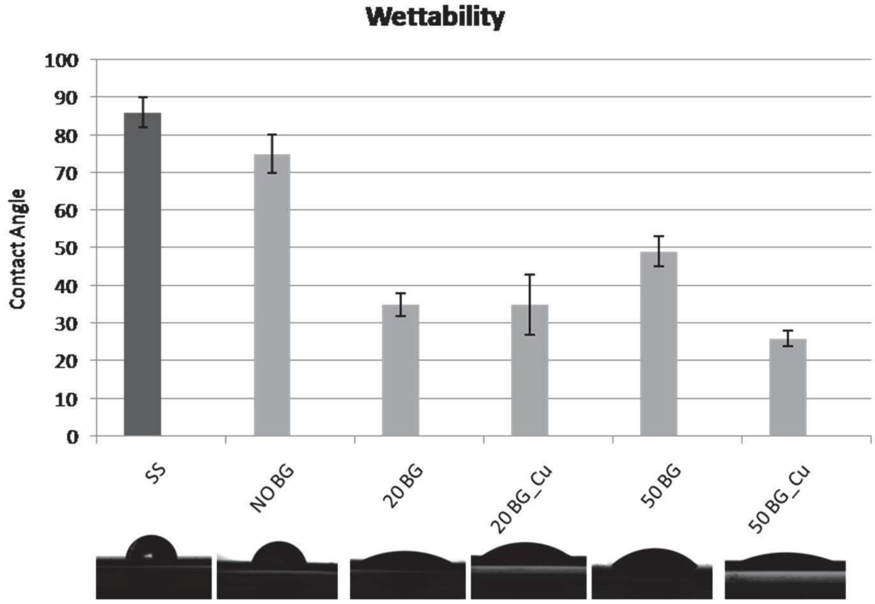

Figure 5.10: Static water contact angle results for all the samples with the related image, reported as example. The error bar is reported as ±SD.

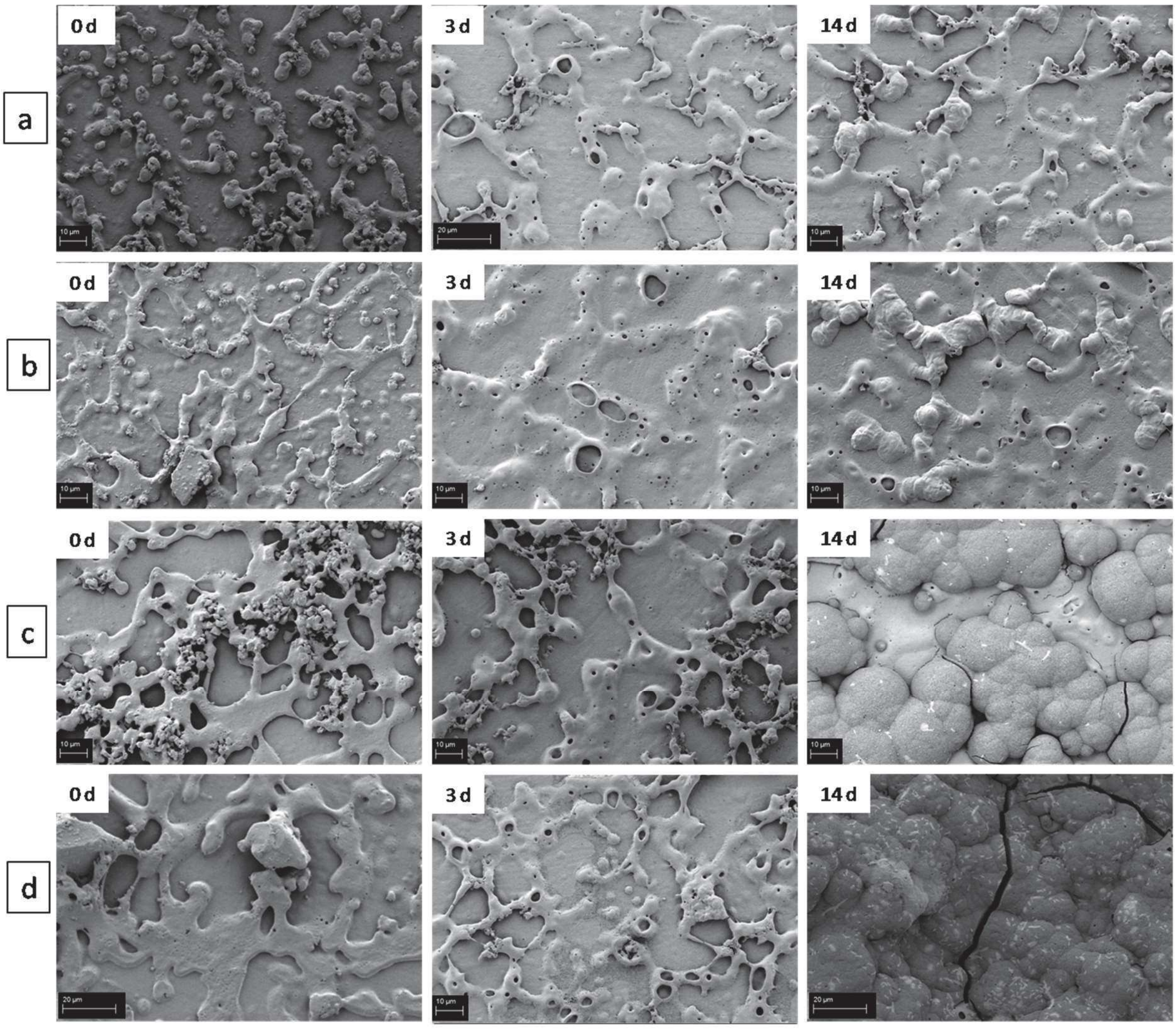

Figure 5.11: SEM images collected upon 20BG (a), 20 BG_Cu (b), 50 BG (c) and 50BG_Cu (d) films after different immersion time points in SBF.

The films' properties have been studied in relation to their in vitro bioactivity. The films' morphology, before the soaking and after different time points, has been evaluated by the means of SEM technique (Figure 5.11). All the films deposited, before the SBF soaking (0 d), have shown a compact background with no holes due to the electrolysis of water; however a not fully polymerization of zein is observable. Film morphology can be improved by the using of smaller nanometric particles. BG particles have been entrapped in the zein matrix, which slowed down the BG bioactivity. In fact typical cauliflower morphology of apatite has been observable after 14 days of immersion only on the deposits with a higher content of bioglass (Figure 5.11 (c-d)).

Nevertheless, after 3 days of soaking the degradation of zein is visible for all the samples, that allows the BG ion release and the formation of calcium phosphate at the boundary between the coatings and the SBF. The SEM image, collected at higher magnification on the sample 50BG, is reported in Figure 5.12. In this image the zein matrix degradation is evident as well as the apatite crystallization. It is necessary to underline, however, that zein alone is not bioactive. In fact a parallel experiment carried out on a film deposited without BG (sample NOBG) has been shown a really slow degradation zein in SBF, together with the complete absence of apatite crystallization. For instance a SEM image of the NOBG is reported in Figure 5.13. The image has been registered after 14 day of soaking in SBF. The zein degradation, after 14 days of SBF soaking, has proved less than the degradation observed after 3 days of soaking of all the deposits with bioglass. This is not surprising since zein coatings are normally used as food packaging thanks to its hydrophobic character [137,155]. This is consistent with the NOBG rather hydrophobicity revealed by the means of contact angle measurements (Figure 5.10).

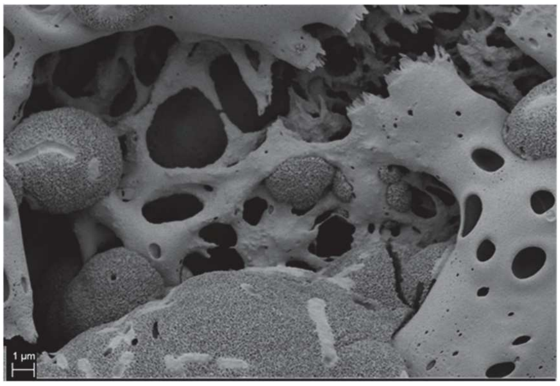

Figure 5.12: SEM image of a detail of zein degradation and hydroxyapatite growth.

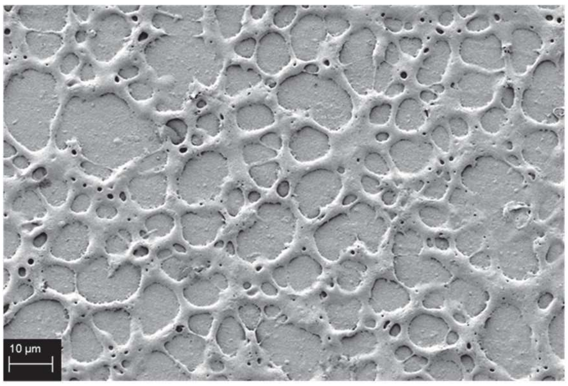

Figure 5.13: SEM image of NOBG surface after 14 days of immersion in SBF.

Table 5.7: Ca/P and (Ca+Na+Mg)/P atomic ratios measured with EDX analysis.

	20 BG	20BG_Cu	50 BG	50 BG_Cu
Ca/P	1.12	1.13	1.40	1.30
(Ca+Na+Mg)/P	1.24	1.25	1.52	1.53

In the Table 5.7 the Ca/P ratio, calculated after 14 days of SBF soaking, is reported. It has been calculated by the means of EDX analysis. As anticipated in the section 5.1 b, the synthetic hydroxyapatite is characterized by a specific Ca/P atomic ratio, which is 1.67. However, when hydroxyapatite crystallizes in physiological environment, bivalent cations, such as Na^{2+} or Mg^{2+}, that are present in the fluid, substitute Ca^{2+} in the hydroxyapatite apatite structure, inducing defects in the crystalline structure. This is the reason why the measured Ca/P ratio resulted minor of the expected one. In this case also the other bivalent cations should be considered [150,151]. The so considered ratio has been slightly lower than the predicted, probably due to the presence of calcium phosphates, other than hydroxiapatite, not yet crystallized in apatite phase.

The soaked samples have been characterized also by the means of ADXRD, Raman and FT-IR spectroscopic techniques. ADXRD analysis (Figure 5.14) has revealed the presence of a multicrystalline apatite formation after 7 days of soaking in SBF. 20 BG has been the only sample showing no crystalline peaks after 7 days of soaking.

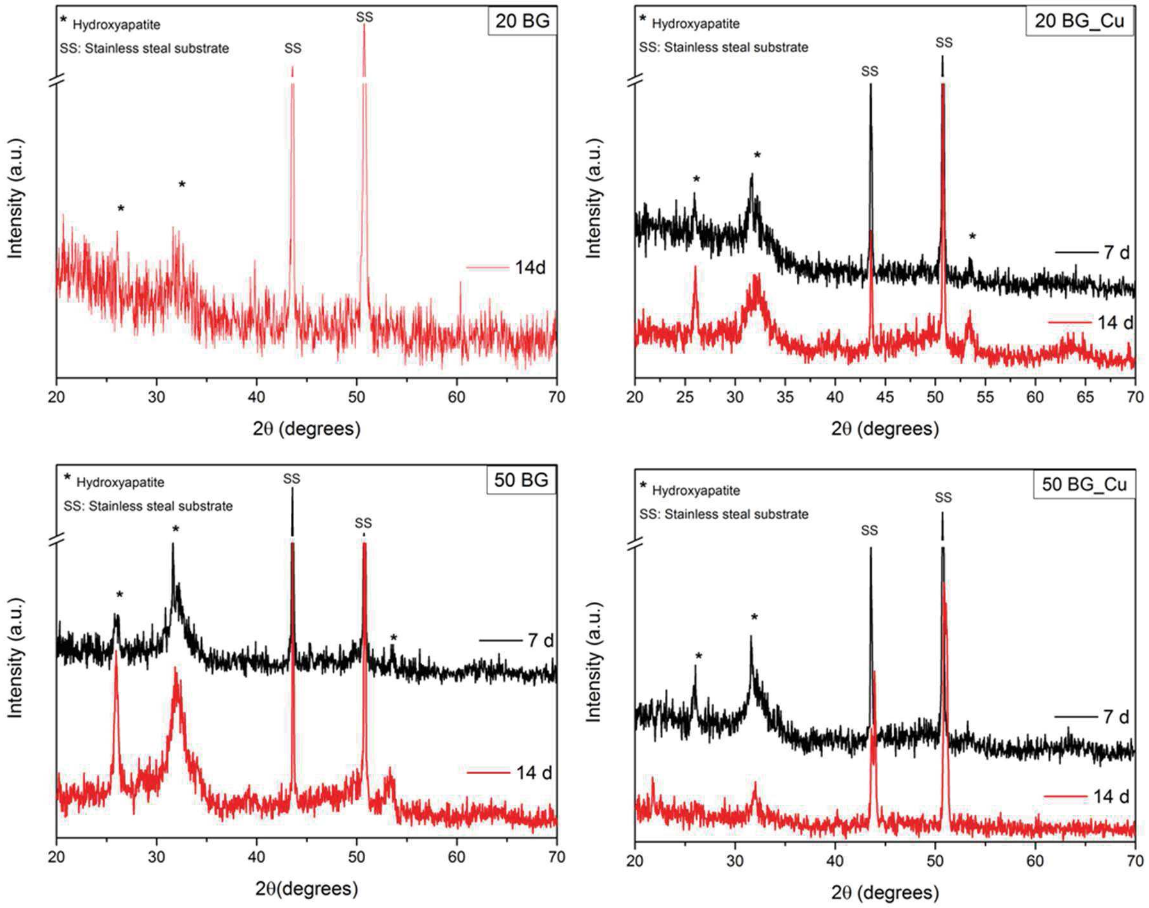

Figure 5.14: ADXRD patterns of 20BG, 20 BG_Cu, 50 BG and 50BG_Cu films after different immersion time points in SBF.

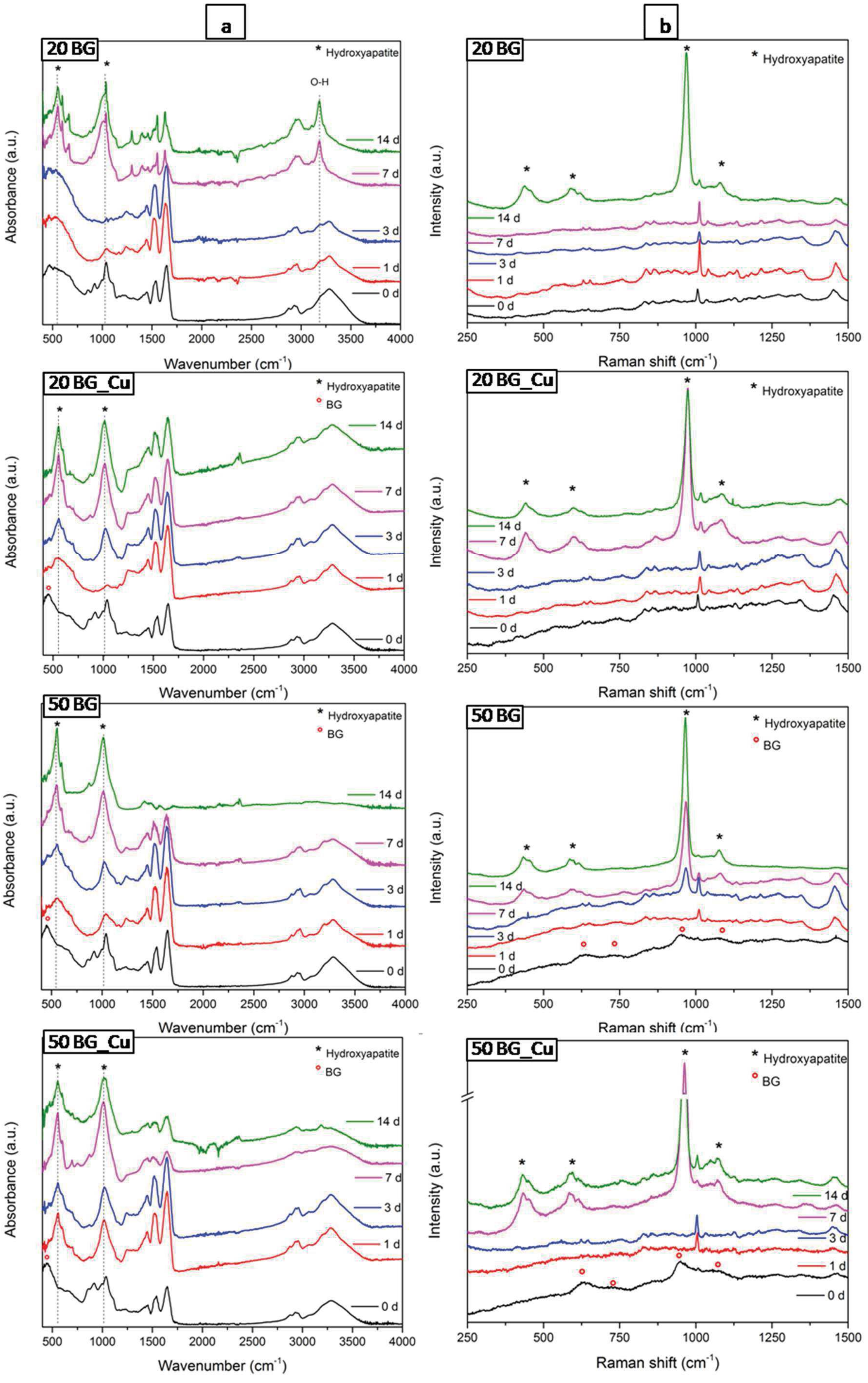

Figure 5.15: FT-IR (a) and Raman (b) spectra of 20BG, 20 BG_Cu, 50 BG and 50BG_Cu films after different immersion time points in SBF.

In Figure 5.15 a comparison between FT-IR (a) and Raman (b) spectra registered on all the sample is shown. The two technique have furnished similar results; however with Raman spectroscopy the signals of BG and BG_Cu before and hydroxyapatite after the immersion assessment have been easier to distinguish from the signals related to zein and glycerol with respect to FT-IR analysis.

As regards the FT-IR spectra, all the samples have shown typical zein peaks (see Figure 5.6 (b)). All the spectra of deposits before the immersion in SBF (0 d) have revealed an additional group of signals (920, 993, 1035 cm^{-1}), related to the presence of glycerol. A weak contribution of BG silicate bending is also visible, on the contrary the signals relate to stretching mode are covered by that related to glycerol.

After 3 days of soaking all the samples, except 20 BG, presents FT-IR signals of phosphate, and after 14 days all of them presents typical apatite vibration at 547, 603 and 663 1015 cm^{-1} (ν_{4c}, ν_{4b} and ν_{4a} PO_4^{3-}, respectively), of crystalline phosphate bending mode, and at 1015 cm^{-1}, related to antisymmetrical stretching mode (ν_3 PO_4^{3-}) [112].

Raman signals of hydroxyapatite have been instead visible after 7 days of soaking in SBF, except for the 20 BG sample, on which apatite peaks has been detected after 14 days. Raman results are exactly the same of that obtained by ADXRD technique. All the attributions are reported in Table 5.8.

Table 5.8: Raman signals attributions.

Peaks Hydroxyapatite (cm^{-1})	**Assignment** [112]
439 (m), 461 (w)	ν_2 PO_4^{3-}
589 (w), 602 (w), 623 (vw)	ν_4 PO_4^{3-}
969 (s)	ν_1 PO_4^{3-}
1081 (vw)	ν_3 PO_4^{3-}
Peaks BG and BG_Cu films (0 d) (cm^{-1})	**Assignment** [147,148]
630 (m)	SiOSi (r)
947 (s)	ν_s Si-O^-
1078 (w)	ν_{as} SiO^-

where vw denotes: very weak, w: weak, m: medium and s: strong

Electrophoretic deposition has proved to be a functional technique for the production of composite zein/BG coating. Their bioactivity, mainly for the deposits with higher amount of bioglass, has demonstrated to be suitable for hard-tissue implants applications. Since both zein and Cu-doped BG should have antimicrobial properties [118,119,124,126,137,155], certainly such properties have to be tested, as in the case of the BG_Cu films deposited by PLD.

CHAPTER 6

Coatings based on glass-ceramics

Bone regeneration involves by two process bone-forming, regulated by osteoblasts, and bone-remodelling, regulated by osteoclasts. These processes require the action of numerous systematic and local agents, such as proteins, receptors, growth factors, hormones. A number of metal ions is involved in bone metabolism inducing and taking part to the biological apatite formation and also acting as enzyme co-factors [62,66]. Researches in the field of hard tissue regeneration are attempting to create the best bioactive ceramic by the introducing of different ions, especially metallic ions, in calcium phosphate, glasses and glass-ceramic composition. The introducing of specific ions not only may improve the biological response, but also can give better physical-chemical and mechanical properties to the materials [31].

In the last two decades a glass ceramics developed at ISTEC_CNR (Faenza, Italy), named RKKP (stands for Ravaglioli, Krajewski, Kirsch and Piancastelli) is drawing the attention of many researchers. RKKP is a bioactive glass-ceramics with the following composition: SiO_2 – 43.68, β-$Ca_3(PO_4)_2$ – 24.00, CaO – 18.40, CaF_2 – 4.92, Na_2O – 4.53, MgO – 2.78, K_2O – 0.19, Ta_2O_5 – 1.00, La_2O_3 – 0.50 (all inwt%) [65]. It was obtained by the adding of network formers La^{3+} and Ta^{5+} to the composition of AP40, which contribute to stabilize the molecular network; in particular, La^{3+} improves the resistance of the glass towards alkalis, whereas Ta^{5+} allows the reduction of the defects inside the glassy body [66,161]. In addition, Z-potential measurements and in vitro tests of proteins absorption demonstrated that the presence of Ta_2O_5 and La_2O_3 in the composition has a crucial role in the biological activity [69,162].

In literature RKKP is reported as a great potential glass-ceramics; its good performances of biological interaction, including high bioactivity and osteoconduction, have been largely proved [69,161–163]; furthermore, in vivo studies revealed also its capability to bond healthy as well as osteopenic bone [164].

RKKP, like all the glass-ceramics, can be produced by melting or sol-gel procedures [165]. Rau et al. [65] studied two series of RKKP film deposited on Ti substrate with ns-PLD technique. They used two different RKKP target, one produced by melting and one by sol-gel route, with the aim to compare the physical-chemical and mechanical properties of the film obtained. They found the better deposition condition (i. e. 12 Jcm^{-2} was the fluence, 500 °C the deposition temperature and 2 cm the distance target-substrate). Moreover there were no significant differences in the use of the target. Successively, they tested the biocompatibility of the films obtained from the sol-gel prepared target [166]. They concluded with the sentence: " *Through our tests it was finally demonstrated that the RKKP coated Ti supports are not only cell-friendly substrates for the CaCo-2 cells adhesion, growth and differentiation, but also represent a new potential cell delivery system that may be used in tissue engineering applications and in the future regenerative medicine protocols.*"

Concerning what was said so far, RKKP has been chosen as starting material for the current works, briefly introduced below.

- RKKP has been deposited again on Ti substrate by the means of PLD in order to test its capability as stem cells delivery system:

(Published: M. Ledda. M., Fosca, A. De Bonis, M. Curcio, R. Teghil, M.G. Lolli, A. De Stefanis, R. Marchese, J.V. Rau, A. Lisi, *Placenta Derived Mesenchymal Stem Cells Hosted on RKKP Glass-Ceramic: A Tissue Engineering Strategy for Bone Regenerative Medicine Applications*, BioMed Research International, (2016) 1-11.) [67].

- It has been deposited on Mg-Ca substrate with the aim to produce a suitable solution for the production of resorbable implant with improved corrosion resistance.

(Published: J.V. Rau, I. Antoniac, M. Fosca, A. De Bonis, A.I.Blajan, C. Cotrut, V.Graziani, M.Curcio, A. Cricenti, M. Niculescu, M. Ortenzi, R. Teghil, *Glass-ceramic coated Mg-Ca alloys for biomedical implant applications*, Materials Science and Engineering C 64 (2016) 362–369.) [149].

- In order to improve the mechanical properties of the film, fullerite powder has been added in the RKKP target and the mixture was used to produce composite thin films.

(Published: M. Curcio, A. De Bonis, M. Fosca, A. Santagata, R. Teghil, J. V. Rau, *Pulsed laser-deposited composite carbon–glass–ceramic films with improved hardness*, Journal of Materials Science 52 (2017) 9140-9150.) [109].

- A further metallic ion with biological role, manganese, has been added in RKKP composition for the improving of the biological performances. The biocompatibility of RKKP_Mn starting powder has been tested and the in vitro bioactivity of the deposited films has been proved.

In the following sections the individual works will be reported separately.

6.1 RKKP coated Ti as support for Mesenchymal Stem Cells delivery

This work has been conducted in collaboration with the IFT-CNR (Rome, Italy), where the biological tests have been carried out; the stem cells have been furnished by S. Peter Hospital (Rome, Italy).

6.1.1 Introduction

Mesenchimal stem cells (MSCs) belong to the category of multipotent cells since they are able to differentiate to different type of mesenchymal cells, such as osteoclasts, osteoblasts, chondrocytes, adipocytes. Thanks to the differentiation capability and the ability to secrete trophic factors for the inducing of the tissue healing, MSCs are very interesting and promising source for tissue regeneration [167]. Among MSCs human amniotic stromal cells (hAMSCs), derived from the amniotic fetal membrane of human term placenta, have generated great interest, not only for their immunomodulatory and proregenerative properties but also for the ethical acceptance, since their isolation is not invasive for the donor [168]. Unfortunately, the applications of MSCs is limited so far because after their implantation patients have to be treated with huge doses of growth factors, that increases the side effects. Furthermore, the protocol for their usage for hard tissue regeneration requires the injection of the cells suspended in a buffer; however this practice has not led to a satisfactory engraftment. In Order to improve their engraftment rate, the use of supporting matrix has been suggested [169].
In this work RKKP bioactive glass-ceramic has been used to coat titanium substrate by the means of PLD technique. As described in the section 1.3.1, titanium is largely used for hard tissue replace thanks to its biocompatible and mechanical properties; however Ti is subjected to oxidation in biological fluid and fibrous tissue encapsulation. For these reasons, the coating with thin film of bioactive materials like RKKP improve the implant fixation. All the films have been deposited with a doubled Nd:YAG source at 12 J/cm^2 of laser fluence; with substrate positioned at 2 cm from the target; deposition time of 2 h,

substrate temperature of 500 °C.

The crystalline phases of the film have been studied by the means of EDXRD; while the EDX gives information of the elemental composition. Surface features have been investigated by SEM and AFM microscopic technique.

The aim of this work was to test the potentiality of RKKP coated Ti substrate as supporting delivery system of hAMScs for hard tissue implant application. Therefore their effects on hAMScs growth, proliferation, metabolic activity, cell morphology, cycle phase distribution, and mRNA expressions of key genes including osteogenic differentiation markers have been tested.

6.1.2 Results and discussion

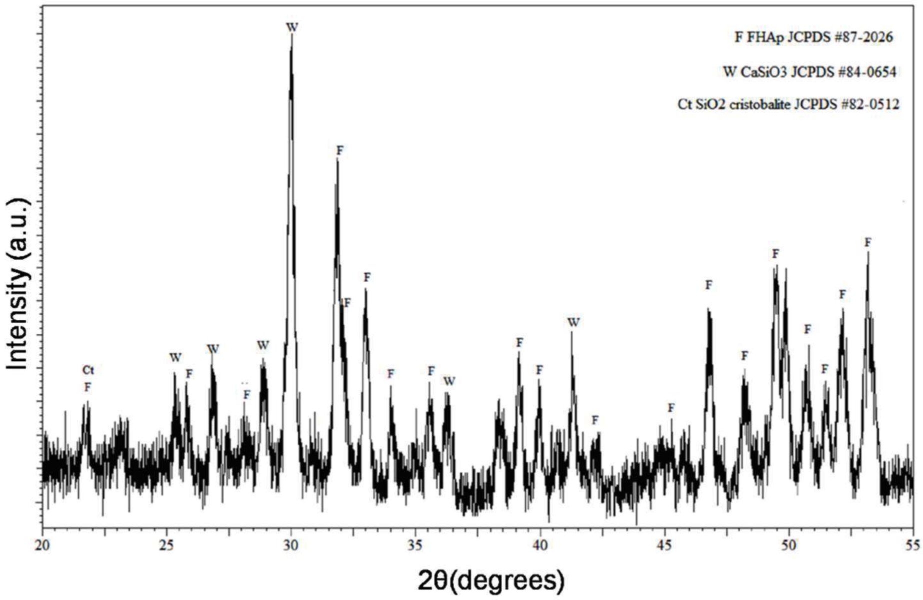

Figure 6.1: ADXRD pattern of RKKP target material, prepared by sol-gel synthesis.

The ADXRD pattern of the RKKP target material, reported in Figure 6.1, prepared by sol-gel route is mainly composed of wollastonite ($CaSiO_3$, wollastonite-1A, JCPDS #84-0654) and fluoroapatite (FHAp, $Ca_5(PO_4)_3F$, JCPDS #87-2026); moreover, the presence of cristobalite (SiO_2, JCPDS #82-0512) cannot be ruled out.

The EDXRD patterns of the RKKP film and Ti substrate are reported (Figure 6.2). Intense Ti substrate peak contributions make difficult to distinguish the film pattern. Only a few peaks, attributable to RKKP phase composition, have been detected (reflections (a)–(d) in Figure 6.2). In particular, the peak at q = 1.6 Å (a) can be attributed to the wollastonite phase; the peak at q = 2.2 Å (b) to FHAp; the peak at q = 3.0 Å (c) to wollastonite and the peak at *q* =3.9 Å (d) to wollastonite and FHAp. Moreover the presence of a less crystalline β−TCP (β−$Ca_3(PO_4)_2$ cannot be ruled out because its crystalline peaks have scatter parameter in b, c and d position. However, this is not a problem since β−TCP belongs to the class of bioresorbable materials for hard tissue regeneration, therefore it is biologically well tolerated and bioactive and usually used together with HAp in order to improve its bioactivity [170]. EDX analysis, reported in Table 6.1, show a good correlation between the target and the deposited film's composition.

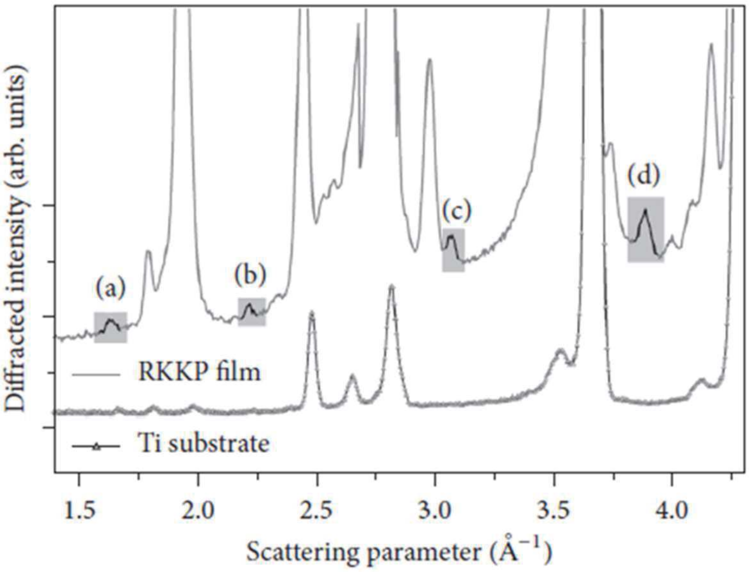

Figure 6.2: EDXRD patterns of the RKKP film, deposited on Ti, and Ti substrate.

Table 6.1: SEM-EDX elemental analysis results for RKKP target and film.

Elements	O	F	Na	Mg	Si	P	K	Ca	La	Ta
RKKP target	45.0	5.2	2.7	1.5	18.2	3.7	0.2	19.6	0.8	3.1
RKKP film	45.6	6.3	4.2	2.4	18.7	3.5	0.2	16.9	0.4	1.8

All the elements in wt %

In Figure 6.3, SEM (a) and AFM (b) surface characterization are shown. The film surface is dense and compact, with the presence of some spherical particles and submicrometric droplets, characteristic for PLD deposition [171]. 5×5 μm^2 AFM images have been collected and the roughness in term of root mean square (r.m.s.) has been measured, that resalted of 8±1 nm.

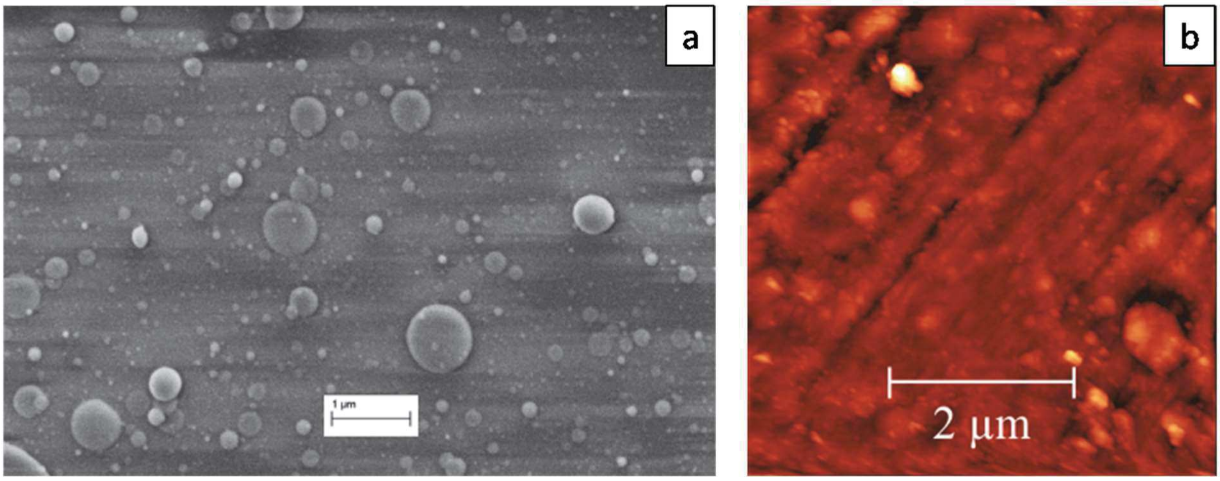

Figure 6.3: SEM (a) and AFM (b) images registered on the RKKP film surface.

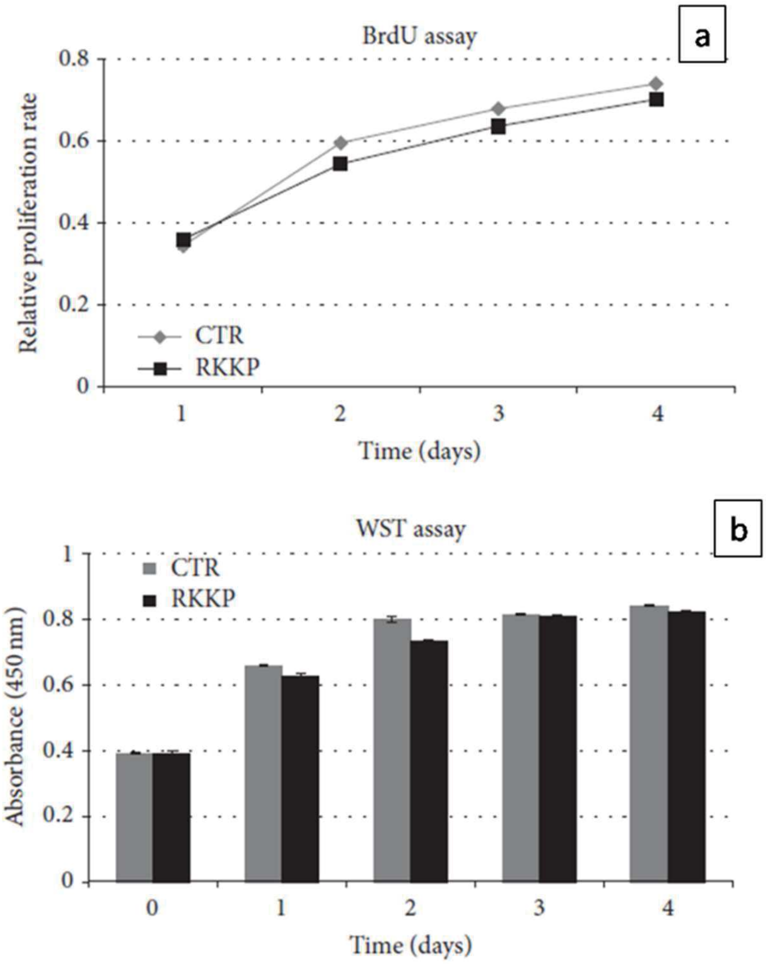

Figure 6.4: Cell proliferation study by BrdU incorporation assay of hAMSCs, seeded on RKKP coated Titanium surface (RKKP) and on treated plastic Petri dish (CTR) (a). Cell metabolic activity analysis of hAMSCs byWST-1 assay of hAMSCs seeded onRKKP coated Ti surface (RKKP) and on treated plastic Petri dish (CTR) (b).

The hAMSCs were seeded both on the RKKP coated Ti surface and on the treated plastic Petri dish, used as control (CTR). Cell proliferation rate has been studied by BrdU incorporation assay and their metabolic activity has been tested by WST-1 colorimetric assay (Figure 6.4). An increasing exponential growth trend of hAMSCs grown on RKKP coated Ti has been observed, similar to the one observed for the control (Figure 6.4 (a)). Cell metabolic activity increased daily and similarly to the control cells (Figure 6.4(b)).

The cell attachment, monitored by staining the nuclei with Hoechst 33342, is shown in Figure 6.5. The collected micrographies have evidenced the increasing in cell density from day 1 up to day 4 (Figure 6.5), that clearly indicate no cytotoxicity of the RKKP coated Ti surface and suggesting a homogenous surface suitable for the placenta derived mesenchymal stem cells attachment also in terms of surface roughness (of 8±1nm).

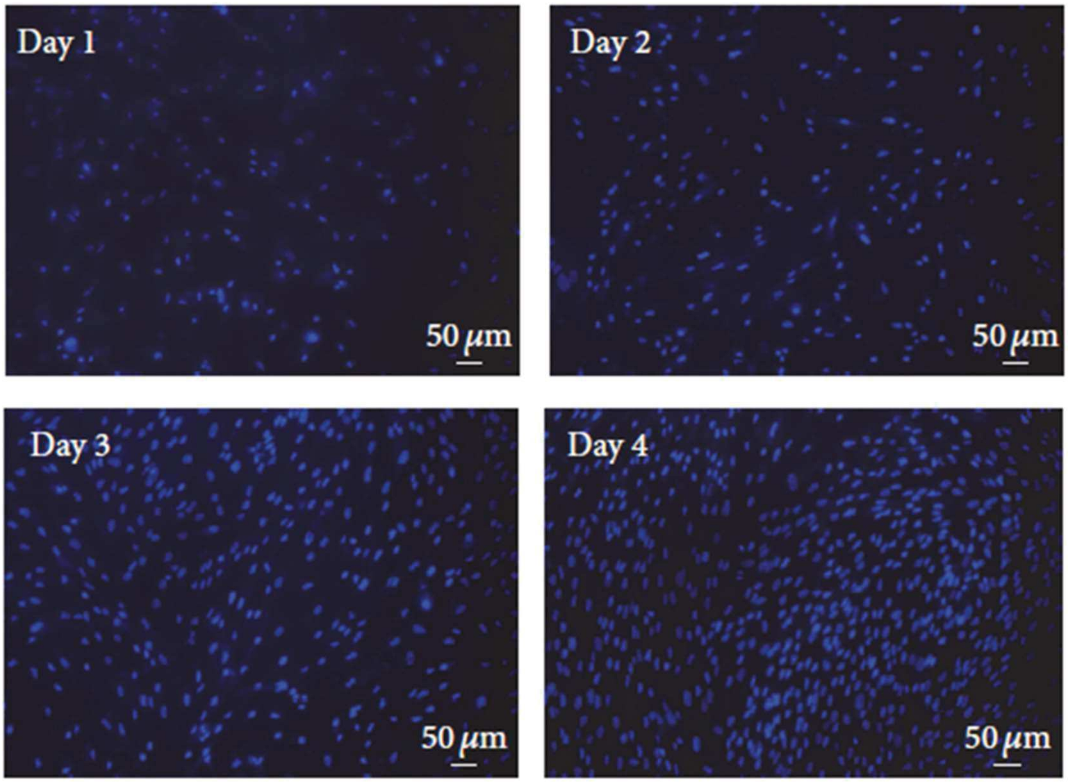

Figure 6.5: Time evolution of hAMSCs' nuclei seeded on RKKP coated Titanium surface, revealed byHoechst staining 33342.

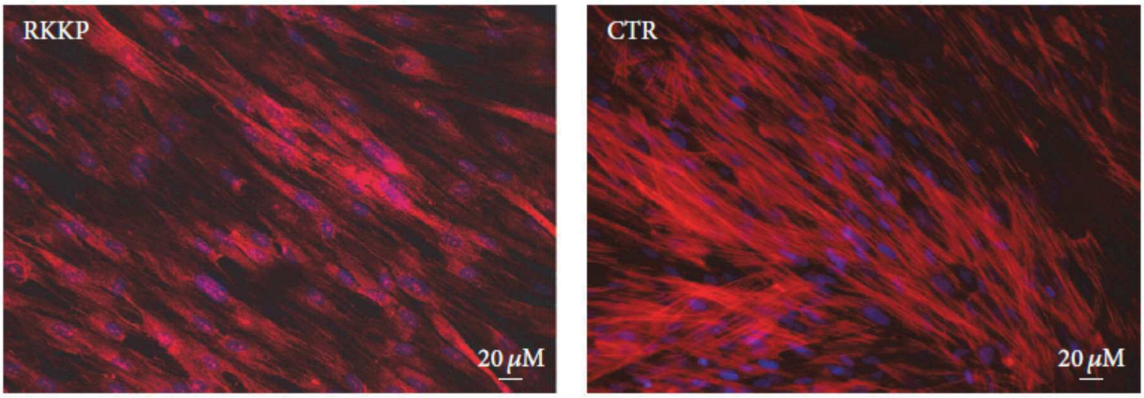

Figure 6.6: Actin distribution analysis of the hAMSCs seeded on RKKP coated Ti surface (RKKP) and on treated plastic Petri dish (CTR).

Phalloidin staining allows to visualize the actin cytoskeleton morphology and organization. The cytoskeleton, essential for maintaining cell shape, is involved in several cell functions associated with the differentiation process, such as the spatial organization of cell organelles, intracellular membrane traffic, modulation of surface receptors, and the mitosis process [172]. The micrographies are shown in Figure 6.6, where it can be noticed that hAMSCs attached on RKKP coated Ti surface maintain their morphology, shape, size, and orientation, similar to the cells grown on treated plastic Petri dishes, allowing the attachment and the actin cytoskeleton organization.

The hAMSCs cycle phase distribution, after two days of growth on the RKKP coated Ti surface and on the treated Petri dish, has been analysed. The cell phase percentage of the former sample has been of 79.63% for cells in G0/G1, 11.14% in S phase, and 9.03% in G2/M and no statistically significant difference was observed in comparison to the control samples, as shown in Figure 6.7.

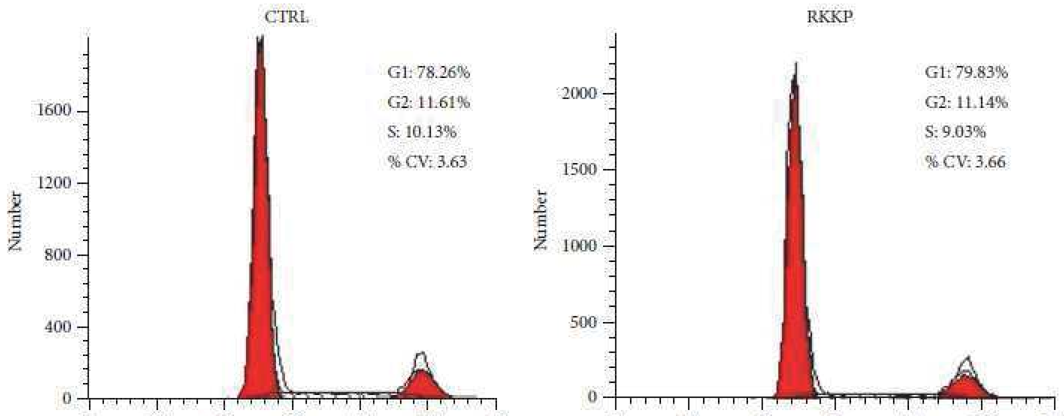

Figure 6.7: Cell cycle analysis of hAMSCs seeded on RKKP coated Ti surface (RKKP) and on treated plastic Petri dish (CTR).

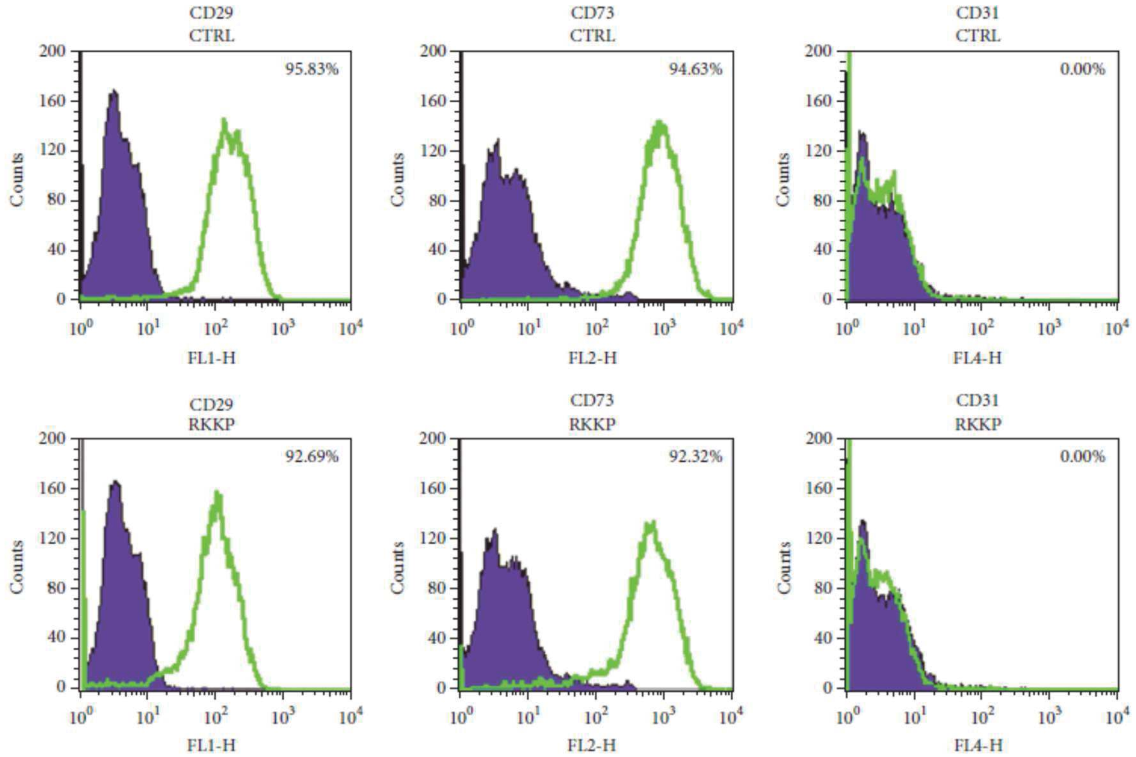

Figure 6.8: Immunophenotypical characterization study for CD29, CD73, and CD31 of hAMSCs grown on RKKP coated Titanium surface (RKKP) and on treated plastic Petri dish (CTR).

For the immunophenotypical characterization (Figure 6.8) the cells have been labelled with antibodies against the mesenchymal CD29 and CD73 stem cell markers and the hematopoietic CD31 cell marker. Both the samples, analysed by flow cytometry, have showed high expression of CD29 and CD73(more than 90%),whereas the CD31 has been undetected.

The mRNA expressions of hAMSC key genes have been investigated. The mRNA transcript levels of anti-inflammatory and trophic factors highly expressed on hAMSCs such as the Transforming Growth Factor β (TGFβ), indoleamine 2,3- dioxygenase (IDO), the Vascular Endothelial Growth Factor (VEGF), the Hepatocyte Growth Factor (HGF), and the housekeeping genes such as β-actin (β- ACT), Ki67, and RPL34 were studied. The messenger expression of these genes in the hAMSCs grown for 4 days on the RKKP film surface resulted similar to the control sample, except for the VEGF (Figure 6.9), that is higher for the RKKP film.

The last test regards the in vitro osteogenic commitment capability. The hAMSCs seeded both on the RKKP coated Ti surface and on the treated plastic Petri dish have been cultured for 7 days in Osteogenic Medium (OM). The mRNA expression has been studied by qRT-PCR assay. The results are shown in Figure 6.10. A statistically significant increasing of the early differentiation markers such as RUNX2 and Alkaline Phosphatase

(ALP), and an initial upregulation of the late differentiation marker, Osteocalcin (OCL), in the cells grown on both types of substrates has been found.

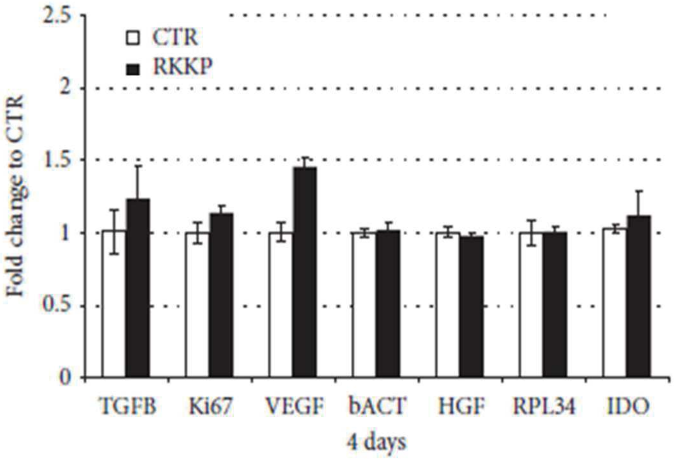

Figure 6.9: qRT-PCR analysis of hAMSC key genes expressions. The TGFβ, IDO, VEGF, HGF, and housekeeping genes (constitutive gene) β-ACT, Ki67, and RPL34. Data are shown as mean ± SD.

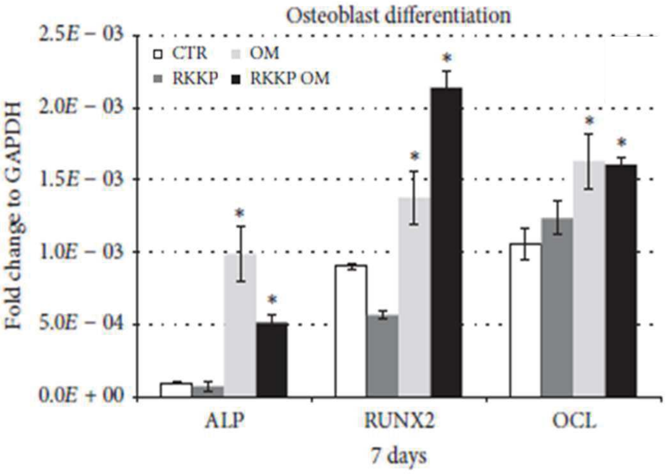

Figure 6.10: qRT-PCR analysis of hAMSC key genes expressions of the early and late osteoblast differentiation markers (RUNX2, ALP, and OCL) expression on hAMSCs grown on coated Ti surface compared to treated plastic Petri dish. Asterisks identify statistical significance ($p < 0.05$). Data are shown as mean ± SD.

In conclusion, the previous demonstrated high quality physical-chemical and mechanical features as well as good biocompatibility [65,166], together with the anti-inflammatory, immunomodulatory, proangiogenic, and proregenerative properties, make hAMSCs cellularized RKKP coated Ti surface a very interesting cell delivery system suitable for tissue engineering applications.

6.2 RKKP films to improve corrosion resistance of Mg-Ca substrates

6.2.1 Introduction

Recently, the interest for the use of biodegradables metals and alloys in bone-related implant application is growing up. The basic idea is to use biodegradables metals for temporary implant. Usually, when a metallic implant is used to temporarily assist tissue healing, such as plates, screws and pins, a second surgical procedure is expected after the tissue has healed. In this context, the use of biodegradable implant, which may help and support the tissue regeneration and degrade completely when healing process is completed, could be really promising [173]. Among the possible degradable metal, magnesium is emerging thanks to its the functional role in physiological systems, as essential element to metabolic activities and the ability to decompose in the body fluid. Moreover, the mechanical properties of magnesium, especially strength and elasticity modulus and its density, very closed to that of the natural bone, make it attractive for tissue engineering applications.

An intake of 300–400 mg of magnesium is normally required daily [174] and redundant magnesium cations can be harmlessly and efficiently excreted in the urine. Recently, it has even been reported that the presence of magnesium in the bone system is beneficial to bone strength and growth [175]. Thus, Mg^{2+} would be easily absorbed in the human body. However, the rapid degradation of Mg is accompanied by the severe side effect of rapid generation of by-products, i.e. hydrogen bubbles in the blood circulating system could cause serious problems, even the death of the patient [174]. Dissolution of magnesium happens through the following reaction [17]:

$$\mathrm{Mg} + 2\,\mathrm{H_2O} \rightarrow \mathrm{Mg(OH)_2} + \mathrm{H_2} \uparrow$$

Therefore, Mg reacts with water, which is plentiful in body fluid, and produces hydroxide and hydrogen. In high pH (>11.5) environments, $Mg(OH)_2$ acts as a protective layer on the surface of magnesium implants, but at lower pH (<11.5) it facilitates magnesium corrosion. Since the local pH at implant-bone interface is about 7.4, Mg corrosion even increases in vivo [174]. That being said, successful application of biodegradable Mg implants requires a controlled kinetics of degradation of Mg and can be improved by using the element alloying method to adjust the composition and the microstructure or by the application of coatings of ceramic, polymer and composite materials [176].

As regards the alloying for hard tissue applications, calcium is one of the most suitable elements [11]. Ca density (1.55 g/cm^3) is very close to that of Mg (1.74 g/cm^3), which helps to preserve magnesium's properties. Several attempts have been carried out in order to find the proper amount of Ca in the Mg for the alloying [17,174,177–179]. Since, Ca is poorly soluble in Mg (approximately 1.34 wt.%), the integration of supersaturated Ca in pure Mg causes the precipitation of Mg_2Ca phase along the grain boundaries. Moreover, Ca addition refines Mg microstructure as a result of thermally stable intermetallic phase formation, that enhances the corrosion.

On the other hand, too high amount of calcium are often difficult to be thermo-mechanically processed due to the workability decreasing, consequently higher amount of calcium can lead to hot cracking during extrusion [177].

Binary Mg-Ca alloys, with low Ca content (0.6–3wt.%) have demonstrated to be promising for orthopaedic applications, but they have a biodegradation rate faster than that required for trauma implants [17]. Therefore Mg–Ca alloys still cannot satisfy the requirements of bone implants. For all these reasons, the coating with a bioactive material, able to slow down the degradation rate of the Mg-Ca implant together with the ability to improve bone regeneration, seems to be a potential solution for the manufacturing of functional degradable implant. Among the different materials eligible for the coating, bioactive glass-ceramics are very promising thanks to their slower biodegradation rate and the beneficial release of trace ions, involved in physiological biochemical cycles.

In this work RKKP glass-ceramic, prepared by melting route, has been deposited by the means of PLD technique. The Mg-Ca (1.4 wt%) substrate has been positioned at 2 cm from the target surface and heated at 400 °C. The PLD has been conducted for 2 hours with a fluence of 12 J/cm^2.

6.2.2 Results and discussion

The composition of RKKP glass-ceramic, prepared by melt-processing synthesis, has been characterised by the means of Raman spectroscopy and ADXRD. The results are shown in Figure 6.11.

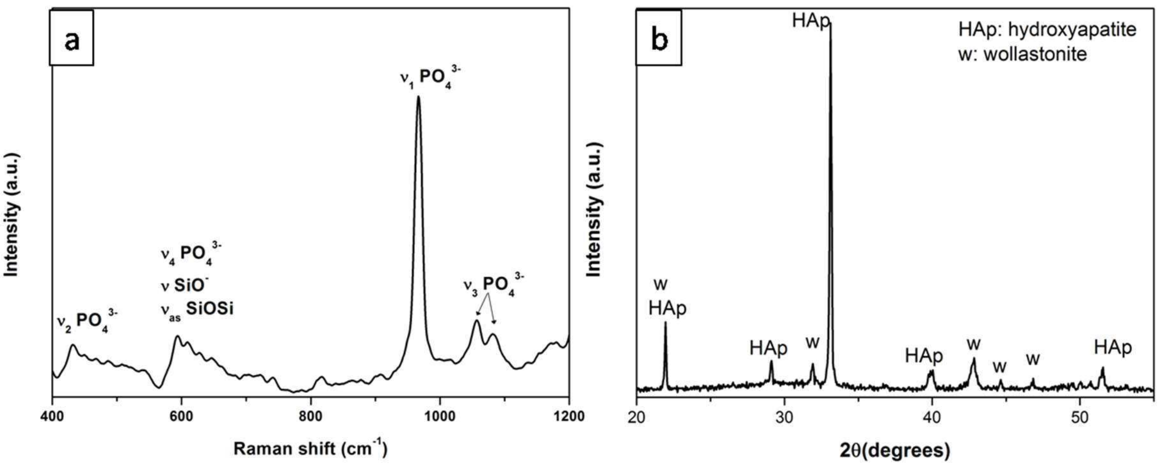

Figure 6.11: Raman spectrum (a) and ADXRD pattern (b) of RKKP bulk material, prepared by melting processing.

Both the analysis have testified the presence of hydroxyapatite and wollastonite crystalline phases. In particular, ADXRD has revealed a peak at 2θ°=21.9, attributable to both HAp and W; the peaks at 29.0, 33.1, 39.9 and 51.5 2θ° can be assigned to the HAp phase, while, the peaks at 31.9, 42.7, 44.7 and 46.9 2θ° are related to the presence of the W phase. All the attribution have been obtained by the comparison with reference X-ray diffractograms of the ICDD database (PDF: 01-074-0566 for HAp and PDF: 00-003-0626 W). Raman spectrum of the RKKP target, reported in Figure 6.11 (a), consists of some broad bands and few sharp peaks. Raman bands centred at 431, 595, 1056 and 1081 cm^{-1} are related to the ν_2, ν_4 and ν_3 vibrational modes of the PO_4^{3-}group of HA, respectively [70,180]. The position of the sharp phosphate ν_1 peak at 968 cm^{-1} indicates a good degree of crystallinity of apatite component of the material [180]. Furthermore, silicate group can contribute to the broad band at 595 cm^{-1}, which results a mixed peak with the contribution of phosphate and silicate groups of the RKKP target [181].

Because of the strong contribution of the substrate material Energy dispersion XRD technique is more appropriate than the Angle dispersion one for the detection of the crystalline structure of thin films. In the spectrum collected on the RKKP deposited films is compared to that of the Mg-Ca substrate (Figure 6.12), in order to eliminate from the attribution the contribution of the latter. All the spectra have been registered at the same scattering angle 2θ=10°. Region of the explored reciprocal space is within 1(Å^{-1})<q<4.5(Å^{-1}). These values can be converted into 2θ values for an easier comparison with ADXRD spectra and literature data. The q range roughly corresponds to 14°<2θ<65°. The diffraction patterns of the Mg-Ca substrate reveals that it is composed of Mg, since no peaks belonging to Ca or Mg-Ca phase have been registered. The positions of the detected peaks has been calculated and compared with literature data and Miller indexes have been assigned. As can be seen, all the reflections (non-belonging to Mg phase) can be attributed to HAp and wollastonite phases. Moreover, some films contribution are missed, such as the HAp reflection at d=2.81 Å → q=2.26 Å^{-1}, because they are overlapped by the substrate reflections. From EDXRD results it is possible to assert that RKKP deposited film is composed of the HAp and W phases, in accordance with the target composition.

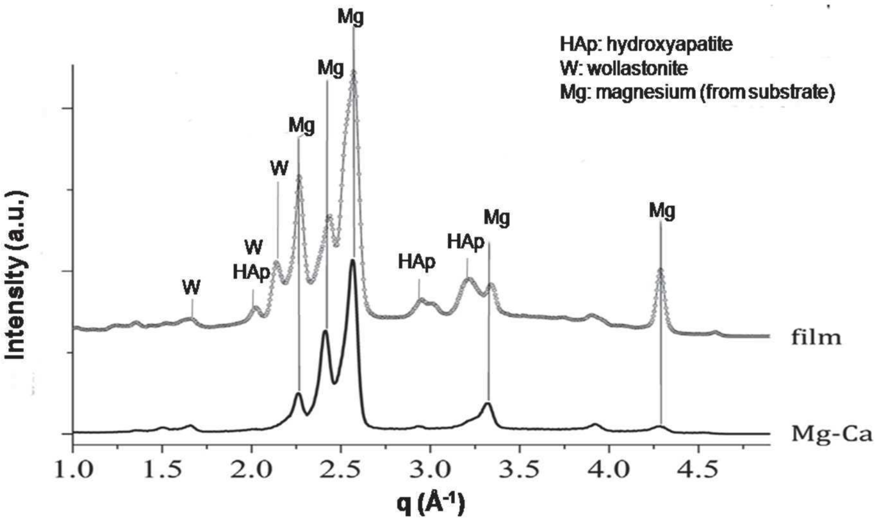

Figure 6.12: EDXRD pattern of RKKP deposited films compared to that of the Mg-Ca substrate.

EDX results testifies that the elemental composition of the target is preserved in the film, even for element in trace, as it is reported in Table 6.2.

Form SEM image in Figure 6.13 (a) it is possible to observe a dense and compact morphology of the film and the absence of cracks and non-covered substrate spaces can be testified. The coating seems to be composed of a amorphous matrix with various size particles included, which is consistent with the nature of glass-ceramic material.

Table 6.2: SEM-EDX elemental analysis results for RKKP target and film.

Element	O	F	Na	Mg	Si	P	K	Ca	La	Ta
RKKP film	66.5	4.7	0.9	4.1	8.0	0.5	0.4	13.4	0.6	0.9
RKKP terget	54.9	2.3	3.5	3.0	18.4	3.6	0.0	17.9	0.1	0.8

All the elements in wt %

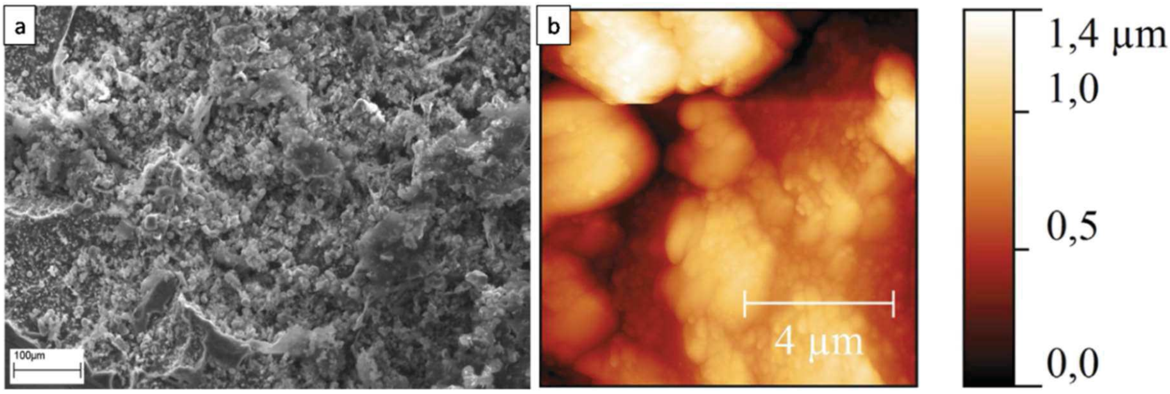

Figure 6.13: SEM (a) and AFM (b) images collescten on the RKKP coated Ti surface.

The surface of the deposited coatings, evaluated by SEM and AFM analysis (Figure 6.13), has a coarse texture, in which dense and heterogeneous agglomerations of glass ceramic clusters, with sizes ranging from micro- to nano- scale dimensions, are completely covered by small particles resulting in a very rough surface. To analyze the typical surface roughness, the area of 10×10 μm^2 was considered. The average surface roughness (r.m.s), has been measured on the entire scanned area, resulting of 295± 30 nm. Such a high value is mainly affected by the contribution of micrometric aggregates. Roughness seems to be a really important parameter for the well-functioning of an implant for hard tissue. Several researches proved that micro- and nano-roughness of surface topography benefits the interaction between bone cells and implant by the stimulation of different biological process [43,44,110,111]. In particular, microscale features improve the adhesion of cells onto the implant surface [44], whereas nanotexture helps the adhesion of the proteins [43]. Therefore the r.m.s. of fine texture has been evaluated. For this purpose, a retailed 5×5 μm^2 square (Figure 6.14) has been selected due to the major presence of finer morphology and a polynomial background of 10th degree has been subtracted. In this way the resulting roughness value shall not be affected by the presence of large grains. Thus, the calculated r.m.s. of the fine-texture particulate is 47±4 nm.

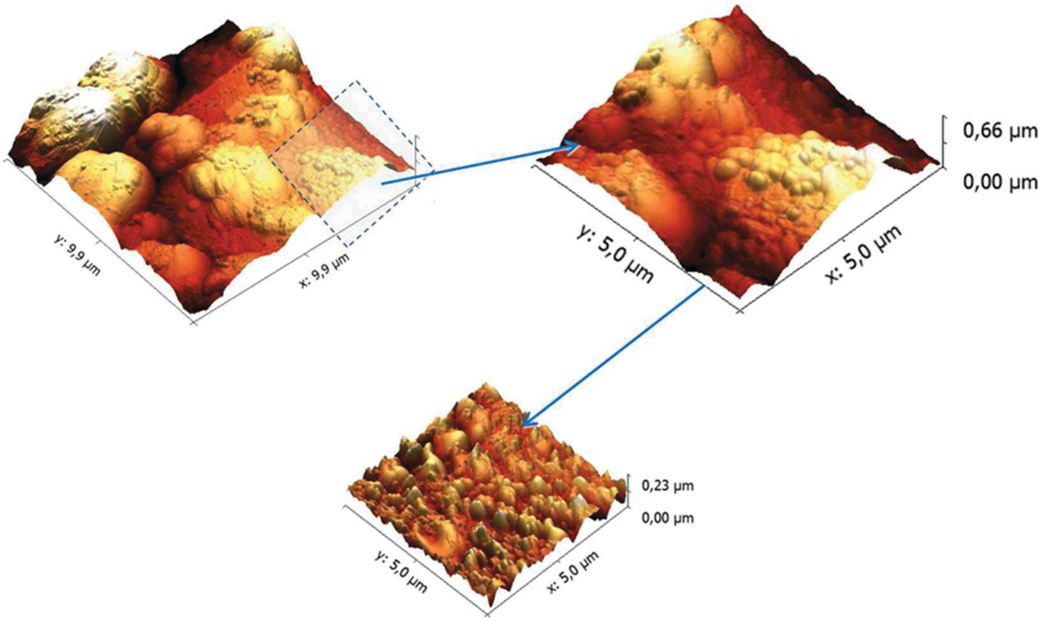

Figure 6.14: AFM 3D view image, the selected square corresponds to the retailed retailed 5×5 μm2 area and the post-processing image, characterized by fine-texture.

Once proved that the obtained film is suitable for a hard tissue implant, the corrosion resistance of the sample has been determined in order to evaluate if such type of thin films are appropriate for the coating of biodegradable implant. For the estimation of the corrosion resistance a Tafel plot electrochemical technique has been carried out in simulated body fluid (SBF) buffer. The Tafel curves, corresponding to the uncoated and RKKP coated Mg-Ca (1.4 wt%) alloys are shown in Figure 6.15 and the main corrosion parameters are presented in Table 6.3. Corrosion resistance of the uncoated and coated Mg-Ca alloys has been examined from different evaluation criteria: the higher corrosion potential, the higher corrosion resistance, while a higher corrosion current corresponds to a worse corrosion resistance.

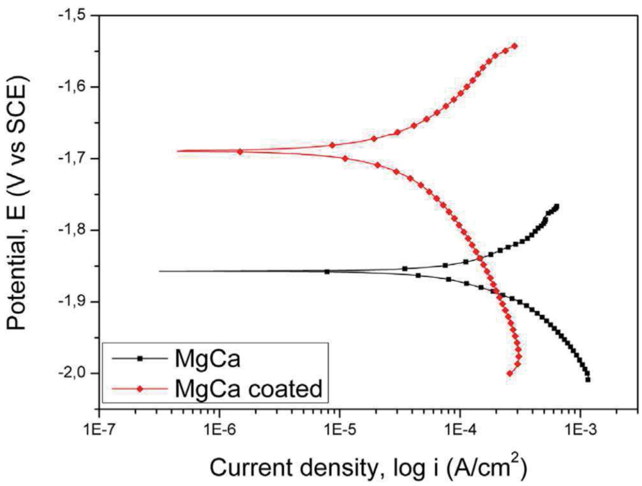

Figure 6.15: Tafel curves for uncoated and RKKP coated Mg-Ca alloy.

Table 6.3: Main corrosion parameters of uncoated and RKKP coated Mg-Ca alloys in SBF solution.

Sample	**E_{corr} (V)**	**I_{corr} (μA/cm^2)**
Uncoated Mg-Ca	– 1.86	575.12
RKKP coated Mg-Ca	– 1.68	61.32

As it is possible to observe from the Figure 6.15 and better in the Table 6.3, the RKKP coated Mg-Ca has a higher electropositive corrosion potential value (−1.68 V) and a corrosion current density 10 times smaller than the uncoated Mg-Ca. Considering these results it is possible to affirm that RKKP glass-ceramics offer protection for the Mg alloy substrates in SBF and provide a suitable corrosion behavior for a possible use as degradable implants.

6.3 PLD of composite carbon-RKKP material for the improving of mechanical properties of the coatings.

6.3.1 Introduction

It is well known that bioactive glass are characterized by poor mechanical properties, which limit their use although their excellent biological properties [182]. Heating treatments of bioactive glass with special composition allow the crystallization of same phases inside the glassy matrix, thus the creation of the already known glass-ceramic. The presence of crystalline phases provides improved mechanical properties to the material [183]. However, usually mechanical properties of glass-ceramic are still not enough for load-bearing application otherwise they are so crystalline that the decreasing or the complete loss of their bioactivity is observed [170,182,183].

In the field of nanomedicine carbon-based materials are emergent materials. The most promising are graphene (G) and its derivates, such as graphene oxide (GO), reduced graphene oxide (RGO), fullerene (C_{60}) and carbon nanotubes (CNTs) [184,185]. They are very attractive thanks to their exceptional capability to stimulate the adhesion of proteins as well as their special reactivity that results in improved cellular functions [186]. Since the advantages of their use lie in the advancement of both biological and mechanical properties, carbon-based biomaterials own a great potential for the development of new efficient biomedical applications [185–188]. In the field of tissue engineering some carbon-based materials have been already investigates. Some of the study conducted in this field are listed below:

- graphene (G) plates have been co-deposited with calcium phosphate per the improving of its mechanical properties [188];
- GO has been used with hydroxyapatite for bone grafting application [189];
- rGO/bioglass composites have been produced for the reduction of ROS (reactive oxygen species), responsible of infections after a surgical treatment [190];
- CNTs have been used to toughen bioactive glasses for scaffold manufacturing [191].

In this context fullerene has been chosen to prepare carbon-RKKP composite film by PLD, with the aim to investigate the possibility to obtain thin homogeneous films with low crystallinity and enhanced hardness.

In this work RKKP glass-ceramic, prepared by melting route, has been mixed with C_{60} powder (5 wt%) and deposited by the means of PLD technique. The Ti substrate has been positioned at 2 cm from the target surface and the deposition temperature has been varied from room temperature (RT) to 500 °C. The obtained films have undergone structural, compositional and morphological characterization as well as microhardness analysis.

6.3.2 Results and discussions

The crystallinity of the RKKP&C_{60} has been evaluated by ADXRD (Figure 6.16 (a)). to facilitate the attribution, the obtained spectrum has been compared to those registered on the RKKP and C_{60} starting powders. The XRD pattern of C_{60} confirms the purity of the crystalline phase of the starting powder (ICDD PDF 00-044-0558). All the diffraction peaks, detected on the RKKP powder, are associated to a crystalline apatite phase (ICDD PDF 00-009-0432). The lack of wollastonite crystalline contributions is reasonably due to the fact that no high-temperature sinterization process has been carried out on the RKKP prepared by melt-processing synthesis. In fact, a wide band that can be related to a glassy phase has been detected. The diffraction spectrum of the RKKP&C_{60} pellet exhibits the same peaks of the RKKP powder. On the other hand, no C_{60} contributions are visible, likely due to its low quantity (5 wt%) in the target material. In order to confirm the presence of C_{60} in the target material, a FT-IR analysis has been performed. In Figure 6.16 (b), the FT-IR spectrum of RKKP&C_{60} target material is reported together with the C_{60} and RKKP spectra. RKKP and, accordingly, RKKP&C_{60} shows a dominating broad band between 840 and 1200 cm^{-1}, in the region where both phosphate and silicate groups have characteristic FT-IR absorption bands [140]. The signals that can be assigned to a silicate glass are: the band centred at 476 cm^{-1} is attributable to bending mode (δSiOSi and δOSiO), the peak at 760 cm^{-1} to the symmetrical stretching (ν_sSiOSi), the shoulder at 1040 cm^{-1} to the antisymmetrical stretching (ν_{as} SiOSi) and the large band centred at 945 cm^{-1} is due to the stretching of SiO^- ions [70]. All the signals are broad, suggesting the amorphous nature of the silicate component. On the other hand, phosphate signals at 603 cm^{-1} (ν_4 PO_4^{3-}), 964 cm^{-1} (ν_1 PO_4^{3-}), and 1040-1095 cm (ν_3 PO_4^{3-}) confirm the presence of a crystalline apatite phase [66], supporting the obtained XRD results (Fig. 1). In addition, the two most intense signals of C_{60} at 523 and 572 cm^{-1}, attributable to T_{1u} vibrational mode [192], are clearly visible in FT-IR spectrum of the composite target.

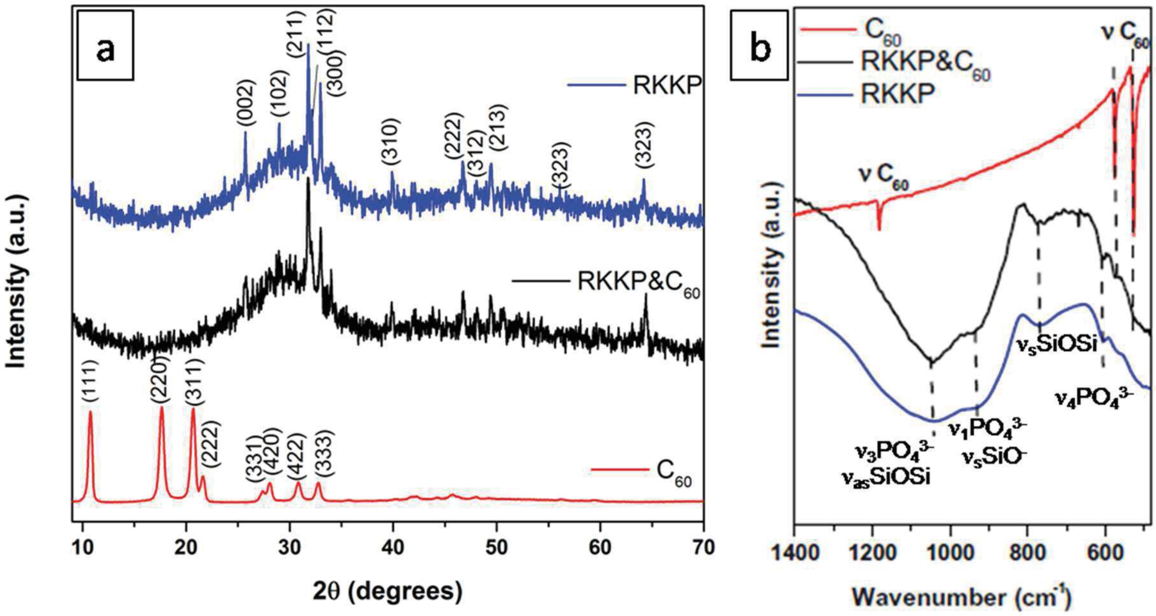

Figure 6.16: ADXRD patterns (a) and FT-IR spectra (b) of RKKP powder, RKKP&C_{60} target material and C_{60} powder.

Once the target was characterized, films at different deposition temperatures (RT, 300 °C, 500 °C) have been deposited.

In order to study the early step of film growth, the deposition of the RKKP&C_{60} has been carried out for few minutes at RT on a copper grid for TEM analysis. On TEM image (Figure 6.17), large fused spherical particles superimposed to a dense background are visible, which suggests that films growth process can be described by a gas-phase condensation and coalescence of droplets, hundreds of nanometers large. This type of film growth is usual for film deposited in vacuum with a ns-laser source irrespective to the target material [108,193].

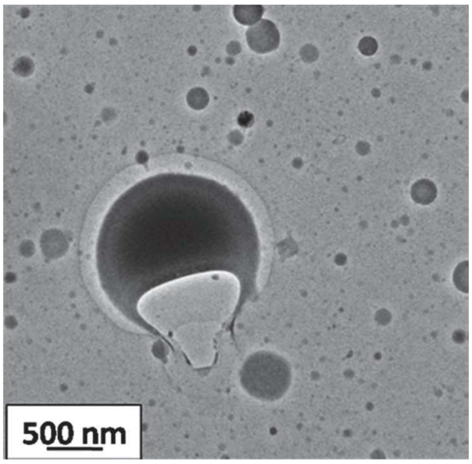

Figure 6.17: TEM image TEM image of the early steps of film growth.

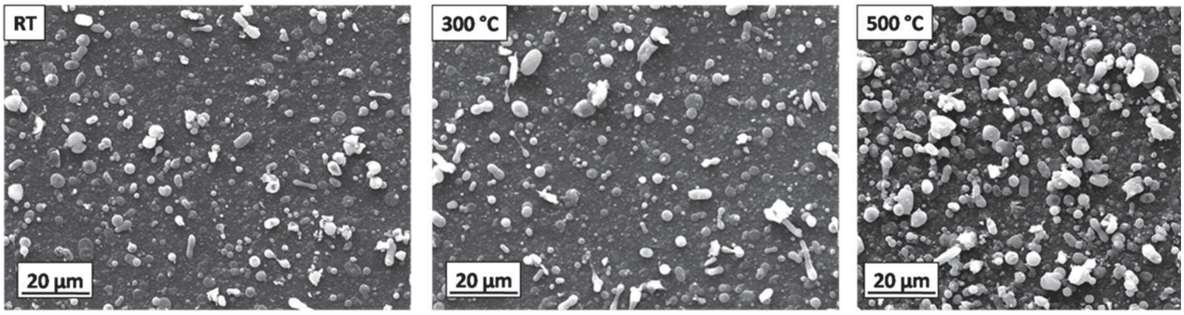

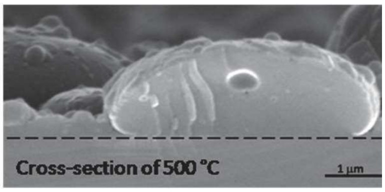

Figure 6.18: SEM images collected on the RKKP&C_{60} deposited on Ti at different temperature and the cross-sectional image of a particles detected on the film deposited at 500 °C.

SEM images, registered on the film deposited at the three different temperatures (Figure 6.18), confirms the film growth mechanism assumed on the base of the TEM image. In fact, the films are formed by micrometric circular and ovoid particulates, which overlap a compact background, as has been highlighted in the cross section image of films deposited at 500 °C. Furthermore, morphological analysis of the deposited films proves that at higher deposition temperatures, the particles mobility increases on the growing film [108]; in fact, the top-flat micrometric droplets visible in films deposited at RT became spherical particles upon the deposition temperature increase. Therefore, a film densification, due to the aggregation and coalescence of nanoparticles, is observed on the film sample deposited at 500 °C. The presence of particulate on film's surface, evidenced in the cross-sectional image, is advantageous for films bioactivity since it provides a higher surface area available for cells adhesion and growth.

In order to investigate the films' topography and measure their roughness, several 10×10 μm^2 and 5×5 μm^2 AFM images have been collected on their surface.

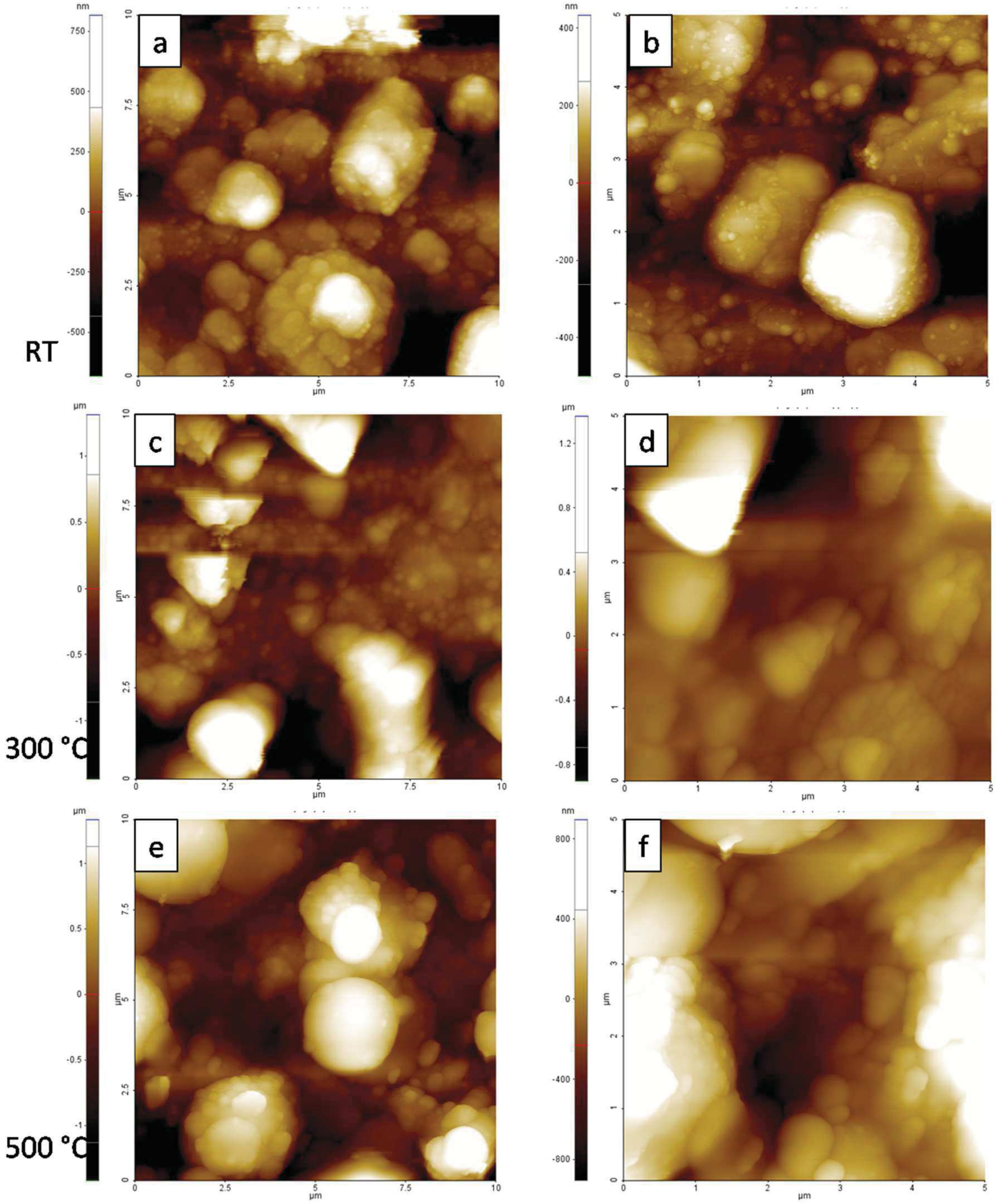

Figure 6.19: AFM images collected on the RKKP&C60 films deposited at RT(a-b), 300 °C (c-d) adn 500 °C (e-f).

Irrespective of deposition temperature, two different morphological features can be distinguished: micrometric structures randomly distributed on the whole surface and sub-micron texture that homogeneously covers the films surface.

Table 6.4: Root mean squares (r.m.s.) values measured on the 10×10 μm^2 and 5×5 μm^2 images collected on the RKKP&C_{60} films deposited at RT, 300 and 500 °C.

RKKP&C_{60} film	**RT**	**300 °C**	**500 °C**
r.m.s on 10×10 μm^2	202±37 nm	437±72 nm	639±52 nm
r.m.s on 5×5 μm^2	129±35 nm	223±74 nm	240±51 nm
r.m.s. of fine texture	71±25 nm	77±7 nm	98±3 nm

The values of roughness are reported in Table 6.4 in term of r.m.s. (root mean square), measured on the whole scanned area of the image. The r.m.s. value varies from 202 nm for films deposited at RT to 437 and 639 nm for films deposited at 300 and 500 °C, respectively. Although a nanometric texture is visible on the image, especially on that at higher magnification, the measure values are more affected by the micrometric structures than by the sub-micrometric features. Therefore, in order to evaluate the roughness of the fine texture, r.m.s. has been calculated in region free of the largest particles (mountains). The obtained r.m.s. values of the fine-texture particulate is of about tens of nanometers for each deposition condition. The increasing of the roughness with the increasing of the deposition temperature confirms, as noted on SEM images, that the deposition at higher substrate temperatures allows the increasing of sub-micron surface roughness. Surface roughness is a critical property for the film-coating bioactivity, and several studies suggest that the multi-scale surface roughness can stimulate different processes at the implant surface [43,110,111]. In particular, nanoscale roughness, with feature sizes comparable to those of the proteins dimensions, can favor the absorption of proteins involved in the regulation of osteoblast proliferation [43], whereas microscale features, which correspond to cell dimensions, influence cells adhesion and differentiation [44]. Thus, the combination of sub-microscale surface roughness with microscale and nanoscale features shall result in an additional effect on cell's differentiation, promoting a stable interface between the implant and the new bone tissue and, consequently, the success of the implant.

The composition of target and films has been investigate by SEM-EDX, in Table 6.5 the results are summarized.

The target composition is slightly enriched in carbon with respect to the RKKP&C60 stoichiometry, probably due to the irregular mixing of C_{60} and RKKP powders or due to the presence of spurious carbon. The deposited films maintain the target elemental composition even for the minor components, but a loss of carbon can be observed for films produced at higher temperatures, suggesting the lost of lighter elements under these deposition conditions.

Table 6.5: SEM-EDX elemental analysis results for RKKP target and films.

wt%	C	O	F	Na	Mg	Si	P	K	Ca	La	Ta
Target	22.6	31.4	1.50	2.65	1.53	16.4	3.05	0.28	19.9	0.49	0.25
RT	19.3	38.1	1.96	1.93	1.32	14.7	1.87	0.12	20.4	0.20	0.11
300ºC	16.3	39.6	2.08	2.58	1.52	16.4	1.63	0.19	19.4	0.21	0.13
500ºC	9.12	35.9	1.63	1.84	1.99	21.1	1.81	0.15	26.2	0.21	0.10

All the elements in wt %

ADXRD, FT-IR and micro-Raman characterizations have been applied on the deposited films in order to determine their structure.

No diffraction signals have been obtained for the ADXRD analysis of all the deposited films. The presence of small crystalline phases cannot be definitively ruled out, since in ADXRD diffraction peaks can be observed only for highly crystalline materials. Moreover the lack of signals confirms that even the deposition at 500 °C has not produced really crystalline coatings, as observed for the other PLD of RKKP [65,67,149]. This is not surprising since films contain carbonaceous materials. In fact, it has been reported that the presence of carbonaceous materials (e.g. RGO or CNTs) can retard film densification and inhibit crystallization of the glass–carbon composite [194].

FT-IR spectra of films (Figure 6.20 (a)) deposited at different temperatures show the same features of the target material (Figure 6.16 (b)), except for the lack of the C_{60} signals. In addition, the phosphate signals at 603 cm^{-1} (ν_4 PO_4^{3-}), typical of crystalline apatite is not clearly distinguishable. With increasing the deposition temperature, the bands became sharper and more similar to the target ones. However, all the spectra are characteristic of amorphous calcium silicate materials.

In order to investigate the nature of the carbonaceous component formed in the film after the ablation process, micro-Raman analysis has been conducted. In Figure 6.20 (b) the Raman spectra registered on the film deposited at RT and 500 °C are shown. In both the spectra the two typical signal are present: D and G bands in the region between 1000 and 1800 cm^{-1}. The G band, which is related to E_{2g} symmetry for graphite, is caused by the in-plane bond-stretching motion of a couple of sp^2 carbons, whereas while the D-band is attributed to the “disordered carbon”, i.e. the bond angle disorder in the sp^2 microdomains, induced by linking with sp^3 carbon atoms [195,196]. The presence, of fullerene cannot be excluded since Raman signals fall exactly in the range of the broad and intense D–G bands

[196,197]. D and G positions and relative intensity provide information on the nature of the carbonaceous material. The film deposited at RT presents signals typical of an amorphous carbon, with a high I_D/I_G ratio (2.5) and broad D and G bands centered at 1345 and 1582 cm^{-1}, respectively. Depositing at higher temperature seems to allow a decreasing of defects and disorder density since I_D/I_G ratio is lower (1.9) and D band is sharper. D and G peaks position (1329 and 1590 cm-1, respectively) and the intensity ratio of the film deposited at 500 °C is similar to Raman spectra of RGO-like structures [198].

The missing of the fullerene signals in both the FT-IR and Raman analysis can be due to its effective absence in the films as a result of the interaction with the laser beam during the ablation process. The laser ablation of C_{60}, reported in other works, led to the formation of DLC films, during the PLD in vacuum [196], while the ablation in water led to the collapse of the cage structure resulting from the formation of C-H bonds [198]. A similar process can be figured for collapse of the C_{60} cage during a nanosecond ablation process. In fact, the interaction between the ns-laser beam and RKKP&C_{60} target causes the formation of a dense and hot plasma, containing atoms, ions and radicals of the elements constituting the target. The oxygen radicals present in the plasma plume can bond to the fullerene structure and induce the C–C cleavage and the following cage opening [199]. In these conditions, the formation of few layers graphene oxidize sheets is expected.

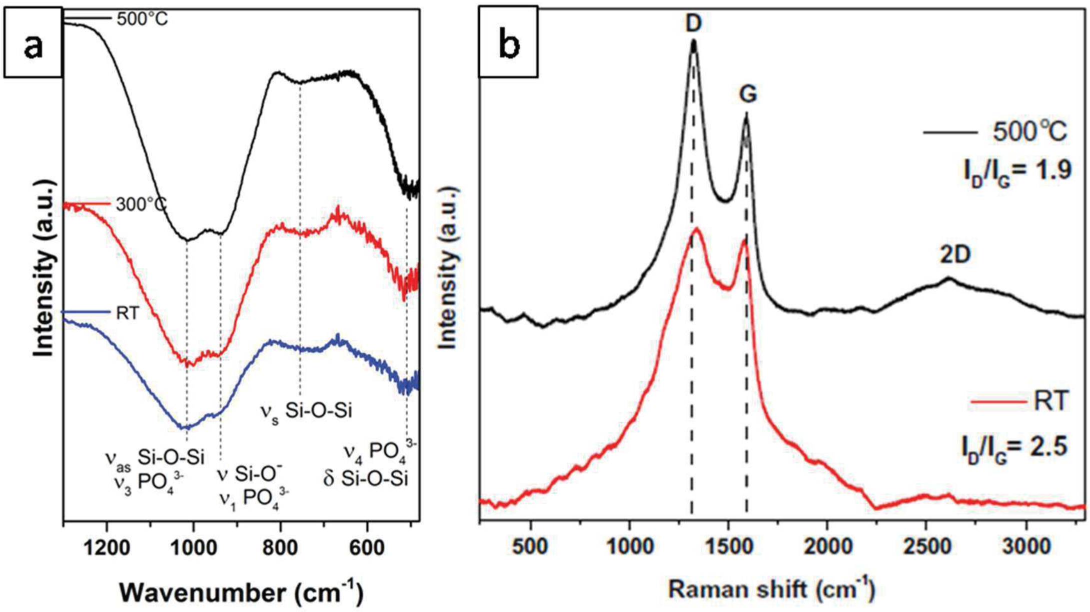

Figure 6.20: FT-IR spectra of RKKP&C_{60} films deposited at 500, 300 °C and RT (a) and Raman spectra of the films deposited at 500 °C and RT(b).

The experimental data on the microhardness measurements for the film deposited at room temperature and at 500 ºC are presented in (Tables 6.6-6.8). In the Tables 6.6 and 6.7, the applied load, average imprint diagonal and the composite hardness values are given. From these data, knowing the film thickness, it is possible to obtain the intrinsic film hardness (Table 6.8) by the Jönsson and Hogmark equation (see section 3.8.2 d). The obtained values of microhardness measurements testify the improvement of mechanical characteristics of the RKKP&C_{60} with respect to RKKP films reported previously. For comparison, values of microhardness measured for crystalline films obtained by the PLD of two different RKKP target materials have been of 25 ± 3 GPa and 17 ± 2 GPa [65]

Table 6.6: Experimental data (composite hardness versus load) for the film deposited at RT.

Number of point	Applied Load, N	D average, µm	Hc average, GPa
5	0.098	6.4 ± 0.3	4.51 ± 0.40
4	0.147	8.7 ± 0.8	3.61 ± 0.73
8	0.245	13.3 ± 0.4	2.61 ± 0.16
8	0.490	21.1 ± 1.1	2.10 ± 0.22
7	0.981	30.5 ± 0.8	2.00 ± 0.10
6	1.961	46.2 ± 1.1	1.74 ± 0.08
6	2.942	57.5 ± 2.6	1.69 ± 0.16
6	4.903	68.2 ± 13.7	1.70 ± 0.07
6	9.806	110.6 ± 0.4	1.52 ± 0.01

Table 6.7: Experimental data (composite hardness versus load) for the film deposited at 500 °C.

Number of point	Applied Load, N	D average, µm	Hc average, GPa
3	0.245	10.4 ± 1.0	4.24 ± 0.83
2	0.490	19.6 ± 0.6	2.42 ± 0.15
3	0.981	30.8 ± 2.3	1.96 ± 0.27
4	1.961	46.5 ± 1.3	1.71 ± 0.09
7	2.942	58.7 ± 3.1	1.64 ± 0.14
6	4.903	76.5 ± 0.8	1.58 ± 0.03
12	9.806	109.3 ± 2.1	1.55 ± 0.06
12	19.611	158.9 ± 3.1	1.47 ± 0.06

Table 6.8: Vickers microhardness and thickness of the films deposited on Ti substrate.

	Thickness (µm)	Intrinsic film hardness (GPa)
RKKP&C_{60} film at 500 °C	0.5±0.2	31±7
RKKP&C_{60} film at RT	0.4±0.1	8±4

Since low apatite formation and reduced ion release have been observed for more crystalline glasses [31] the amorphous character of the obtained films is more desirable for the biological performances. On the other hand, the presence of crystalline phase into the glass structure is desirable for the improving of the mechanical properties of the film coating. Laser ablation of RKKP&C_{60} pressed powder allows to obtain amorphous films with enhanced hardness, thanks to the carbonaceous component homogeneously distributed in the films. The increase of film hardness with deposition temperature can be related to changes of the carbon arrangement in the film, with a decrease in structural disorder as it was possible to observe by Raman analysis .

It is necessary that the coating maintains its integrity because a possible cracking effects delamination and spalling, exposing the metal bulk to the physiologic environment [200], which can leads to the corrosion of the metal with the releasing of eventual toxic products in the organism, or in the case of the biodegradable implant their resorption in advance. Since hard tissue implants are subjected to external loads and stresses, the improvement of the coatings's microhardness can favor the success of the implant.

6.4 Bone-like apatite formation on RKKP_Mn coatings obtained by PLD

This work has been carried out in collaboration with ISM-CNR, Montelibretti Unit (RM), where the RKKP_Mn glass-ceramic has been synthesized, and the Institute of Biomaterials, Department of Materials Science and Engineering, University of Erlangen-Nuremberg, headed by Prof. Dr.-Ing. habil. Aldo R. Boccaccini, where cytotoxicity tests have been performed.

6.4.1 Introduction

With an aging population, the incidence of fractures caused by osteoporosis is increasing [201]. As defined by the World Health Organization "*Osteoporosis is a skeletal disease* *characterized by low bone mass and microarchitectural deterioration of bone tissue with a consequent increase in bone fragility and susceptibility to fracture*" [201,202]. This pathology prevails in postmenopausal women, but several studies demonstrated that man can suffer as well [203,204].

One of the most common fracture caused by osteoporosis is the hip fracture, which requires the substitution with a prosthesis. Certainly, this type of surgeries in patients with osteoporosis can causes more diseases that on healthy patients: the lack of calcium in the surrounding bone and its abnormal metabolism can slow down the healing process. Therefore, it should be useful to include in materials designed for regeneration of osteoporotic bone trace elements with a specific role in the biological process upon the implantation. Among these elements, calcium plays definitely the most important role in bone metabolism; nevertheless, the key function of manganese in the maintenance of bone mass has been demonstrated [205,206].

Mn is an important cofactor of several enzymes involved in extracellularmatrix (ECM) remodelling and synthesis of proteoglycans, important constituents of skeletal and cartilage structural matrices [207,208]; therefore, its deficit retards osteogenesis. Low content of Mn in the body is connected with the increasing of the extracellular concentration of calcium and phosphates [204]. The research group of Landete-Castillejos individuated a strong connection between the dietary lack of Mn and the bone fragility. They studied the genesis of the brittleness of deer antlers (an excellent model for studying bone biology) after a very hard winter. They discovered that cause was the deficit of Mn, because frozen plants are usually characterized by an increasing in Si content, and as a consequence the reducing of Mn [209]. After several studies, they indicated the loss of calcium as a consequence and not the cause of the osteoporosis [210]. The incorporation of Mn ions could be a powerful way to improve bone healing in terms of bioactivity, cell differentiation and mineralization rate [211]. Furthermore, Mn increases the activity of the integrins, a family of receptor that mediate the cellular interaction with the extracellular matrix [212], thus Mn incorporated in bioceramics can improve the cell adhesion.

Given the roles of manganese in the bone osteogenesis and osteoporosis, in this work a small percentage (2%) of manganese oxide has been added in the RKKP glass-ceramic composition. The RKKP_Mn material, obtained by sol-gel synthesis, has been used to coat titanium support by PLD, in order to obtain an improved bioceramics coating for bone implant adequate for the replacement of osteoporotic bone. In this preliminary work, structure and composition of RKKP_Mn have been characterized, then its biocompatibility and the in vitro bioactivity of the deposited films have been tested.

6.4.2 Results and discussion

a *Physical-chemical characterization of RKKP_Mn bulk material*

The crystalline structure of RKKP_Mn bulk material has been characterized by ADXRD. In Figure 6.21 the diffraction spectrum is shown. Three different crystalline phases have been detected: cristobalite (SiO_2, ICDD PDF: 00-027-0605), wollastonite ($CaSiO_3$, ICDD PDF: 00-003-0626) and hydroxyapatite ($Ca_{10}(PO_4)_6(OH)_2$, ICDD PDF: 01-074-0566).

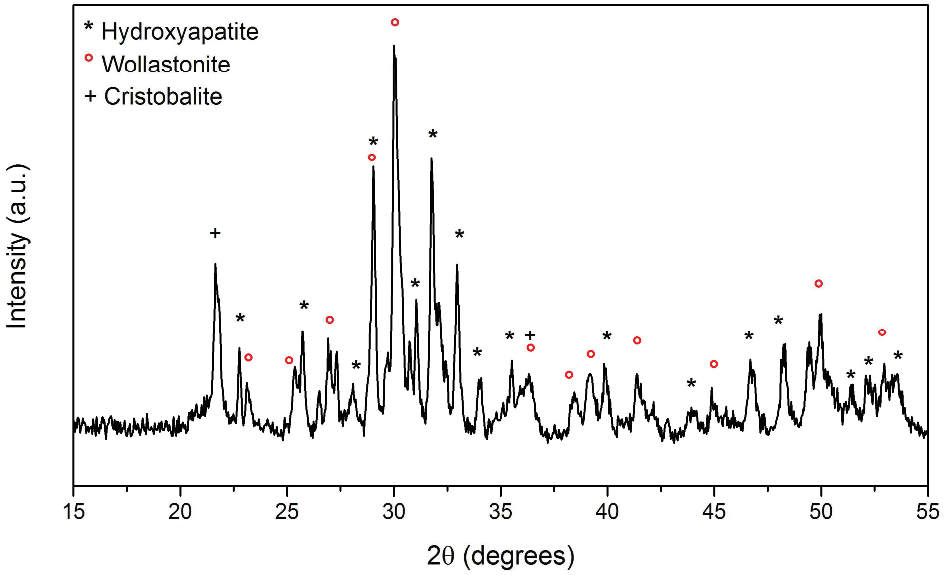

Figure 6.21: ADXRD pattern of RKKP_Mn target material.

In the Raman spectrum (Figure 6.22) typical wollastonite and hyroxyapatite (HAp) signals are superimposed on a large luminescence band, probably due to the amorphous component of the glass-ceramic. This is the reason why only the more intense signals of HAp are visible, i.e. the stretching ν_1 PO_4^{3-} at 963 cm^{-1} and ν_3 PO_4^{3-} at 1051 cm^{-1}[108,112].

Regarding wollastonite vibrational mode, signals at 667 and 1013 cm^{-1} are due to the rocking and stretching of Si-O-Si, respectively [213], while at 637 cm^{-1} mixed stretching and bending mode is detectable [108,181]. To the vibration of Si-O$^-$ (non-bridging oxigen) are attributable the signals at 970 and 1051 cm^{-1} [213]. Finally bands centred at 326, 392 and 417 cm^{-1} can be assigned to the Si-O-Si silicate network deformation mode of wollastonite crystal [108,181].

The frequency shift and intensity variation of the Raman signals are due to the presence of alkali, alkali earth and others bivalent cations which act as network modifiers, decreasing the local symmetry in the silica network [37,108]. The presence of two distinct peaks at 963 and 970 cm^{-1} of the stretching of phosphate and Si-O-Si groups, respectively, supports the glass-in-glass phase separation occurrence, characterised by the formation of immiscible silicate-rich and a phosphate-rich phases within the glassy matrix This effect has been already observed in previous work on RKKP and other glass-ceramic materials [66,108].

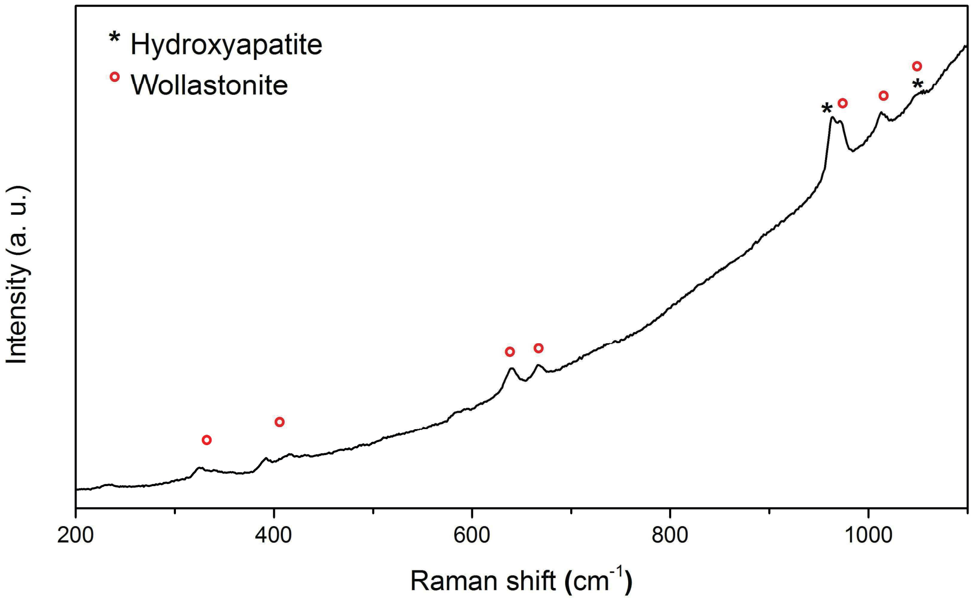

Figure 6.22: Raman spectrum of RKKP_Mn target material.

The FT-IR analysis (Figure 6.23) on the bulk material confirm the results obtained by Raman spectroscopy and ADXRD. All the signals that can be assigned to phosphate and silicate characteristic absorption bands. In particular, the identification of the PO_4^{3-} characteristic vibrational modes at 564 cm^{-1} (ν_4 PO_4^{3-}), and the bands centred at 925 and 1065 cm^{-1} (ν_1 PO_4^{3-} and ν_3 PO_4^{3-}, respectively), have testified the presence of the apatite crystalline phase, in agreement with the ADXRD data. However, the shoulder at around 1200 cm^{-1} can be attributed to the ν_5 POH [70]. Concerning the silicate phase, from the FT-IR spectrum it is possible to suppose the presence of both the residual glassy matrix and the crystalline phase, justifying the luminescence band in the Raman spectrum. The signal distinctive of a modified silica network has been found at 925 cm^{-1}, related to the stretching of silicate with non-bridging oxygen [141]. On the contrary, the signal at 790 cm^{-1} is due to the bending vibration of bridging oxygens in a direction perpendicular to the

Si–Si axis and within the Si–O–Si plane, when all the oxygens are bridging [214]. The other signals related to silicate vibration have been found at 474 cm^{-1} (δSiOSi), 695 cm^{-1} (ν_sSiOSi), 1065 cm^{-1} (ν_{as}SiOSi) [140,141,214].

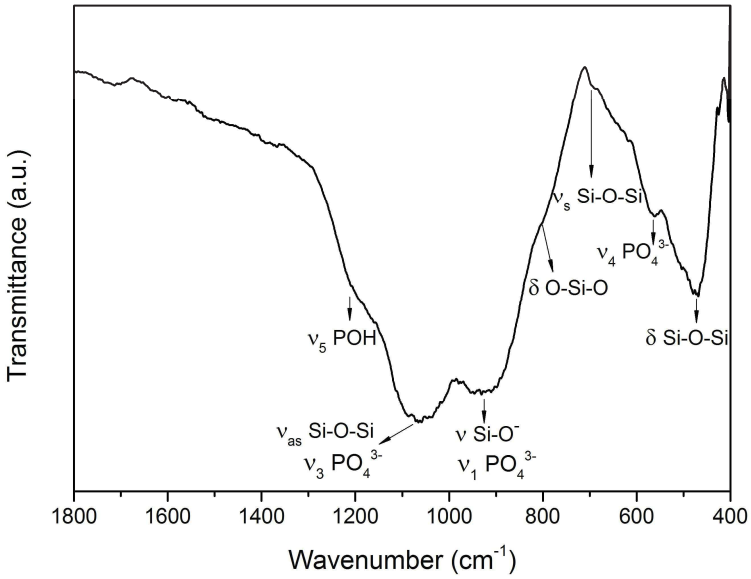

Figure 6.23: FT-IR spectrum of RKKP_Mn target material

b *Biocompatibility characterization of RKKP_Mn starting material*

The biocompatibility of RKKP_Mn bulk material has been tested. At this purpose MG-63 cells, which are human osteoblast-like cells, has been used in order to test its citotoxicity. MG-63 cells have been incubated with different amounts of RKKP_Mn powder (0.1, 1.0 and 10.0 mg/ml), suspended in DMEM. Cell viability has been measured after 2 days of incubation by the means of WST-8 assay, the results are shown in Figure 6.24. During the incubation period, viable cells have converted the WST in formazan dye with specific absorbance at 450 nm. The results of the spectrophotometric measurements are shown in Figure 6.24 (a). The metabolic activity of the cells co-cultured with the 0.1 mg/ml of RKKP_Mn shows no significant difference in comparison to the control samples (CTR, cell culture plate without RKKP_Mn suspension), however with the increasing of the RKKP_Mn quantity, the metabolic activity of the cells decreases, which indicates that the number of viable cells decreases. However it is necessary to underline that this colorimetric assay could be affected by the light pink colour of the RKKP_Mn (for the presence of manganese oxide not completely incorporated in the silicate network [211]). In addition, the decreasing of the metabolic activity has been possibly due to the cell differentiation. Several authors have reported that cells show less metabolic activity during the differentiation process [215–217]. Usually after longer incubation period it is possible to observe the improving of the viability, an indication of the increasing of the cells density. For all these reasons this type of test alone is not enough to define the citoxicity of the material.

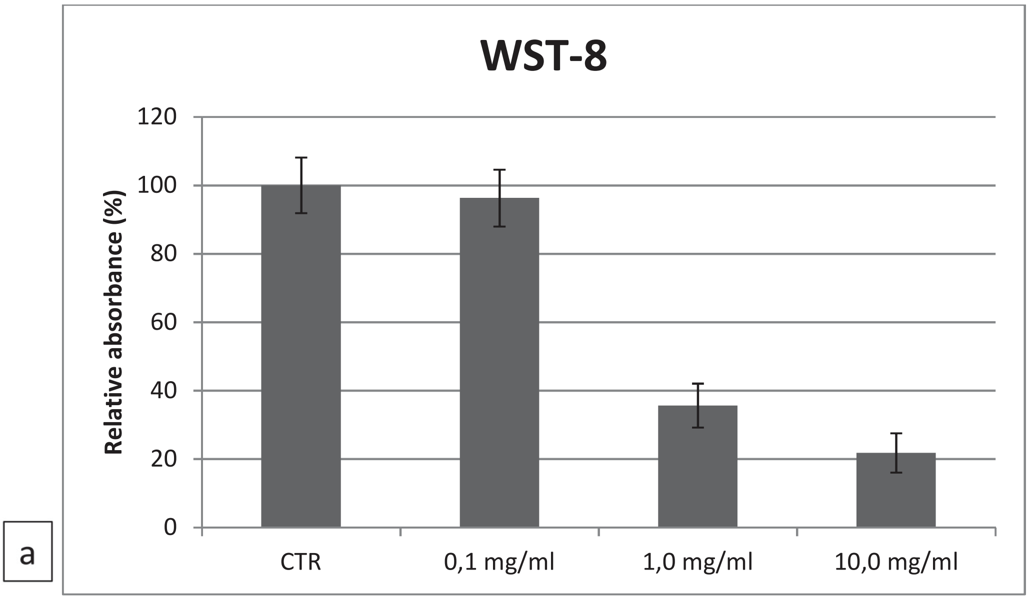

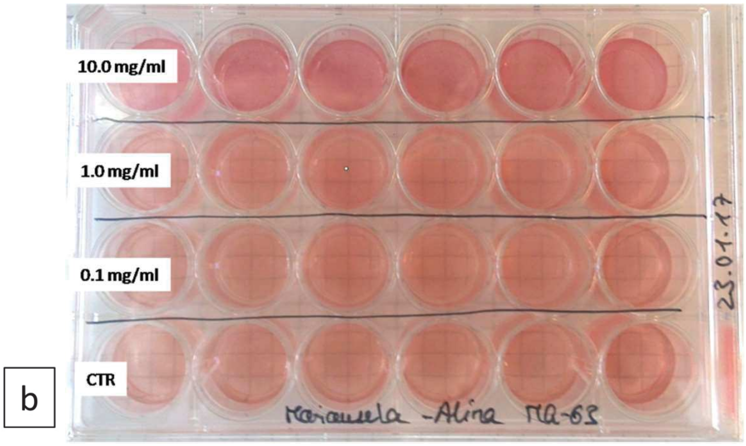

Figure 6.24 Cell metabolic activity analysis of hAMSCs by WST-8 assay of MG-63 cultured for 2 days alone (CTR) and with different amount of RKKP_Mn powder, resulting from the absorbance measurement at 450 nm (a) and the picture of the samples (b).

The same cells have been then stained with calcein AM, in order to mark the cytoplasm of living cells, and DAPI, which gives information about the integrity of the nucleus. A fluorescent microscope has been used to analyze the cells density and distribution. In Figure 6.25 the collected images has been reported. Although the number of viable cells is decreased with the concentration of RKKP_Mn in the culture media, as is visible in Figure 6.25, well and uniformly dispersed cells with intact nucleus are observable for all the samples. No difference can be recognized between the cells cultured with the CTR and in the 0.10 mg/ml RKKP_Mn suspension. Whereas cells cultured in 1.0 and 10.0 mg/ml RKKP_Mn are mainly elongated, which indicates spreading and proliferating cells [215].

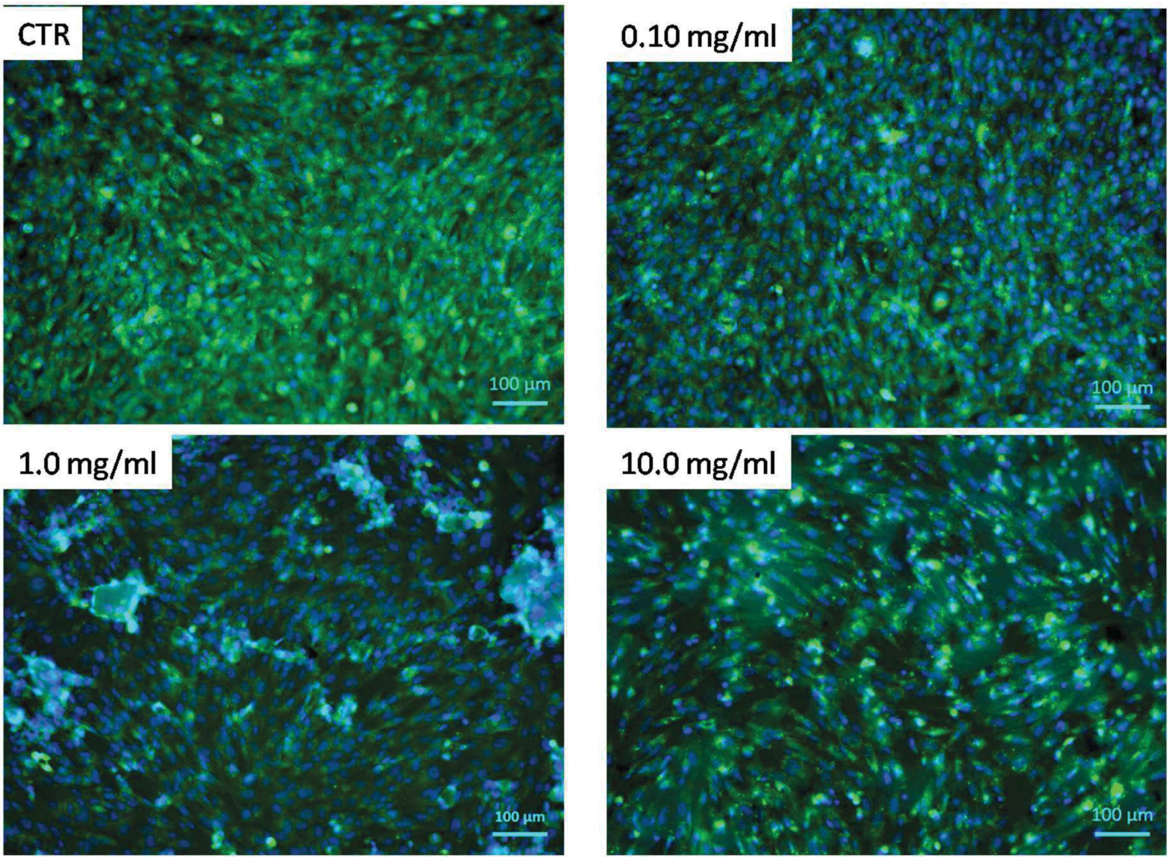

Figure 6.25: Fluorescence images of MG-63 cells cultured for 2 days alone (CTR) and with different amount of RKKP_Mn powder, resulting from the staining with calcein AM (for cytoplasm) and DAPI (for nuclei).

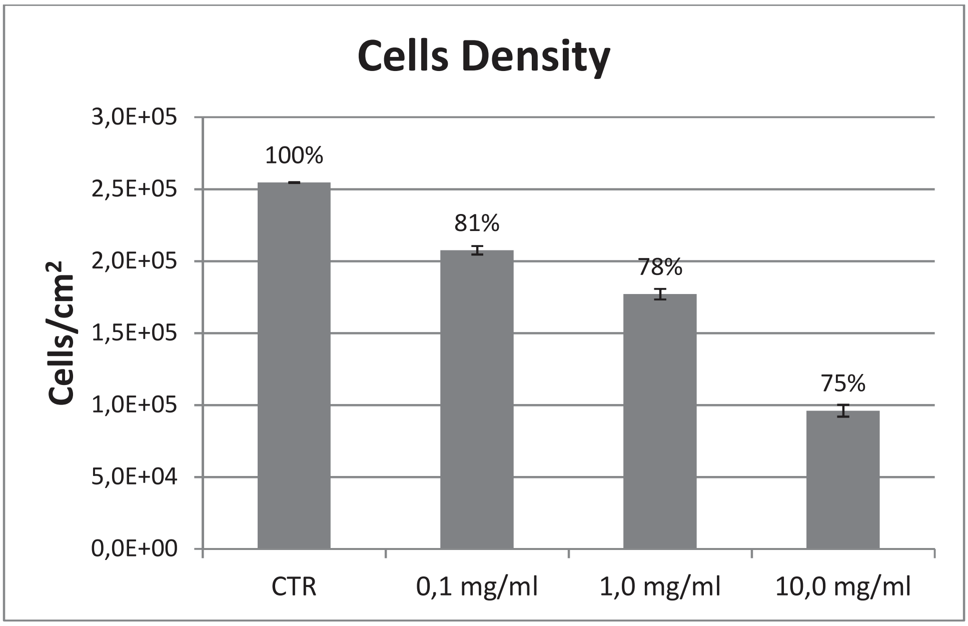

Figure 6.26: Cells density measured on the fluorescence images reported in Figure 6.25.

The results obtained by calcein AM and DAPI staining have confirmed the suppositions regarding the WST-8 assay validity for such type of material, namely the colour of the RKKP_Mn powder have has affected the spectrophotometric analysis. In fact, despite the reduction in the number of alive cells is visible after the calcein staining, even at high concentration of the glass-ceramic, after 2 days the viable cells are the 75% with respect to the control.

c *Films deposition, characterization and bioactivity*

Once structure, composition and biocompatibility have been characterized, the RKKP_Mn material has been used to coat Ti substrates by the means of PLD. All the film have been deposited for 4h at two different substrate temperature: room temperature (RT) and 500 °C. The ADXRD spectra of the obtained films, compared to the target one are shown in Figure 6.27. All the most intense peaks of the target material have been found in the films spectra and no extra peaks have been detected, apart from the substrate contributions. The films deposited at 500 °C is definitely more crystalline than the one obtained at RT, because when the substrate is kept at high temperature the arriving ablated material can easily recrystallize.

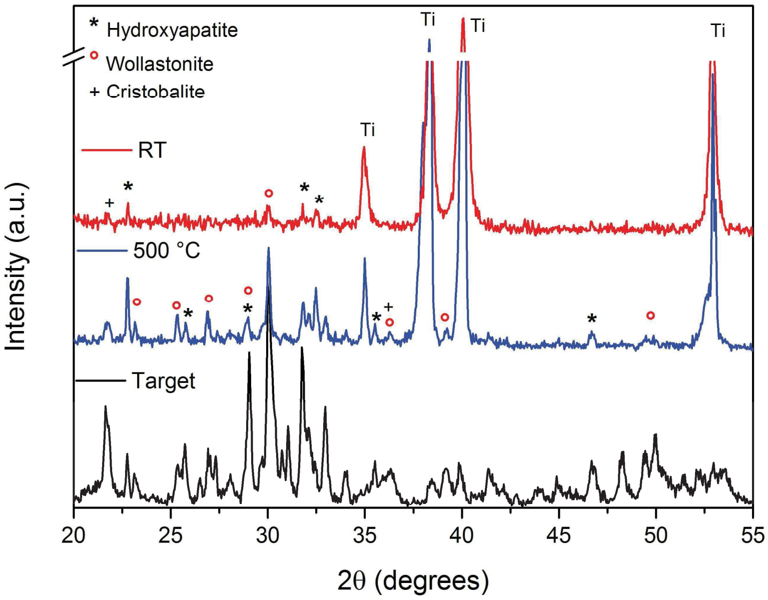

Figure 6.27: ADXRD patterns of RKKP_Mn films deposited on Ti at RT and 500 °C, compared to the target one.

Differences between the two films are detectable also in the SEM images in Figure 6.28. Although both the films are composed of a compact layer of nano and micro particles, the film deposited at RT presents a number of flat particles (originated directly from the melt droplets, coming from the plasma). On the contrary, the film deposited at 500 °C shows the presence of bigger spherical particles, that supports the idea of a recrystallization process during the film growth on the heated substrate.

Furthermore the composition of the two films has been defined by EDX analysis. The results, compared to the target composition (in Table 6.9), suggest that a congruent phase transfer has occurred during the ablation-deposition process, since also the stoichiometry of the minor components has been kept.

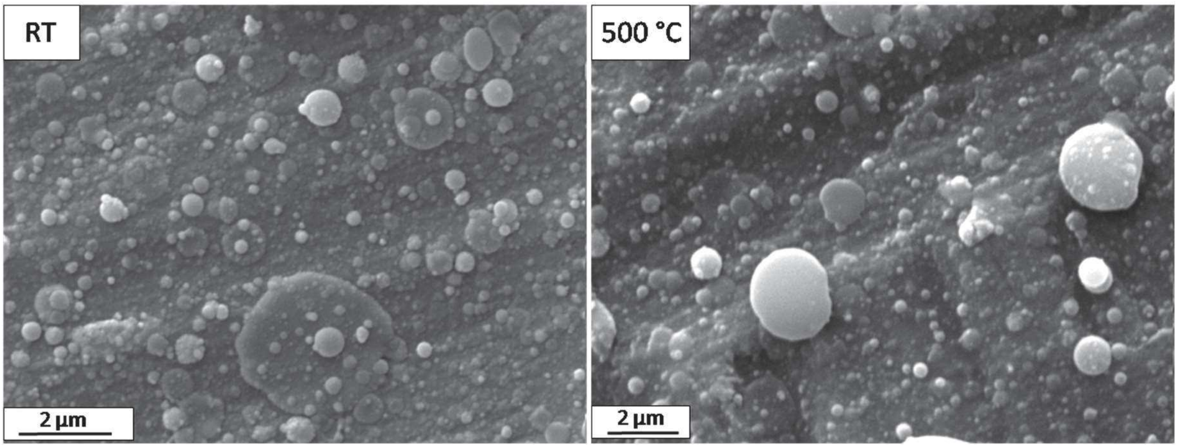

Figure 6.28: SEM images collected on RKKP_Mn films deposited on Ti at RT and 500 °C.

Table 6.9: SEM-EDX elemental analysis results for RKKP_Mn target and films.

Elements	O	Na	Mg	Si	P	Ca	Mn	La	Ta
Target	33.9	1.7	2.5	24.2	5.5	29.2	1.9	0.1	0.9
RT	32.2	2.0	2.6	24.0	10.6	25.2	2.0	0.3	1.0
500 °C	38.0	1.1	1.8	23.3	4.0	29.0	1.4	0.2	1.5

All the elements in wt %

In order to study the influence of the film crystallinity on the bioactivity, films deposited at both the conditions have been tested in vitro by the immersion in simulated body fluid (SBF). This fluid has an ion concentration very close to those of human blood plasma, therefore the in vivo bioactivity of the coatings can be predicted according to the apatite formation on its surface in SBF [63]. Each sample has been soaked for different time, i.e. 3, 7,14 and 28 days. The apatite formation has been investigated with Raman spectroscopy, ADXRD and SEM-EDX techniques.

Raman spectra registered on the RKKP_Mn coated Ti after different immersion time points are reported in Figure 6.29. Raman spectrum of the non-soaked samples shows the typical signals of a silicate phase for both the films deposited at RT and 500 °C; from three days of immersion in SBF, only phosphate signals are detectable. The signals attributions are summarized in the Table 6.10. No differences can be detected from Raman analysis on the behaviour in SBF of the films deposited with the two different deposition temperature, therefore with a different crystallinity.

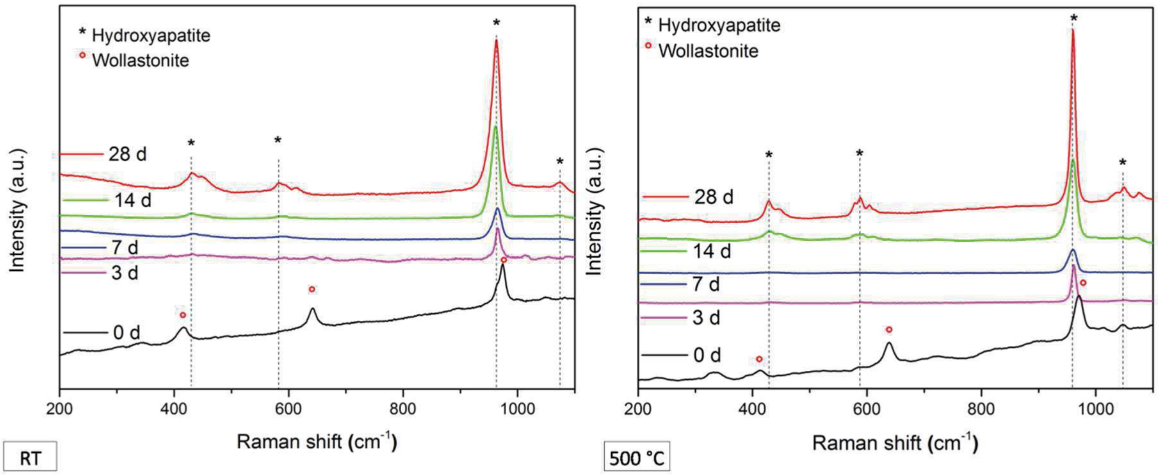

Figure 6.29: Raman spectra registered on RKKP_Mn films deposited at RT and 500°C after different immersion time points in SBF.

Table 6.10: Raman signals attributions.

Peaks Hydroxyapatite (cm^{-1})	**Assignment** [112]
429 (m), 447 (w)	$\nu_2\ PO_4^{3-}$
583 (w), 594 (w), 615 (vw)	$\nu_4\ PO_4^{3-}$
963 (s)	$\nu_1\ PO_4^{3-}$
1075 (vw)	$\nu_3\ PO_4^{3-}$
Peaks wollastonite (cm^{-1})	**Assignment** [70,181]
415 (m)	δ SiOSi and δ OSiO
641 (m)	ν_s SiOSi
973 (s)	ν_{as} SiOSi

where vw denotes: very weak, w: weak, m: medium and s: strong.

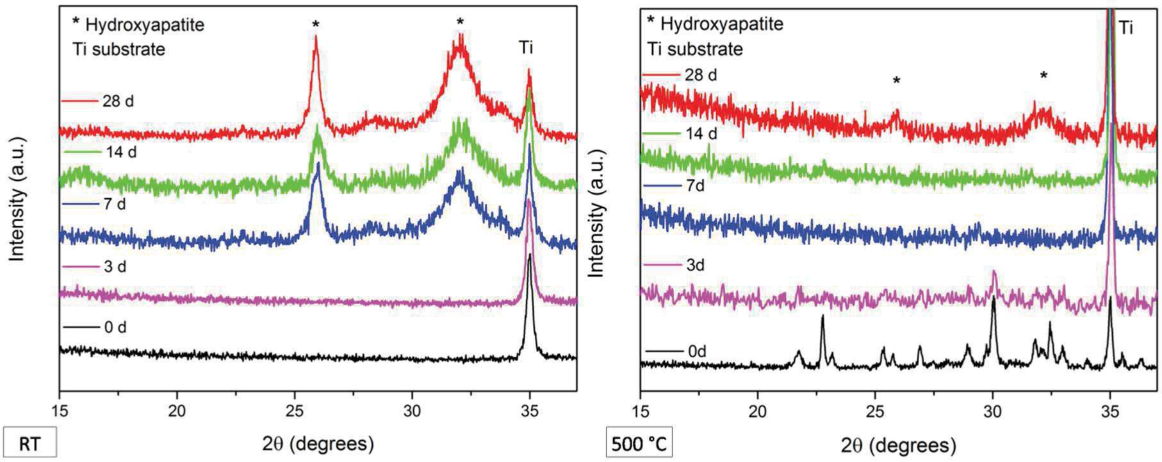

Figure 6.30: ADXRD patterns of RKKP_Mn films deposited at RT and 500°C after different immersion time points in SBF.

On the other hand, in the two ADXRD spectra it is possible to reveal how the film deposited at RT (amorphous) is more bioactive than the one deposited at 500 °C (crystalline). In fact, if for the film deposited at RT a multicrystalline apatite phase is already detectable after three days of soaking, in the case of the more crystalline film (deposited at 500 °C) apatite signals are detectable only after 28 days of soaking. These results do not mean that the crystalline films are not bioactive, but that their bioactivity is slower. Moreover, since ADXRD is not a microscopic technique, it is difficult to detect the existence of small crystalline domains. However crystalline domains should be present on the soaked film deposited at 500 °C, at least after one or two weeks of immersion, as micro-Raman analysis suggests.

The corresponding SEM images are shown in Figure 6.31. A careful observation of the two sequences, suggest that the dissolution of the film deposited at 500 °C and the subsequent apatite growth are slowed down of about 1 week with respect to that of the films deposited at RT. In the case of the film deposited at RT, evident film's dissolution features are visible after only three days of immersion, the typical cauliflower morphology is visible after 7 days, confirming both Raman and XRD results, and after 28 days a second apatite crystallization has occurred. While for the coating deposited at 500 °C the films dissolution is evident after 7 days, the apatite crystallization is visible only after 14 days, and definitely no further apatite crystallizations are detectable after 28 days of immersion. These results are not surprising, since a less crystalline silicate network facilitates the ions exchange between the film and the SBF.

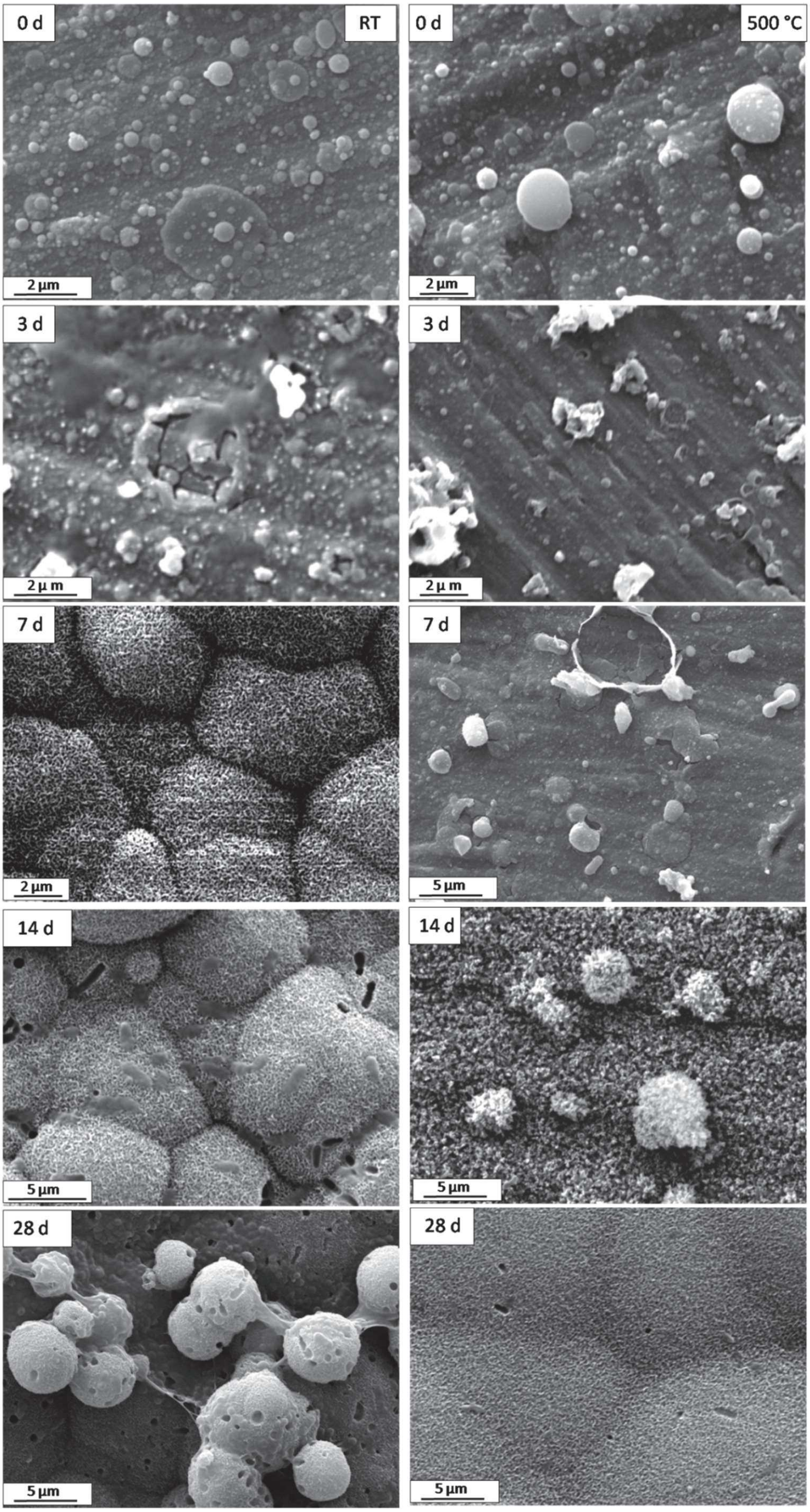

Figure 6.31: SEM images collected upon RKKP_Mn films deposited at RT and 500°C after different immersion time points in SBF.

To support all the investigation described so far, the changes of the film's composition have been evaluated after the immersion tests by the means of EDX technique. In particular, the decreasing of the silicon percentage, which is the main component of the glass-ceramic, and the increasing of calcium and phosphorus amounts, which are the principals components of the hydroxyapatite, have been evaluated. The synthetic hydroxyapatite is characterized by a specific Ca/P atomic ratio, which is 1.67. In the case of hydroxyapatite formed in physiological condition, defects in the crystalline structure are expected. In particular, if bivalent cations are present, like Na^{2+} or Mg^{2+}, they can substitute the Ca^{2+} in the hydroxyapatite apatite structure. The result is a multicrystalline apatite, like that observed in the XRD pattern in Figure 6.30 [150,151], similar to the biological apatite. Nevertheless, in this case the correct atomic ratio to be considered is (Na+Mg+Ca)/P.

Table 6.11: EDX measurements on the films deposited at RT, at different SBF soaking time points, all the data are reported in wt %, last column is an atomic ratio.

Element / Soak. d	**O**	**Na**	**Mg**	**Si**	**P**	**Ca**	**Mn**	**(Na+Mg+Ca)/P**
0 d	32.2	2.0	2.6	24.0	12.0	25.2	2.1	
3 d	34.4	3.7	4.2	12.8	25.0	15.7	4.1	
7 d	24.2	1.4	2.0	0.8	26.1	41.2	1.3	1.4
14 d	22.9	1.0	1.6	1.2	26.7	45.6	1.1	1.5
28 d	23.0	1.7	1.6	1.5	25.4	46.0	1.0	1.6

Table 6.12: EDX measurements on the films deposited at 500 °C, at different SBF soaking time points, all the data are reported in wt %, last column is an atomic ratio.

Element / Soak. d	**O**	**Na**	**Mg**	**Si**	**P**	**Ca**	**Mn**	**(Na+Mg+Ca)/P**
0 d	38.0	1.1	1.8	23.3	4.0	29.0	1.4	
3 d	55.2	3.7	4.3	18.2	7.7	8.5	2.3	
7 d	53.9	2.6	1.4	19.2	3.9	18.0	1.0	
14 d	47.4	0.6	2.3	4.2	15.6	28.0	1.9	1.6
28 d	38.2	1.1	1.3	1.2	19.9	38.2	<0.1	1.6

From the two tables (6.11 and 6.12) the ion dissolution in function of the soaking time - follows the predicted trend for both sets of samples: the initial lost of silicon is followed by the increasing of calcium and phosphate percentage. The (Na+Mg+Ca)/P atomic ratio, calculated for the samples where hydroxyapatite (more or less substituted) has been detected, gives a further confirmation of the bioactive behaviour of the films.

Given all these results, it is possible to assert that the new RKKP_Mn glass-ceramic composition is a biocompatible materials, with suitable use for the coating of hard tissue implants. The PLD at two different substrate temperature, RT and 500 °C, allows the production of amorphous or crystalline films, respectively. The in vitro bioactivity assessment suggests that, although both the films lead to the formation of an apatite layer after the soaking in SBF, the one produced at RT gives a faster crystallization of the apatite layer. On the other hand, the use of more crystalline coatings provides better mechanical properties [31,183].

Conclusions

Although the production of hard-tissue implants is a well-established practice, there are still problems related to revision surgeries or, in the worst scenario, the implants failure. Therefore, researches are working on the improvement of prosthesis performances.

The goal of this research project has been the deposition of film coatings of new-generation biomaterials, suitable for bone-related implants. In particular, the main materials of all the coatings belong to the class of bioceramics. For each material, attempts have been made in order to exploit the potentialities and overcome the weaknesses.

Hydroxyapatite has been deposited with IONPs (iron oxide nanoparticles). Despite its high biocompatibility, hydroxyapatite shows low bioactivity. Moreover, the presence of magnetite NPs are shown to encourage HAp nuclei formation due to electrostatic interactions in SBF solution. In addition, magnetized HAp coatings can be used as support matrix for cells delivery, for a remote magnetic controlled bone regeneration. The IONPs introduced into the coating have been obtained with a really "green" technique, the PLAL (pulsed laser ablation in liquid), since only an iron target and water have been used for their production. The obtaining of HAp/IONPs films has demonstrated how PLD is a successful deposition technique for the production of magnetic composite coatings. Further assessments should be executed in order to prove the biological activity of such films and the possibility to use them as magnetic support for cells delivery for remote magnetic controlled bone regeneration.

BG_Cu films have been also successfully deposited trough PLD and their bioactivity has been demonstrated by the hydroxyapatite growth on their surface during the soaking in simulated body fluid (SBF). The use of electrophoretic deposition (EPD) has allowed the coating of SS substrate with polymer/bioglass composite films, which cannot be accomplished by the conventional PLD. Also in this case a Cu-doped bioaglass has been used together with a protein-based polymer, zein, and the films bioactivity has been proved.

RKKP is a bioglass-ceramic composed mainly by hydroxyapatite and wollastonite crystalline phases. Since the biocompatibility of RKKP films deposited by PLD was been already proved in previous work [166], some modifications have been carried out in order to improve their performances. Moreover, RKKP pulsed laser deposited has been proved functional coatings for cell-delivery implantation and for the reduction of the corrosion of biodegradable implant. Although glass-ceramics show superior mechanical properties than bioglasses, they are still not enough for load-bearing application. Therefore, RKKP&C_{60} has been used as target for the deposition of composite films with improved hardness. Finally, RKKP has been modified by the adding of another component, manganese, useful for the bone regeneration, and its biocompatibility has been proved. The films deposited at both the deposition temperature, i.e. room temperature and 500 °C, have been demonstrated bioactive, even though they are characterized by different crystalline degrees. However the less crystalline one has shown a faster apatite crystallization in SBF.

References

[1] P.D. United Nations, Department of Economic and Social Affairs, World population ageing, New York, 2015.

[2] W.M. Thomson, S. Ma, An ageing population poses dental challenges, Singapore Dent. J. 35 (2014) 3–8.

[3] US Department of Health and Human Services, Bone health and osteoporosis: a report of the Surgeon General, 2004.

[4] P.M. Galletti, J.W. Boretos, Report on the Consensus Development Conference on "Clinical Applications of Biomaterials," 1–3 November 1983, J. Biomed. Mater. Res. 17 (1983) 539–555.

[5] D.F. Williams, Definitions in biomaterials: proceedings of a consensus conference of the European Society for Biomaterials, Elsevier, Amsterdam ;, 1987.

[6] "SECOND CONSENSUS CONFERENCE ON DEFINITIONS IN BIOMATERIALS", Biomed. Mater. Int. Newsletters. (1991).

[7] B.D. Ratner, A History of Biomaterials, in: Biomater. Sci. An Introd. to Mater. Third Ed., 2013: pp. xli–liii.

[8] H.F. Hildebrand, Biomaterials - a history of 7000 years, BioNanoMaterials. 14 (2013) 119–133.

[9] M. Colakis, M.J. Masello, "Tantalum". Classical Mythology & More: A Reader Workbook, 2007.

[10] V. Migonney, History of Biomaterials, Biomaterials. (2014) 1–10.

[11] P.I. Brånemark, U. Breine, B. Johansson, P.J. Roylance, H. Röckert, J.M. Yoffey, Regeneration of bone marrow, Cells Tissues Organs. 59 (1964) 1–46.

[12] B.D. Ratner, A.S. Hoffman, F.J. Schoen, J.E. Lemons, Biomaterials Science - An Introduction to Materials in Medicine, First Edit, Academic Press, San Diego, 1996. doi:10.1016/B978-0-08-087780-8.00148-0.

[13] B.D. Ratner, A.S. Hoffman, F.J. Schoen, J.E. Lemons, Introduction - Biomaterials Science: An Evolving, Multidisciplinary Endeavor, Third Edit, Elsevier, 2013.

[14] S.R. Paital, N.B. Dahotre, Calcium phosphate coatings for bio-implant applications: Materials, performance factors, and methodologies, Mater. Sci. Eng. R Reports. 66 (2009) 1–70.

[15] L.L. Hench, S.M. Best, Ceramics, Glasses, and Glass-Ceramics: Basic Principles, in: Biomater. Sci. An Introd. to Mater. Third Ed., Third Edit, Elsevier, 2013: pp. 128–151.

[16] S. Schaefer, R. Detsch, F. Uhl, U. Deisinger, G. Ziegler, How degradation of calcium phosphate bone substitute materials is influenced by phase composition and porosity, Adv. Eng. Mater. 13 (2011) 342–350.

[17] X.N. Gu, S.S. Li, X.M. Li, Y.B. Fan, Magnesium based degradable biomaterials: A review, Front. Mater. Sci. 8 (2014) 200–218.

[18] S. V. Dorozhkin, Calcium orthophosphate coatings on magnesium and its biodegradable alloys, Acta Biomater. 10 (2014) 2919–2934.

[19] T.J. Blokhuis, Bioresorbable bone graft substitutes, in: Bone Substit. Biomater., Elsevier Inc., 2014: pp. 80–92.

[20] S.R. Levitt, P.H. Crayton, E.A. Monroe, R.A. Condrate, Forming method for apatite prostheses, J. Biomed. Mater. Res. 3 (1969) 683–684.

[21] K. Lin, Y. Zhou, Y. Zhou, H. Qu, F. Chen, Y. Zhu, J. Chang, Biomimetic hydroxyapatite porous microspheres with co-substituted essential trace elements: Surfactant-free hydrothermal synthesis, enhanced degradation and drug release, J. Mater. Chem. 21 (2011) 16558-16565.

[22] M. Avci, B. Yilmaz, A. Tezcaner, Z. Evis, Strontium doped hydroxyapatite biomimetic coatings on Ti6Al4V plates, Ceram. Int. 43 (2017) 9431–9436.

[23] E. El-Meliegy, R. van Noort, Glasses an Glass Ceramics for Medical Applications, Springer US, 2012.

[24] L.L. Hench, The story of Bioglass®, J. Mater. Sci. Mater. Med. 17 (2006) 967–978.

[25] L.L. Hench, R.J. Splinter, W.C. Allen, T.K. Greenlee, Bonding mechanism at the interface of ceramic prosthetic materials, J Biomed Mater Res A. 5 (1971) 117–141.

[26] L.L. Hench, Biomaterials: A forecast for the future, Biomaterials. 19 (1998) 1419–1423.

[27] K. Lin, J. Chang, Structure and properties of hydroxyapatite for biomedical applications, in: Hydroxyapatite Biomedical Applications, Elsevier Ltd., 2015: pp. 3–19.

[28] D. Arcos, Calcium Phosphate Bioceramics, in: M. Vallet-Regí (Ed.), Bio-Ceramics with Clinical Applications, Wiley, 2014: pp. 23–71.

[29] H. Begam, B. Kundu, A. Chanda, S.K. Nandi, MG63 osteoblast cell response on Zn doped hydroxyapatite (HAp) with various surface features, Ceram. Int. 43 (2017) 3752–3760.

[30] B. Ben-Nissan, A.H. Choi, R. Roest, B.A. Latella, A. Bendavid, Adhesion of hydroxyapatite on titanium medical implants, in: Hydroxyapatite Biomedical Applications, Elsevier Ltd., 2015: pp. 21–51.

[31] D.S. Brauer, Bioactive Glasses — Structure and Properties, Angew. Chem. Int. Ed. 54 (2015) 4160–4181.

[32] J.E. Shelby, Introduction to Glass Science and Technology, Royal Society of Chemistry, Cambridge, 2005.

[33] V. FitzGerald, D.M. Pickup, D. Greenspan, G. Sarkar, J.J. Fitzgerald, K.M. Wetherall, R.M. Moss, J.R. Jones, R.J. Newport, A Neutron and X-Ray Diffraction Study of Bioglass® with Reverse Monte Carlo Modelling, Adv. Funct. Mater. 17 (2007) 3746–3753.

[34] Y. Xiang, J. Du, Effect of strontium substitution on the structure of 45S5 bioglasses, Chem. Mater. 23 (2011) 2703–2717.

[35] M.D. O'Donnell, Melt-Derived Bioactive Glass, in: J.R. Jones, A.G. Clare (Eds.), Bio-Glasses an Introduction, A John Wiley & Sons, Ltd., 2012: pp. 13–27.

[36] A. Pedone, G. Malavasi, M. Cristina Menziani, U. Segre, A.N. Cormack, Role of magnesium in soda-lime glasses: Insight into structural, transport, and mechanical properties through computer simulations, J. Phys. Chem. C. 112 (2008) 11034–11041.

[37] L.L. Hench, N. Roki, M.B. Fenn, Bioactive glasses: Importance of structure and properties in bone regeneration, J. Mol. Struct. 1073 (2014) 24–30.

[38] A. Ravaglioli, A. Krajewski, G. Baldi, F. Tateo, L. Peruzzo, A. Piancastelli, Glass–ceramic scaffolds for tissue engineering, Adv. Appl. Ceram. 107 (2008) 268–273.

[39] U. Gross, V. Strunz, The interface of various glasses and glass ceramics with a bony implantation bed, J. Biomed. Mater. Res. 19 (1985) 251–271.

[40] T. Kokubo, Bioactive glass ceramics: properties and applications, Biomaterials. 12 (1991) 155–163.

[41] M.V. Cabañas, Bio-Ceramics with Clinical Applications, John Wiley & Sons, Ltd, Chichester, UK, 2014.

[42] S. Bose, S. Tarafder, A. Bandyopadhyay, Hydroxyapatite coatings for metallic implants, in: M. Mucalo (Ed.), Hydroxyapatite Biomed. Appl., Elsevier Ltd., 2015: pp. 143–157.

[43] R.A. Gittens, T. Mclachlan, R. Olivares-navarrete, Y. Cai, S. Berner, R. Tannenbaum, Z. Schwartz, K.H. Sandhage, B.D. Boyan, Biomaterials The effects of combined micron- / submicron-scale surface roughness and nanoscale features on cell proliferation and differentiation, Biomaterials. 32 (2011) 3395–3403.

[44] B.J. Im, S.W. Lee, N. Oh, M.H. Lee, J.H. Kang, R. Leesungbok, S.C. Lee, S.J. Ahn, J.S. Park, Texture direction of combined microgrooves and submicroscale topographies of titanium substrata influence adhesion , proliferation , and differentiation in human primary cells, Arch. Oral Biol. 57 (2011) 898–905.

[45] S.E. Black, Laser Ablation : Effects and Applications, Nova Science Publishers, Inc. New York, 2011.

[46] C.W. Schneider, T. Lippert, Laser Ablation and Thin Film Deposition, in: P. Schaaf (Ed.), Laser Process. Mater. Fundam. Appl. Dev., Springer Berlin, Heidelberg, 2010: pp. 89–112.

[47] S. Fähler, H.U. Krebs, Calculations and experiments of material removal and kinetic energy during pulsed laser ablation of metals, Appl. Surf. Sci. 96–98 (1996) 61–65.

[48] A. Miotello, R. Kelly, Laser-induced phase explosion: New physical problems when a condensed phase approaches the thermodynamic critical temperature, Appl. Phys. A Mater. Sci. Process. 69 (1999) 67–73.

[49] R. Kelly, A. Miotello, A. Mele, A. Giardini Guidoni, Plume Formation and Characterization in Laser-Surface Interactions, in: R. Celotta, T. Lucatorto (Eds.), Exp. Methods Phys. Sci., Academic Press by Elsevier, 1997: pp. 225–289.

[50] D. Perez, L.J. Lewis, P. Lorazo, M. Meunier, Ablation of molecular solids under nanosecond laser pulses: The role of inertial confinement, Appl. Phys. Lett. 89 (2006) 1–3.

[51] P.R. Willmott, J.R. Huber, Pulsed laser vaporization and deposition, Rev. Mod. Phys. 72 (2000) 315–328.

[52] J.F. Seely, Quantum Theory of Inverse Bremsstrahlung Absorption and Pair Production, in: Laser Interact. Relat. Plasma Phenom., Springer US, Boston, MA, 1974: pp. 835–847.

[53] S.I. Anisimov, B.S. Luk’yanchuk, A. Luches, An analytical model for three-dimensional laser plume expansion into vacuum in hydrodynamic regime, Appl. Surf. Sci. 96–98 (1996) 24–32.

[54] D.H. Lowndes, Growth and Doping of Compound Semiconductor Films by Pulsed Laser Ablation, in: R. Celotta, T. Lucatorto (Eds.), Exp. Methods Phys. Sci., Academic Press by Elsevier, 1997: pp. 475–571.

[55] O.O. Van der Biest, L.J. Vandeperre, Electrophoretic Deposition of materials, Annu. Rev. Mater. Res. 29 (1999) 327–357.

[56] A.R. Boccaccini, S. Keim, R. Ma, Y. Li, I. Zhitomirsky, Electrophoretic deposition of biomaterials, J. R. Soc Interface. 7 (2010) S581–S613.

[57] H.C. Hamaker, Formation of a deposit by electrophoresis, Trans. Faraday Soc. 35 (1940) 279-287.

[58] P. Sarkar, P.S. Nicholson, Electrophoretic Deposition (EPD): Mechanisms, Kinetics, and Application to Ceramics, J. Am. Ceram. Soc. 79 (1996) 1987–2002. doi:10.1111/j.1151-2916.1996.tb08929.x.

[59] P.M. Biesheuvel, H. Verweij, Theory of cast formation in electrophoretic deposition, J. Am. Ceram. Soc. 82 (1999) 1451–1455.

[60] H.C. Hamaker, E.J.W. Verwey, Part II.—(C) Colloid stability. The role of the forces between the particles in electrodeposition and other phenomena, Trans. Faraday Soc. 35 (1940) 180–185.

[61] H. Koelmans, J.T.G. Overbeek, Stability and Electrophoretic Deposition ofsuspensions in non-aqueous media, Discuss. Faraday Soc. 18 (1954) 52–63.

[62] C. Stahli, M. James-Bhasin, A. Hoppe, A.R. Boccaccini, S.N. Nazhat, Effect of ion release from Cu-doped 45S5 Bioglass on 3D endothelial cell morphogenesis, Acta Biomater. 19 (2015) 15–22.

[63] T. Kokubo, H. Takadama, How useful is SBF in predicting in vivo bone bioactivity?, Biomaterials. 27 (2006) 2907–2915.

[64] Q. Chen, S. Cabanas-Polo, O.M. Goudouri, A.R. Boccaccini, Electrophoretic co-deposition of polyvinyl alcohol (PVA) reinforced alginate-Bioglass® composite coating on stainless steel: Mechanical properties and in-vitro bioactivity assessment, Mater. Sci. Eng. C. 40 (2014) 55–64.

[65] J. V. Rau, R. Teghil, M. Fosca, A. De Bonis, I. Cacciotti, A. Bianco, V.R. Albertini, R. Caminiti, A. Ravaglioli, Bioactive glass-ceramic coatings prepared by pulsed laser deposition from RKKP targets (sol-gel vs melt-processing route), Mater. Res. Bull. 47 (2012) 1130–1137.

[66] M. Lombardi, I. Cacciotti, A. Bianco, L. Montanaro, RKKP bioactive glass-ceramic material through an aqueous sol-gel process, Ceram. Int. 41 (2015) 3371–3380.

[67] M. Ledda, M. Fosca, A. De Bonis, M. Curcio, R. Teghil, M.G. Lolli, A. De Stefanis, R. Marchese, J. V. Rau, A. Lisi, Placenta Derived Mesenchymal Stem Cells Hosted on RKKP Glass-Ceramic: A Tissue Engineering Strategy for Bone Regenerative Medicine Applications, Biomed Res. Int. (2016) 1–11.

[68] I.V. Antoniac, M. Miculescu, M. Dinu, Metallurgical Characterization of some Magnesium Alloys for Medical Applications, Solid State Phenom. 188 (2012) 109–113.

[69] A. Krajewski, R. Malavolti, A. Piancastelli, Albumin adhesion on some biological and non-biological glasses and connection with their Z-potentials., Biomaterials. 17 (1996) 53–60.

[70] A. Krajewski, A. Ravaglioli, A. Tinti, P. Taddei, M. Mazzocchi, R. Martinetti, C. Fagnano, M. Fini, Comparison between the in vitro surface transformations of AP40 and RKKP bioactive glasses, J. Mater. Sci. Mater. Med. 16 (2005) 119–128.

[71] B. Jönsson, S. Hogmark, Hardness measurements of thin films, Thin Solid Films. 114 (1984) 257–269.

[72] A. Iost, R. Bigot, Hardness of coatings, Surf. Coatings Technol. 80 (1996) 117–120.

[73] A. Iost, R. Bigot, Indentation size effect: reality or artefact?, J. Mater. Sci. 31 (1996) 3573–3577.

[74] Product Information, 96992 Cell Counting Kit – 8, SIGMA-ALDRICH. (n.d.).

[75] C. Paluszkiewicz, A. Ślósarczyk, D. Pijocha, M. Sitarz, M. Bućko, A. Zima, A. Chróścicka, M. Lewandowska-Szumieł, Synthesis, structural properties and thermal stability of Mn-doped hydroxyapatite, J. Mol. Struct. 976 (2010) 301–309.

[76] C.F. Koch, S. Johnson, D. Kumar, M. Jelinek, D.B. Chrisey, A. Doraiswamy, C. Jin, R.J. Narayan, I.N. Mihailescu, Pulsed laser deposition of hydroxyapatite thin films, Mater. Sci. Eng. C. 27 (2007) 484–494.

[77] G.P. Dinda, J. Shin, J. Mazumder, Pulsed laser deposition of hydroxyapatite thin films on Ti-6Al-4V: Effect of heat treatment on structure and properties, Acta Biomater. 5 (2009) 1821–1830.

[78] C.M. Cotell, Pulsed laser deposition and processing of biocompatible hydroxylapatite thin films, Appl. Surf. Sci. 69 (1993) 140–148.

[79] G. Socol, A.M. Macovei, F. Miroiu, N. Stefan, L. Duta, G. Dorcioman, I.N. Mihailescu, S.M. Petrescu, G.E. Stan, D.A. Marcov, A. Chiriac, I. Poeata, Hydroxyapatite thin films synthesized by pulsed laser deposition and magnetron sputtering on PMMA substrates for medical applications, Mater. Sci. Eng. B Solid-State Mater. Adv. Technol. 169 (2010) 159–168.

[80] T.D. Schladt, K. Schneider, H. Schild, W. Tremel, Synthesis and bio-functionalization of magnetic nanoparticles for medical diagnosis and treatment., Dalton Trans. 40 (2011) 6315–43.

[81] A.M. Derfus, G. Von Maltzahn, T.J. Harris, T. Duza, K.S. Vecchio, E. Ruoslahti, S.N. Bhatia, Remotely triggered release from magnetic nanoparticles, Adv. Mater. 19 (2007) 3932–3936.

[82] C.S.S.R. Kumar, F. Mohammad, Magnetic nanomaterials for hyperthermia-based therapy and controlled drug delivery, Adv. Drug Deliv. Rev. 63 (2011) 789–808.

[83] H. Gu, K. Xu, C. Xu, B. Xu, Biofunctional magnetic nanoparticles for protein separation and pathogen detection, Chem. Commun. (2006) 941–949.

[84] L. Wang, H. Ji, S. Wang, Y. Li, X. Jiang, G. Yang, Ultrasonic-assisted synthesis of amorphous Fe3O4 with a high specific surface area and improved capacitance for supercapacitor, Nanoscale. 5 (2013) 3793–3799.

[85] R. Qiao, C. Yang, M. Gao, Superparamagnetic iron oxide nanoparticles: from preparations to in vivo MRI applications, J. Mater. Chem. 19 (2009) 6274-6293.

[86] P. Qiu, C. Jensen, N. Charity, R. Towner, C. Mao, Oil phase evaporation-induced self-assembly of hydrophobic nanoparticles into spherical clusters with controlled surface chemistry in an oil-in-water dispersion and comparison of behaviors of individual and clustered iron oxide nanoparticles, J. Am. Chem. Soc. 132 (2010) 17724–17732.

[87] Q. Chang, D.L. Chen, H.Q. Ru, X.Y. Yue, L. Yu, C.P. Zhang, Toughening mechanisms in iron-containing hydroxyapatite/titanium composites, 31 (2010) 1493–1501.

[88] O. Kaygili, S. V. Dorozhkin, T. Ates, A.A. Al-Ghamdi, F. Yakuphanoglu, Dielectric properties of Fe doped hydroxyapatite prepared by sol-gel method, Ceram. Int. 40 (2014) 9395–9402.

[89] S. Panseri, C. Cunha, T. D'Alessandro, M. Sandri, G. Giavaresi, M. Marcacci, C.T. Hung, A. Tampieri, Intrinsically superparamagnetic Fe-hydroxyapatite nanoparticles positively influence osteoblast-like cell behaviour, J. Nanobiotechnology. 10 (2012) 32, 1–10.

[90] U. Anjaneyulu, U. Vijayalakshmi, Preparation and characterization of novel sol-gel derived hydroxyapatite/Fe3O4 composites coatings on Ti-6Al-4V for biomedical applications, Mater. Lett. 189 (2017) 118–121.

[91] L.J. Santos, R.L. Reis, M.E. Gomes, Harnessing magnetic-mechano actuation in regenerative medicine and tissue engineering, Trends Biotechnol. 33 (2015) 471–479.

[92] D. Ling, T. Hyeon, Chemical design of biocompatible iron oxide nanoparticles for medical applications, Small. 9 (2013) 1450–1466.

[93] V. Amendola, P. Riello, S. Polizzi, S. Fiameni, C. Innocenti, C. Sangregorio, M. Meneghetti, Magnetic iron oxide nanoparticles with tunable size and free surface obtained via a "green" approach based on laser irradiation in water, J. Mater. Chem. 21 (2011) 18665–18673.

[94] A. De Bonis, A. Galasso, N. Ibris, A. Laurita, A. Santagata, R. Teghil, Rutile microtubes assembly from nanostructures obtained by ultra-short laser ablation of titanium in liquid, Appl. Surf. Sci. 268 (2013) 571–578.

[95] S. Scaramuzza, S. Agnoli, V. Amendola, Metastable alloy nanoparticles, metal-oxide nanocrescents and nanoshells generated by laser ablation in liquid solution: influence of the chemical environment on structure and composition, Phys. Chem. Chem. Phys. 17 (2015) 28076–28087.

[96] G.W. Yang, Nanodiamonds from laser ablation in liquid, laser ablation: effects and applications, in: S.E. Black (Ed.), Laser Ablation Eff. Appl., Nova Science Publisher, Inc., New York, 2011: pp. 227–265.

[97] A. De Bonis, M. Sansone, L. D 'alessio, A. Galasso, A. Santagata, R. Teghil, Dynamics of laser-induced bubble and nanoparticles generation during ultra-short laser ablation of Pd in liquid, J. Phys. D Appl. Phys. 46 (2013) 445301–9.

[98] A. Kanitz, J.S. Hoppius, M. del Mar Sanz, M. Maicas, A. Ostendorf, E.L. Gurevich, Synthesis of Magnetic Nanoparticles by Ultrashort Pulsed Laser Ablation of Iron in Different Liquids, ChemPhysChem. 18 (2017) 1155–1164.

[99] A. De Bonis, T. Lovaglio, A. Galasso, A. Santagata, R. Teghil, Iron and iron oxide nanoparticles obtained by ultra-short laser ablation in liquid, Appl. Surf. Sci. 353 (2015) 433–438.

[100] V. Amendola, P. Riello, M. Meneghetti, Magnetic Nanoparticles of Iron Carbide , Iron Oxide , Iron @ Iron Oxide , and Metal Iron Synthesized by Laser Ablation in Organic Solvents, J. Phys. Chem. C. 115 (2011) 5140–5146.

[101] P. Liu, W. Cai, H. Zeng, Fabrication and size-dependent optical properties of FeO nanoparticles induced by laser ablation in a liquid medium, J. Phys. Chem. C. 112 (2008) 3261–3266.

[102] L. Wang, J. Li, Z. Wang, L. Zhao, Q. Jiang, Low-temperature hydrothermal synthesis of α-Fe/Fe3O4 nanocomposite for fast Congo red removal., Dalt. Trans. 42 (2013) 2572–2579.

[103] L. Zhang, Y.H. Dou, H.C. Gu, Sterically induced shape control of magnetite nanoparticles, J. Cryst. Growth. 296 (2006) 221–226.

[104] M. Darbandi, F. Stromberg, J. Landers, N. Reckers, B. Sanyal, W. Keune, H. Wende, Nanoscale size effect on surface spin canting in iron oxide nanoparticles synthesized by the microemulsion method, J. Phys. D. Appl. Phys. 45 (2012) 195001-12.

[105] A.M. Jubb, H.C. Allen, Vibrational spectroscopic characterization of hematite, maghemite, and magnetite thin films produced by vapor deposition, ACS Appl. Mater. Interfaces. 2 (2010) 2804–2812.

[106] C. Mossaad, M.C. Tan, M. Starr, E.A. Payzant, J.Y. Howe, R.E. Riman, Size-dependent crystalline to amorphous uphill phase transformation of hydroxyapatite nanoparticles, Cryst. Growth Des. 11 (2011) 45–52.

[107] C. Chen, R. Chiang, H. Lai, C. Lin, Characterization of Monodisperse Wüstite Nanoparticles following Partial Oxidation, J. Phys. Chem. C. 114 (2010) 4258–4263.

[108] A. De Bonis, M. Curcio, M. Fosca, I. Cacciotti, A. Santagata, R. Teghil, J. V Rau, RBP1 bioactive glass-ceramic fi lms obtained by Pulsed Laser Deposition, Mater. Lett. 175 (2016) 195–198.

[109] M. Curcio, A. De Bonis, M. Fosca, A. Santagata, R. Teghil, J. V. Rau, Pulsed laser-deposited composite carbon-glass-ceramic films with improved hardness, J. Mater. Sci. 52 (2017) 9140–9150.

[110] S. Lumetti, E. Manfredi, S. Ferraris, S. Spriano, G. Passeri, G. Ghiacci, G. Macaluso, C. Galli, The response of osteoblastic MC3T3-E1 cells to micro- and nano-textured, hydrophilic and bioactive titanium surfaces, J. Mater. Sci. Mater. Med. 27 (2016) 68.

[111] S. Ferraris, a. Bobbio, M. Miola, S. Spriano, Micro- and nano-textured, hydrophilic and bioactive titanium dental implants, Surf. Coatings Technol. 276 (2015) 374–383.

[112] A. Antonakos, E. Liarokapis, T. Leventouri, Micro-Raman and FTIR studies of synthetic and natural apatites, Biomaterials. 28 (2007) 3043–3054.

[113] A. Klini, A. Manousaki, D. Anglos, C. Fotakis, Growth of ZnO thin films by ultraviolet pulsed-laser ablation: Study of plume dynamics, J. Appl. Phys. 98 (2005) 1–8.

[114] M.N.R. Ashfold, F. Claeyssens, G.M. Fuge, S.J. Henley, Pulsed laser ablation and deposition of thin films, Chem. Soc. Rev. 33 (2004) 23–31.

[115] G. Cristoforetti, A. De Giacomo, M. Dell'Aglio, S. Legnaioli, E. Tognoni, V. Palleschi, N. Omenetto, Local Thermodynamic Equilibrium in Laser-Induced Breakdown Spectroscopy: Beyond the McWhirter criterion, Spectrochim. Acta - Part B At. Spectrosc. 65 (2010) 86–95.

[116] H.M. Griem, Principles of Plasma Spectroscopy, Cambrige University Press, Cambrige, 1997.

[117] NIST: Atomic Spectra Database Lines Form, (n.d.). https://physics.nist.gov/PhysRefData/ASD/lines_form.html (accessed November 22, 2017).

[118] Y.F. Goh, A.Z. Alshemary, M. Akram, M.R. Abdul Kadir, R. Hussain, Bioactive Glass: An In-Vitro Comparative Study of Doping with Nanoscale Copper and Silver Particles, Int. J. Appl. Glas. Sci. 5 (2014) 255–266.

[119] A. Hoppe, N.S. Güldal, A.R. Boccaccini, A review of the biological response to ionic dissolution products from bioactive glasses and glass-ceramics, Biomaterials. 32 (2011) 2757–2774.

[120] N. Philips, H. Hwang, S. Chauhan, D. Leonardi, S. Gonzalez, Stimulation of Cell Proliferation and Expression of Matrixmetalloproteinase-1 and Interluekin-8 Genes in Dermal Fibroblasts by Copper Stimulation of Cell Proliferation and Expression of Matrixmetalloproteinase-1 and Interluekin-8 Genes in Dermal Fibroblas, Connect. Tissue Res. 51 (2010) 224–229.

[121] J.P. Rodriguez, S. Rios, M. Gonzalez, Modulation of the Proliferation and Differentiation of Human Mesenchymal Stem Cells by Copper, J. Cell. Biochem. 85 (2002) 92–100.

[122] A. Hoppe, R. Meszaros, C. Stähli, S. Romeis, J. Schmidt, W. Peukert, B. Marelli, S.N. Nazhat, L. Wondraczek, J. Lao, E. Jallot, A.R. Boccaccini, In vitro reactivity of Cu doped 45S5 Bioglass® derived scaffolds for bone tissue engineering, J. Mater. Chem. B. 1 (2013) 5659–5674.

[123] I. Cacciotti, Bivalent cationic ions doped bioactive glasses: the influence of magnesium, zinc, strontium and copper on the physical and biological properties, J. Mater. Sci. 52 (2017) 8812–8831.

[124] L. Milkovic, A. Hoppe, R. Detsch, A.R. Boccaccini, N. Zarkovic, Effects of Cu-doped 45S5 bioactive glass on the lipid peroxidation-associated growth of human osteoblast-like cells *in vitro*, J. Biomed. Mater. Res. Part A. 102 (2014) 3556–3561.

[125] Z. Song, L. Borgwardt, N. Høiby, H. Wu, T.S. Sørensen, A. Borgwardt, Prosthesis infections after orthopedic joint replacement : the possible role of bacterial biofilms, Orthop. Rev. (Pavia). 5 (2013) 65–71.

[126] E. Wers, B. Lefeuvre, New hybrid agarose/Cu-Bioglass® biomaterials for antibacterial coatings, Korean J. Chem. Eng. 34 (2017) 2241–2247.

[127] K. Zheng, X. Dai, M. Lu, N. Hüser, N. Taccardi, A.R. Boccaccini, Synthesis of copper-containing bioactive glass nanoparticles using a modified Stöber method for biomedical applications, Colloids Surfaces B Biointerfaces. 150 (2017) 159–167.

[128] A.A. El-rashidy, J.A. Roether, L. Harhaus, U. Kneser, A.R. Boccaccini, Acta Biomaterialia Regenerating bone with bioactive glass scaffolds : A review of in vivo studies in bone defect models, Acta Biomater. 62 (2017) 1–28.

[129] L. Rusen, S. Brajnicov, P. Neacsu, V. Marascu, A. Bonciu, M. Dinescu, V. Dinca, A. Cimpean, Novel degradable biointerfacing nanocomposite coatings for modulating the osteoblast response, Surf. Coatings Technol. 325 (2017) 397–409.

[130] A. Luches, A.P. Caricato, Fundamentals and Applications of MAPLE, in: A. Miotello, P. Ossi (Eds.), Laser-Surface Interact. New Mater. Prod., Springer, Berlin, Heidelberg, 2010: pp. 203–233.

[131] A.R. Boccaccini, C. Peters, J.A. Roether, D. Eifler, S.K. Misra, E.J. Minay, Electrophoretic deposition of polyetheretherketone (PEEK) and PEEK/Bioglass® coatings on NiTi shape memory alloy wires, J. Mater. Sci. 41 (2006) 8152–8159.

[132] D. Zhitomirsky, J.A. Roether, A.R. Boccaccini, I. Zhitomirsky, Electrophoretic deposition of bioactive glass/polymer composite coatings with and without HA nanoparticle inclusions for biomedical applications, J. Mater. Process. Technol. 209 (2009) 1853–1860.

[133] F. Pishbin, A. Simchi, M.P. Ryan, A.R. Boccaccini, Electrophoretic deposition of chitosan/45S5 Bioglass® composite coatings for orthopaedic applications, Surf. Coatings Technol. 205 (2011) 5260–5268.

[134] T. Moskalewicz, S. Seuss, A.R. Boccaccini, Microstructure and properties of composite polyetheretherketone/ Bioglass® coatings deposited on Ti-6Al-7Nb alloy for medical applications, Appl. Surf. Sci. 273 (2013) 62–67.

[135] S. Clavijo, F. Membrives, G. Quiroga, A.R. Boccaccini, M.J. Santillán, Electrophoretic Deposition of Chitosan/Bioglass® and Chitosan/Bioglass®/TiO2 Composite Coatings for Bioimplants, Ceram. Int. 42 (2016) 14206–14213.

[136] A.L.B. Maçon, T.B. Kim, E.M. Valliant, K. Goetschius, R.K. Brow, D.E. Day, A. Hoppe, A.R. Boccaccini, I.Y. ong Kim, C. Ohtsuki, T. Kokubo, A. Osaka, M. Vallet-Regí, D. Arcos, L. Fraile, A.J. Salinas, A. V. Teixeira, Y. Vueva, R.M. Almeida, M. Miola, C. Vitale-Brovarone, E. Verné, W. Höland, J.R. Jones, A unified in vitro evaluation for apatite-forming ability of bioactive glasses and their variants, J. Mater. Sci. Mater. Med. 26 (2015) 115.

[137] B.L. Hsu, Y.M. Weng, Y.H. Liao, W. Chen, Structural investigation of edible zein films/coatings and directly determining their thickness by FT-Raman spectroscopy, J. Agric. Food Chem. 53 (2005) 5089–5095.

[138] K. Indira, C. Sylvie, W. Zhongke, Z. Hongyu, Investigation of Wettability Properties of Laser Surface Modified Rare Earth Mg Alloy, Procedia Eng. 141 (2016) 63–69.

[139] J.D. Bumgardner, R. Wiser, S.H. Elder, R. Jouett, Y. Yang, J.L. Ong, Contact angle, protein adsorption and osteoblast precursor cell attachment to chitosan coatings bonded to titanium, J. Biomater. Sci. Polym. Ed. 14 (2003) 1401–1409.

[140] I. Cacciotti, M. Lombardi, L. Montanaro, Sol – gel derived 45S5 bioglass : synthesis , microstructural evolution and thermal behaviour, J Mater Sci Mater Med. 23 (2012) 1849–1866.

[141] A.R. Boccaccini, Q. Chen, L. Lefebvre, L. Gremillard, J. Chevalier, Sintering, crystallisation and biodegradation behaviour of Bioglass-derived glass-ceramics., Faraday Discuss. 136 (2007) 27–44.

[142] L. Lefebvre, J. Chevalier, L. Gremillard, R. Zenati, G. Thollet, D. Bernache-Assolant, A. Govin, Structural transformations of bioactive glass 45S5 with thermal treatments, Acta Mater. 55 (2007) 3305–3313.

[143] O. Bretcanu, X. Chatzistavrou, K. Paraskevopoulos, R. Conradt, I. Thompson, A.R. Boccaccini, Sintering and crystallisation of 45S5 Bioglass® powder, J. Eur. Ceram. Soc. 29 (2009) 3299–3306.

[144] L. Lefebvre, L. Gremillard, J. Chevalier, R. Zenati, D. Bernache-Assolant, Sintering behaviour of 45S5 bioactive glass, Acta Biomater. 4 (2008) 1894–1903.

[145] E.P. Erasmus, O.T. Johnson, I. Sigalas, J. Massera, Effects of Sintering Temperature on Crystallization and Fabrication of Porous Bioactive Glass Scaffolds for Bone Regeneration, Sci. Rep. 7 (2017) 1–12.

[146] O.P. Filho, G.P. Latorre, L.L. Hench, Effect of crystallization on apatite-layer formation of bioactive glass 45S5, J. Biomed. Mater. Res. 30 (1996) 509–514.

[147] C.C. Lin, L.C. Huang, P. Shen, Na2CaSi2O6-P2O5 based bioactive glasses. Part 1: Elasticity and structure, J. Non. Cryst. Solids. 351 (2005) 3195–3203.

[148] N. Zotov, I. Ebbsjö, D. Timpel, H. Keppler, Calculation of Raman spectra and vibrational properties of silicate glasses: Comparison between between Na2Si4O9 and SiO_2 glasses, Phys. Rev. B. 60 (1999) 6383–6397.

[149] J. V. Rau, I. Antoniac, M. Fosca, A. De Bonis, A.I. Blajan, C. Cotrut, V. Graziani, M. Curcio, A. Cricenti, M. Niculescu, M. Ortenzi, R. Teghil, Glass-ceramic coated Mg-Ca alloys for biomedical implant applications, Mater. Sci. Eng. C. 64 (2016) 362–369.

[150] A. Farzadi, F. Bakhshi, M. Solati-Hashjin, M. Asadi-Eydivand, N.A.A. Osman, Magnesium incorporated hydroxyapatite: Synthesis and structural properties characterization, Ceram. Int. 40 (2014) 6021–6029. .

[151] J. Sang Cho, S.H. Um, D. Su Yoo, Y.C. Chung, S. Hye Chung, J.C. Lee, S.H. Rhee, Enhanced osteoconductivity of sodium-substituted hydroxyapatite by system instability, J. Biomed. Mater. Res. - Part B Appl. Biomater. 102 (2014) 1046–1062.

[152] A.B.H. Yoruç, A. Aydınoğlu, The precursors effects on biomimetic hydroxyapatite ceramic powders, Mater. Sci. Eng. C. 75 (2017) 934–946.

[153] S.B. Goodman, Z. Yao, M. Keeney, F. Yang, The future of biologic coatings for orthopaedic implants, Biomaterials. 34 (2013) 3174–3183.

[154] N.J. Shah, J. Hong, M.N. Hyder, P.T. Hammond, Osteophilic multilayer coatings for accelerated bone tissue growth, Adv. Mater. 24 (2012) 1445–1450.

[155] R. Shukla, M. Cheryan, Zein: The industrial protein from corn, Ind. Crops Prod. 13 (2001) 171–192.

[156] R. Paliwal, S. Palakurthi, Zein in controlled drug delivery and tissue engineering, J. Control. Release. 189 (2014) 108–122.

[157] E. Corradini, E.S. De Medeiros, A.J.F. Carvalho, A.A.S. Curvelo, L.H.C. Mattoso, Mechanical and morphological characterization of starch/zein blends plasticized with glycerol, J. Appl. Polym. Sci. 101 (2006) 4133–4139.

[158] E. Corradini, P.S. Curti, A.B. Meniqueti, A.F. Martins, A.F. Rubira, E.C. Muniz, Recent advances in food-packing, pharmaceutical and biomedical applications of zein and zein-based materials, Int. J. Mol. Sci. 15 (2014) 22438–22470.

[159] S. Kaya, A.R. Boccaccini, Electrophoretic deposition of zein coatings, J. Coatings Technol. Res. 14 (2017) 683–689.

[160] J.H. Dickerson, A.R. Boccaccini, Electrophoretic deposition of nanomaterials, Springer, 2012.

[161] P. Torricelli, M. Fini, G. Giavaresi, M. Rocca, G. Pierini, R. Giardino, Isolation and characterization of osteoblast cultures from normal and osteopenic sheep for biomaterials evaluation, J. Biomed. Mater. Res. 52 (2000) 177–182.

[162] Å. Rosengren, S. Oscarsson, M. Mazzocchi, A. Krajewski, A. Ravaglioli, Protein adsorption onto two bioactive glass-ceramics, Biomaterials. 24 (2003) 147–155.

[163] M. Mattioli Belmonte, A. De Benedittis, R.A.A. Muzzarelli, P. Mengucci, G. Biagini, M.G. Gandolfi, C. Zucchini, A. Krajewski, A. Ravaglioli, E. Roncari, M. Fini, R. Giardino, Bioactivity modulation of bioactive materials in view of their application in osteoporotic patients, J. Mater. Sci. Mater. Med. 9 (1998) 485–492.

[164] M. Fini, G. Giavaresi, P. Torricelli, a Krajewski, a Ravaglioli, M.M. Belmonte, G. Biagini, R. Giardino, Biocompatibility and osseointegration in osteoporotic bone., J. Bone Joint Surg. Br. 83 (2001) 139–43.

[165] M. Montazerian, E. Dutra Zanotto, History and trends of bioactive glass-ceramics, J. Biomed. Mater. Res. - Part A. 104 (2016) 1231–1249.

[166] M. Ledda, A. De Bonis, F.R. Bertani, I. Cacciotti, R. Teghil, M.G. Lolli, A. Ravaglioli, A. Lisi, J. V Rau, Interdisciplinary approach to cell-biomaterial interactions: biocompatibility and cell friendly characteristics of RKKP glass-ceramic coatings on titanium., Biomed. Mater. 10 (2015) 35005.

[167] L. da Silva Meirelles, A.M. Fontes, D.T. Covas, A.I. Caplan, Mechanisms involved in the therapeutic properties of mesenchymal stem cells, Cytokine Growth Factor Rev. 20 (2009) 419–427.

[168] A. Toda, M. Okabe, T. Yoshida, T. Nikaido, The potential of amniotic membrane/amnion-derived cells for regeneration of various tissues., J. Pharmacol. Sci. 105 (2007) 215–228.

[169] H. Petite, V. Viateau, W. Bensaïd, A. Meunier, C. de Pollak, M. Bourguignon, K. Oudina, L. Sedel, G. Guillemin, Tissue-engineered bone regeneration, Nat. Biotechnol. 18 (2000) 959–963.

[170] G. Kaur, O.P. Pandey, K. Singh, D. Homa, B. Scott, G. Pickrell, Review Article A review of bioactive glasses : Their structure , properties , fabrication , and apatite formation, J Biomed Mater Res A. 102A (2014) 254–274.

[171] D. Ferro, S.M. Barinov, J. V. Rau, R. Teghil, A. Latini, Calcium phosphate and fluorinated calcium phosphate coatings on titanium deposited by Nd:YAG laser at a high fluence, Biomaterials. 26 (2005) 805–812.

[172] R.B. Maccioni, V. Cambiazo, Role of microtubule-associated proteins in the control of microtubule assembly., Physiol. Rev. 75 (1995) 835–64.

[173] X.N. Gu, Y.F. Zheng, A review on magnesium alloys as biodegradable materials, Front. Mater. Sci. China. 4 (2010) 111–115.

[174] M. Salahshoor, Y. Guo, Biodegradable orthopedic magnesium-calcium (MgCa) alloys, processing, and corrosion performance, Materials (Basel). 5 (2012) 135–155.

[175] G. Song, Control of biodegradation of biocompatable magnesium alloys, Corros. Sci. 49 (2007) 1696–1701. doi:10.1016/j.corsci.2007.01.001.

[176] Y.F. Zheng, X.N. Gu, F. Witte, Biodegradable metals, Mater. Sci. Eng. R. 77 (2014) 1–34.

[177] A.-I. Blajan, F. Miculescu, I. Ciuca, C. Cotrut, A. Semenescu, I. Antoniac, Effect of calcium content on the microstructure and degradation of Mg-Ca binary alloys potentially used as orthopedic biomaterials, Key Eng. Mater. 638 (2014) 104–108.

[178] M. Salahshoor, Y.B. Guo, Biodegradation control of magnesium-calcium biomaterial via adjusting surface integrity by synergistic cutting-burnishing, Procedia CIRP. 13 (2014) 143–149.

[179] Z. Li, X. Gu, S. Lou, Y. Zheng, The development of binary Mg-Ca alloys for use as biodegradable materials within bone, Biomaterials. 29 (2008) 1329–1344.

[180] R. Palanivelu, A. Ruban Kumar, Synthesis, characterization, in vitro anti-proliferative and hemolytic activity of hydroxyapatite, Spectrochim. Acta - Part A Mol. Biomol. Spectrosc. 127 (2014) 434–438.

[181] P. Richet, B.O. Mysen, J. Ingrin, High-temperature X-ray diffraction and Raman spectroscopy of diopside and pseudowollastonite, Phys. Chem. Miner. 25 (1998) 401–414.

[182] J. Ma, C.Z. Chen, D.G. Wang, X.G. Meng, J.Z. Shi, Influence of the sintering temperature on the structural feature and bioactivity of sol – gel derived SiO_2 – CaO–P_2O_5 bioglass, Ceram. Int. 36 (2010) 1911–1916.

[183] F. Baino, C. Vitale-Brovarone, Three-dimensional glass-derived scaffolds for bone tissue engineering: Current trends and forecasts for the future, J. Biomed. Mater. Res. - Part A. 97 A (2011) 514–535.

[184] L. Grausova, J. Vacik, V. Vorlicek, V. Svorcik, P. Slepicka, P. Bilkova, M. Vandrovcova, V. Lisa, L. Bacakova, Fullerene C60 films of continuous and micropatterned morphology as substrates for adhesion and growth of bone cells, Diam. Relat. Mater. 18 (2009) 578–586.

[185] B. Zhang, Y. Wang, G. Zhai, Biomedical applications of the graphene-based materials, Mater. Sci. Eng. C. 61 (2016) 953–964.

[186] L. Bacakova, I. Kopova, L. Stankova, J. Liskova, J. Vacik, V. Lavrentiev, A. Kromka, S. Potocky, D. Stranska, Bone cells in cultures on nanocarbonbased materials for potential bone tissue engineering: A review, Phys. Status Solidi Appl. Mater. Sci. 211 (2014) 2688–2702.

[187] N. Dubey, R. Bentini, I. Islam, T. Cao, A.H. Castro Neto, V. Rosa, Graphene: A Versatile Carbon-Based Material for Bone Tissue Engineering, Stem Cells Int. 2015 (2015) 1–12. doi:10.1155/2015/804213.

[188] Y. Xie, H. Li, C. Ding, X. Zheng, K. Li, Effects of graphene plates ’ adoption on the microstructure , mechanical properties , and in vivo biocompatibility of calcium silicate coating, Int. J. Nanomedicine. 10 (2015) 3855–3863.

[189] R. Deepachitra, R. Nigam, S.D. Purohit, B.S. Kumar, T. Hemalatha, T.P. Sastry, In Vitro Study of Hydroxyapatite Coatings on Fibrin Functionalized/Pristine Graphene Oxide for Bone Grafting, Mater. Manuf. Process. 30 (2015) 804–811.

[190] C. Ashok raja, S. Balakumar, D. Durgalakshmi, R.P. George, B. Anandkumar, U. Kamachi Mudali, Reduced graphene oxide/nano-Bioglass composites: processing and super-anion oxide evaluation, RSC Adv. 6 (2016) 19657–19661.

[191] J. Liu, C. Gao, P. Feng, T. Xiao, C. Shuai, S. Peng, A bioactive glass nanocomposite scaffold toughed by multi-wall carbon nanotubes for tissue engineering, J. Ceram. Soc. Japan. 123 (2015) 485–491.

[192] G. V Andrievsky, V.K. Klochkov, A.B. Bordyuh, G.I. Dovbeshko, Comparative analysis of two aqueous- colloidal solutions of C60 fullerene with help of FTIR reflectance and UV – Vis spectroscopy, Chem. Phys. Lett. 364 (2002) 8–17.

[193] R.K. Singh, J. Narayan, Pulsed-laser evaporation technique for deposition of thin films: Physics and theoretical model, Phys. Rev. B. 41 (1990) 8844–8859.

[194] H. Porwal, S. Grasso, L. Cordero-Arias, C. Li, A.R. Boccaccini, M.J. Reece, Processing and bioactivity of 45S5 Bioglass-graphene nanoplatelets composites, J. Mater. Sci. Mater. Med. 25 (2014) 1403–1413.

[195] A.C. Ferrari, J.C. Meyer, V. Scardaci, C. Casiraghi, M. Lazzeri, F. Mauri, S. Piscanec, D. Jiang, K.S. Novoselov, S. Roth, A.K. Geim, Raman spectrum of graphene and graphene layers, Phys. Rev. Lett. 97 (2006) 187401 (1-4).

[196] J. V Rau, R. Teghil, A. De Bonis, A. Generosi, B. Paci, R. Generosi, M. Fosca, D. Ferro, V.R. Albertini, N.S. Chilingarov, Pulsed laser deposition of hard and superhard carbon thin films from C60 targets, Diam. Relat. Mater. 19 (2010) 7–14.

[197] A. V. Talyzin, S.M. Luzan, I. V Anoshkin, A.G. Nasibulin, E.I. Kauppinen, A. Dzwilewski, A. Kreta, J. Jamnik, A. Hassanien, A. Lundstedt, H. Grennberg, Hydrogen Driven Cage Unzipping of C 60 into Nano-graphenes, J. Phys. Chem. C. 118 (2014) 6504–6513.

[198] A. De Bonis, M. Curcio, A. Santagata, J. V Rau, A. Galasso, R. Teghil, Fullerene-reduced graphene oxide composites obtained by ultrashort laser ablation of fullerite in water, Appl. Surf. Sci. 336 (2015) 67–72.

[199] L. Gan, Peroxide-Mediated Selective Cleavage of [60]Fullerene Skeleton Bonds: Towards the Synthesis of Open-Cage Fulleroid $C_{55}O_5$, Chem. Rec. 15 (2015) 189–198.

[200] B. Ben-nissan, A.H. Choi, A. Bendavid, Surface & Coatings Technology Mechanical properties of inorganic biomedical thin fi lms and their corresponding testing methods, Surf. Coat. Technol. 233 (2013) 39–48.

[201] J.A. Kanis, WHO Study Group, Assessment of fracture risk and its application to screening for postmenopausal osteoporosis: Synopsis of a WHO report, Osteoporos. Int. 4 (1994) 368–381. doi:10.1007/BF01622200.

[202] Consensus development conference: Diagnosis, prophylaxis, and treatment of osteoporosis, Am. J. Med. 94 (1993) 646–650.

[203] C.W. Asling, L.S. Hurley, The influence of trace elements on the skeleton, Clin. Orthop. Relat. Res. 27 (1963) 213–264.

[204] B.J. Friedman, J.H. Freeland-Graves, C.W. Bales, F. Behmardi, R.L. Shorey-Kutschke, R.A. Willis, J.B. Crosby, P.C. Trickett, S.D. Houston, Manganese balance and clinical observations in young men fed a manganese-deficient diet., J. Nutr. 117 (1987) 133–43.

[205] J.Y. Reginster, L.G. Strause, P. Saltman, P. Franchimont, Trace elements and postmenopausal osteoporosis: A preliminary study of decreased serum manganese, Med. Sci. Res. 16 (1988) 337–338.

[206] H. Rico, N. Gómez-Raso, M. Revilla, E.R. Hernández, C. Seco, E. Páez, E. Crespo, Effects on bone loss of manganese alone or with copper supplement in ovariectomized rats A morphometric and densitomeric study, Eur. J. Obstet. Gynecol. Reprod. Biol. 90 (2000) 97–101.

[207] P.D. Saltman, L.G. Strause, The role of trace minerals in osteoporosis., J. Am. Coll. Nutr. 12 (1993) 384–389.

[208] R.M. Leach, A.-M. Muenster, W.E. M., Studies on the Role of Manganese in Bone Formation, Arch. Biochem. Biophys. 133 (1969) 22–28.

[209] T. Landete-Castillejos, J.D. Currey, J.A. Estevez, Y. Fierro, A. Calatayud, F. Ceacero, A.J. Garcia, L. Gallego, Do drastic weather effects on diet influence changes in chemical composition, mechanical properties and structure in deer antlers?, Bone. 47 (2010) 815–825.

[210] T. Landete-Castillejos, I. Molina-Quilez, J.A. Estevez, F. Ceacero, A.J. Garcia, L. Gallego, Alternative hypothesis for the origin of osteoporosis: The role of Mn, Front. Biosci. - Elit. 4 (2012) 1385–1390.

[211] P.M.C. Torres, S.I. Vieira, A.R. Cerqueira, S. Pina, O.A.B. Da Cruz Silva, J.C.C. Abrantes, J.M.F. Ferreira, Effects of Mn-doping on the structure and biological properties of β-tricalcium phosphate, J. Inorg. Biochem. 136 (2014) 57–66.

[212] F. Lüthen, U. Bulnheim, P.D. Müller, J. Rychly, H. Jesswein, J.G.B. Nebe, Influence of manganese ions on cellular behavior of human osteoblasts in vitro, Biomol. Eng. 24 (2007) 531–536.

[213] P. González, J. Serra, S. Liste, S. Chiussi, B. León, M. Pérez-Amor, Raman spectroscopic study of bioactive silica based glasses, J. Non. Cryst. Solids. 320 (2003) 92–99.

[214] X. Chatzistavrou, T. Zorba, E. Kontonasaki, K. Chrissafis, P. Koidis, K.M. Paraskevopoulos, Following Bioactive Glass Behavior Beyond Melting Temperature by Thermal and Optical Methods, Phys. Status Solidi. 201 (2004) 944–951.

[215] M. Furko, Z. May, V. Havasi, Z. Kónya, A. Grünewald, R. Detsch, A.R. Boccaccini, C. Balázsi, Pulse electrodeposition and characterization of non-continuous , multi-element-doped hydroxyapatite bioceramic coatings, JSolid StateElectrochem. In Press (2017).

[216] M. Agostini, F. Romeo, S. Inoue, M. V Niklison-Chirou, A.J. Elia, D. Dinsdale, N. Morone, R.A. Knight, T.W. Mak, G. Melino, Metabolic reprogramming during neuronal differentiation, Cell Death Differ. 23 (2016) 1502–1514.

[217] L. Schneider, S. Giordano, B.R. Zelickson, M. S. Johnson, G. A. Benavides, X. Ouyang, N. Fineberg, V.M. Darley-Usmar, J. Zhang, Differentiation of SH-SY5Y cells to a neuronal phenotype changes cellular bioenergetics and the response to oxidative stress, Free Radic. Biol. Med. 51 (2011) 2007–2017.